Imperial College
London

In situ Synchrotron Characterisation of Fe-rich Intermetallic Formation during the Solidification of Al-Si-Cu-Fe alloys

Chedtha Puncreobutr

A THESIS SUBMITTED IN FULFILMENT OF REQUIREMENTS FOR THE DEGREE OF
DOCTOR OF PHILOSOPHY IN MATERIALS ENGINEERING

November 2013

Department of Materials
Imperial College London

Abstract

The enrichment of Fe during aluminium recycling increases the quantity of Fe-rich intermetallics formed, particularly β-Al_5FeSi, limiting the usage of recycled Al in many fatigue-sensitive applications.

In this study, fast synchrotron x-ray tomography was used to investigate microstructure evolution and defect formation in a commercial A319 alloy (Al-7.5Si-3.5Cu, wt.%) with differing Fe-levels (0.2-0.6 wt.%Fe) during *in situ* solidification and isothermal uniaxial tensile deformation. The captured dynamic changes were quantified using novel image analysis techniques and analysed using computational fluid dynamics. Together these provide new insights into the mechanisms of intermetallic nucleation and growth, and their influence on flow blockage and defect formation.

First, time-resolved qualitative and quantitative characterisation revealed that plate-like β-intermetallics nucleate both off the primary aluminium dendrites in the bulk of the specimen as well as off the oxide skin on the specimen surface. Second, β-intermetallic formation is largely complete before the formation of the Al-Si eutectic. Third, β-intermetallics are geometrically complex, demonstrating fast lateral growth and an ability to grow around and in between the primary dendrite arms. Last, direct impingement and potential branching are observed at a wide range of contact angles, indicating that the growth interaction might not be crystallographically related.

The presence of β-intermetallics contributes to several factors that influence defect formation. They block interdendritic flow, increase pore tortuosity and reduce permeability. Pores were observed to grow preferentially along the solid surface of intermetallics, suggesting that β-intermetallics may reduce the gas-solid interfacial energy and thus facilitate the pore growth. However, they do not nucleate the porosity. The results also show that failure under mild uniaxial semi-solid tension, simulating hot-tearing, displays a much more brittle-like failure mechanism when large β-intermetallics are present, compared to the more ductile behaviour of the base alloy with unresolved β-intermetallics.

Declaration

I, Chedtha Puncreobutr, hereby declare that this thesis and associated research are the results of my own investigation carried out in the Department of Materials at Imperial College London during the period from October 2009 to September 2013.

The copyright of this thesis rests with the author and is made available under a Creative Commons Attribution Non-Commercial No Derivatives licence. Researchers are free to copy, distribute or transmit the thesis on the condition that they attribute it, that they do not use it for commercial purposes and that they do not alter, transform or build upon it. For any reuse or redistribution, researchers must make clear to others the licence terms of this work.

Chedtha Puncreobutr

November 2013

Acknowledgement

First and foremost, I would like to express my sincere gratitude to both of my supervisors, Professor Peter D Lee and Dr Andrew Horsfield, for providing me the opportunity to pursue my PhD degree, as well as encouraging me to collaborate with other researchers. Their valuable suggestions and continuous support without reserve ever since my very first day in the Department of Materials at Imperial College have guided me through difficult problems, inspired ideas, and helped me gain knowledge and experience.

I would like to acknowledge the tremendous financial, materials and facilities support from the Thai Government Scholarship, M-ORS, EPSRC, Ford Motor Company, MXIF and RCaH. I also would like to acknowledge the provision of beamtimes and help from the scientists at the TOMCAT beamline, Swiss Light Source, and I12 beamline, Diamond Light Source.

Particularly, I would like to thank my colleagues, Dr André Phillion, Dr Julie L Fife, Dr Junsheng Wang, Dr Thomas Connolley, Dr Peter Rockett, Mr Richard W Hamilton, Dr Robert C Atwood, and Dr Steven Van Boxel for their considerable contribution to my knowledge acquisition in various aspects. It has been a great pleasure working as a part of the teams.

I would like to thank my friends, Dr Ziyu Zhang, Mr Taek Bo Kim, Miss Huiyu Yan, Mr Alex Leung, Mr David Wearing, Dr Lang Yuan, Dr Sobhan Abolghasemi, Dr Farid Tariq, Mr Jinesung Jung, Miss Gladys Teo, and Mr Phromphong Pandee. Thanks for sharing wonderful experiences and making lunch times so enjoyable during the past years. I am very grateful to soon-to-be Dr Kristina Maria Kareh, a great friend, for useful discussion and kindly help. Discussing with her, I always gain a better understanding of my work. Her careful and efficient proof reading was also invaluable.

Dedication

to my beloved parents

ฝนทั่งเหล็กเหลี่ยมป้าน เป็นเข็ม
สำเร็จตามนึกเต็ม แต่ใช้
การงานสิ่งใดได้เล็ม และล่วง เปลืองนา
สบสิ่งสรรพใดได้ เสร็จด้วยพากเพียร

พระยาสีหราชฤทธิไกร

"The perseverance is like the constant dropping water that wears away a stone. Success will come after the hard work; even an iron rod can be ground down to become a needle."

—An epigram from Praya Sriharajrittigrai,
a Thai poet to King Chulalongkorn

Publications

The research presented in Chapters 3, 4 and 5 contain results which have been published or submitted for publication in the following journals:

(1) Puncreobutr, C., Fife, J.L., Phillion, A.B., Rockett, P., Horsfield, A. and Lee, P.D. (2014) "In situ synchrotron quantification of the nucleation and growth of Fe-rich intermetallics during Al alloy solidification," Acta Materialia, Submitted.

(2) Puncreobutr, C., Lee, P.D., Kareh, K.M., Connolley, T., Fife, J.L. and Phillion, A.B. (2014) "Influence of Fe-rich intermetallics on solidification defects in aluminium-silicon-copper alloys," Acta Materialia, Submitted.

(3) Puncreobutr, C., Phillion, A.B., Fife, J.L. and Lee, P.D. (2014) "Coupling in situ synchrotron x-ray tomographic microscopy and numerical simulation to quantify the influence of intermetallic formation on permeability in aluminium-silicon-copper alloy," Acta Materialia, In Press.

(4) Puncreobutr, C., Lee, P.D., Hamilton, R.W., Cai, B., Connolley, T. (2013) "Synchrotron tomographic characterization of damage evolution during aluminium alloy solidification", Metallurgical and Materials Transactions A, 44 (12), pp. 5389-5395.

(5) Puncreobutr, C., Lee, P.D., Hamilton, R.W., and Phillion, A.B. (2012) "Quantitative 3-D characterization of solidification structure and defect evolution in Al alloys", JOM, 64 (1), pp. 89-95.

Additionally, parts of the research have been presented at the following international conferences:

(6) "Quantitative analysis of Fe-rich intermetallic nucleation and growth in aluminium alloys during in-situ solidification via ultra-fast synchrotron-based x-ray tomographic microscopy", International Symposium on Cutting Edge of

Computer Simulation of Solidification, Casting and Refining (CSSCR2013), Finland and Sweden, 20-23 May 2013.

(7) “In situ synchrotron x-ray imaging and computation to determine the influence of intermetallics on solidification defect formation”, International Symposium on Cutting Edge of Computer Simulation of Solidification, Casting and Refining (CSSCR2013), Finland and Sweden, 20-23 May 2013.

(8) “Quantifying Fe-rich intermetallic formation and subsequent pore interaction during solidification of Al alloys using in situ synchrotron-based tomographic microscopy”, TMS Annual Meeting and Exhibition (TMS 2012), Orlando, FL, 11-15 March 2012.

(9) "High speed tomography for the in situ quantification of pore evolution during the solidification of Al-Si-Cu-Fe alloys", TMS Annual Meeting and Exhibition (TMS 2011), San Diego, CA, 27 February - 3 March 2011.

(10) "In situ synchrotron quantification of Fe-rich intermetallic formation in Al-Si-Cu-Fe alloys", TMS Annual Meeting and Exhibition (TMS 2010), Seattle, WA, 14-18 February 2010.

Table of contents

Abstract 3

Declaration 5

Acknowledgement 6

Dedication 7

Publications 9

Table of contents 11

List of figures 15

List of tables 22

Nomenclature 23

Chapter 1 Introduction 27

1.1 Motivation 27

1.2 Objectives 29

1.3 Thesis structure 30

Chapter 2 Literature review 33

2.1 Solidification Theory 33

2.1.1 Nucleation 33

2.1.2 Growth kinetics 41

2.2 Fe-rich Intermetallics 45

2.2.1 Intermetallic phases in Al and Al-Si alloys 46

2.2.2 Reactions governing β-Al_5FeSi intermetallic formation 50

2.2.3 Formation of β-Al_5FeSi intermetallics 52

2.2.4 Modification of β-Al_5FeSi intermetallics 58
2.3 Permeability 60
2.3.1 Permeability measurements 60
2.3.2 Permeability models 61
2.3.3 Particle blockage 63
2.4 Solidification defects 64
2.4.1 Porosity 65
2.4.2 Hot tearing 71
Chapter 3 Formation of β-intermetallics 77
3.1 Methods 78
3.1.1 Specimen preparation 78
3.1.2 *In situ* solidification experiments 80
3.1.3 Tomographic reconstruction 82
3.1.4 Image processing and segmentation 84
3.1.5 Characterisation 85
3.1.6 Quantification 86
3.1.7 Visualisation 90
3.2 Solidification Sequence 91
3.3 Nucleation mechanisms 95
3.4 Growth kinetics 101
3.5 Intermetallic-intermetallic interactions 107
3.6 Summary 111

Chapter 4 Influence of β-intermetallic formation on permeability 113

4.1 Methods 114

4.1.1 *In situ* tomographic imaging 114

4.1.2 Preparing datasets for flow simulation 116

4.1.3 Flow simulation 117

4.2 Microstructural evolution 119

4.3 Flow simulations 121

4.4 Permeability assessment 124

4.5 Determination of an analytical permeability expression 127

4.6 Comparison with experimental data and analytical approximations 130

4.7 Summary 132

Chapter 5 Influence of β-intermetallics on solidification defects 133

5.1 Methods 135

5.1.1 Materials 135

5.1.2 Solidification experiment 136

5.1.3 Semi-solid deformation experiment 137

5.1.4 Quantitative characterisation 138

5.2 Effect of β-intermetallics on porosity formation 140

5.3 Effect of β-intermetallics on hot tear formation 143

5.3.1 *In situ* observation 143

5.3.2 Post-failure observation 147

5.4 Discussion 150

5.5 Summary 153

Chapter 6 Conclusions and future work 155

6.1 Conclusions 155

Nucleation and growth mechanisms of β-intermetallic 156

Influence of β-intermetallic on fluid flow 157

Effect of β-intermetallics on solidification defects 158

6.2 Suggestions for further research 160

Bibliography 161

List of figures

Figure 1.1 Influence of β-intermetallics in aluminium recycled alloys on crack initiation and failure (micrograph of crack initiation after [6]). 28

Figure 2.1 Free energy change associated with homogeneous nucleation of a spherical solid as function of its radius (using pure Al properties [14] at fixed undercooling of 5K) 35

Figure 2.2 The nucleation schematic of a spherical solid cap at a liquid-substrate interface, after [14] 36

Figure 2.3 The nucleation schematic of a spherical solid cap at a liquid-substrate interface, after [14] 37

Figure 2.4 (a) The continuous distribution of active nucleation sites as a function of undercooling (after [14]); and (b) histogram and fitted Gaussian distribution of pore nucleation in Al-Cu alloy (after [23]). 40

Figure 2.5 Types of solid-liquid interface: (a-b) non-faceted interface and (c-d) faceted interface. Images (a, c) represent interfaces at microscopic scale (after [21]) whereas images (b, d) represent interfaces at atomic scale (after [14]). 44

Figure 2.6 Al-rich corner of the equilibrium Al-Fe binary phase diagram, from [44]. 47

Figure 2.7 Typical 2-D morphologies of script-like α-Al_8Fe_2Si and plate-like β-Al_5FeSi from (a) optical microscopy (from [47]) and (b) scanning electron microscopy (SEM) (from [48]) 47

Figure 2.8 3-D morphologies of (a) α-$Al_{15}(Fe,Mn)_3Si_2$ and (b-c) β-Al_5FeSi intermetallics. Note that the 3-D renders in (a-b) were obtained from serial sectioning method (from [49]) whereas (c) were obtained from x-ray tomography (from [11]). 48

Figure 2.9 Volume fraction of β-Al_5FeSi intermetallic as a function of temperature, after [54] 49

Figure 2.10 (a) Polythermal section of the Al-Si-Fe phase diagram at 0.6wt.%Fe (from [4]); and (b) liquidus projection of Al–Si–Fe system, where isothermal lines are shown in dark and red lines correspond to the invariant reactions (from [11]). 51

Figure 2.11 (a) Nucleation of β-intermetallic on γ-aluminium oxide (from [69]); and (b) radiograph showing β-intermetallic oriented parallel to near-by dendrite arms (from [73]). 54

Figure 2.12 (a) HREM image β-Al_5FeSi intermetallic showing twinning (from [59]); and (b) HRTEM image showing steps on β-Al_5FeSi faceted boundary (from [60]). 55

Figure 2.13 (a) Growth evolution of β-intermetallic from *in situ* x-ray radiography, after [36]; (b) tomography images showing erratic growth of β-intermetallic, after [63]; and (c) schematics of β-intermetallic growth mechanism proposed by [63]. Insets I-III in (a) represent the temperatures of 564°C, 558°C and 531°C respectively, whereas insets I-III in (b) show the time steps of 31.3min, 38.0min and 39.9min, respectively, after the first scan. 56

Figure 2.14 Evolution of an β-intermetallic via growth and branching mechanisms, after [63]. Insets I-IV show time of 27.6min, 28.5min, 30.4 and 32.3min after the first scan, respectively. 57

Figure 2.15 (a) Flow simulation of columnar dendrites with blocking carbides in Ni-based superalloys, after [119], and (b) quenched Al-Si microstructure showing β-intermetallics in the interdendritic regions, from [47]. 64

Figure 2.16 Schematic of pore growth between dendrites at solidification time: (a) $t1$ and (b) $t2 > t1$. 67

Figure 2.17 Solidified microstructures of Al-9Si-3Cu-1Fe (wt.%) showing (a) pore nucleation along β-intermetallic and (b) restriction of pore growth by β-intermetallic (indicated by arrows), from [132]. 68

Figure 2.18 (a) radiograph showing β-intermetallics (β) and pores (P) during *in situ* solidification of Al-7.5Si-3.5Cu-0.8Fe (wt.%) (from [36]); (b) 3-D rendering of porosity in fully solidified microstructure of Al-7.5Si-3.5Cu-0.4Fe (wt.%) (from [138]); and (c) influence of Fe content on maximum size of β-intermetallics and pores (from [11]). 70

Figure 2.19 Evolution of hot tearing: (a) sequence of x-ray radiographs obtained during isothermal horizontal tensile loading of Al-12Cu (wt.%) at 580 °C (fS~0.62) and (b) schematic. Strain localisation and fluid flow towards this region, nucleation and growth of damage, and final fracture are shown in inset I-III (of both a and b), respectively, after [92] 73

Figure 2.20 (a) 2-D longitudinal sections and (b) 3-D images of liquid accumulation in the notched area during isothermal vertical tensile loading of Al-8Cu (wt.%) at 555°C (fS~0.93), after [157]. Note that liquid appears white in (a) and blue in (b) whereas damage (void) appears dark in (a) and not rendered in (b). 74
Figure 3.1 (a) Schematic and (b) photograph of wedge mould casting..... 79
Figure 3.2 (a) Cross-sectional schematic of the experimental setup, (b) photograph of the furnace mounted on the TOMCAT beamline of the SLS and (c) schematic of the holding arm affixed to the TOMCAT base stage..... 81
Figure 3.3 X-ray tomographic acquisition and reconstruction. 83
Figure 3.4 Image processing steps: (a) slice of the original reconstructed data, (b) masking of the specimen (blue) and the background (red), (c) masked and filtered slice, and (d) segmentation of the α-Al dendrites (purple), β-intermetallics (green) and pores (yellow). 85
Figure 3.5 Characterisation steps: (a) segmented β-intermetallics, (b) individual β-intermetallics separated and labelled with different colours, (c) normals of labelled β-intermetallics shown as cone directions, and (d) centroid of each β-intermetallic..... 86
Figure 3.6 Measurement of the length of an intermetallic: (a) bounding box method and (b) PCA method. 88
Figure 3.7 Thickness measuring steps: (a) an intermetallic, (b) centerline tree (red) calculated from (a), (c) boundary distance map calculated from (a) and (d) thickness along the center-lines calculated from (b-c). 89
Figure 3.8 Interfacial normals (red arrows) of each triangular face..... 90
Figure 3.9 (a) Rendering of the specimen (red) inside the BN holder, (b,d,f,h,j) typical microstructure evolution during solidification of Al-7.5Si-3.5Cu-0.6Fe (wt.%), (c) 3-D rendering of the dendritic structure, and (e,g,i) 3-D rendering of the β-intermetallics (multi-colour is used to separate different intermetallics whereas the same colour is kept for the same intermetallics at different temperatures). The microstructures and rendering volumes represent temperatures of (b) 600°C, (c-d) 582°C, (e-f) 578°C, (g-h) 572°C and (i-j) 550°C. Note that these results were taken from the first experiment with a capture interval of 72s..... 92

Figure 3.10 Evolution of intermetallic formation at (a-f) 579°C, 578°C, 577°C, 576°C, 575°C and 574°C, respectively. Note that these results were taken from the second experiment with a capture interval of 12s. 93

Figure 3.11 Fraction of the β-intermetallic phases as quantified from the first and second experiments, and compared to calculations from the Scheil solidification model. 94

Figure 3.12 Histogram of the nucleation density of the β-intermetallic phase as a function of nucleation temperature (T_n) and nucleation undercooling (ΔT_n). The Gaussian distribution fitted on the histogram is also shown. 96

Figure 3.13 Examples of β-intermetallics nucleation mechanisms: (red intermetallic in a-b) specimen surface, (blue intermetallic in c-d) α-Al dendrite, (green intermetallic in e-f) existing intermetallic and (orange intermetallic in g-h) as-cast porosity. Al-dendrites and pores are rendered in grey whereas surrounding intermetallics are rendered in pink. Rendering volumes represent temperatures of (a-b) 579°C, (c-d) 578.5°C, (e-f) 578°C and (g-h) 576°C. 98

Figure 3.14 Quantified β-intermetallic nucleation rate, classified by 4 types of nucleation sites. Insets I-IV illustrate intermetallics that were nucleated on specimen surface, as-cast pores, existing intermetallics, and liquid/dendrite, respectively. Note that each intermetallic is rendered as it first appeared in the specimen. 99

Figure 3.15 (a) Orientation contour plot of the normal distribution of all intermetallic plates as compared to the growth directions of the secondary dendrite arms; (b) IND of the dendritic structure. Each white dot in (a) represents the normal of each plate. The insets illustrate how each white dot was determined. 100

Figure 3.16 The different growth evolutions of β-intermetallics during solidification: (a) standard plate-like growth, (b-c) growth of complex plate-like shapes, (d) growth around dendrite arm and subsequently forming a cavity by joining up the separated growth, (e) formation of bent intermetallic and (f) growth of one intermetallic passing an obstructing intermetallic. 102

Figure 3.17 Distribution of β-intermetallic length at different temperatures after nucleation (T_n - T). 103

Figure 3.18 Average length and thickness of intermetallics as a function of temperature (T_n - T) and time (t - t_n) after nucleation. 104
Figure 3.19 (a) Average initial growth velocity as a function of nucleation temperature (T_n) and nucleation undercooling (ΔT_n), and (b) mean growth velocity as a function of temperature (T_n - T) and time (t - t_n) after nucleation. 105
Figure 3.20 Types of intermetallic-intermetallic interactions: (a-c) impingement mechanism and (d-f) potential branching mechanism. Measurements of 3-D angles between each contact are also detailed. 108
Figure 3.21 Quantified number of occurrences of different types of intermetallic-intermetallic interactions. Insets I-III illustrate criteria used to classify growth interactions into (I) impingement, (B) branching, and (U) unclassifiable. Inset IV plots the histogram of angles between each contact over different types of interactions. 110
Figure 4.1 Rendering of the full dendritic structure from the dataset captured at 582±1°C (fS=0.27), coloured by the local mean curvature. The highlighted box (red) is the region chosen for the permeability study. 116
Figure 4.2 Schematic outlining the segmentation process utilized to obtain the non-permeable domain for the CFD calculation: (a) original data, (b) segmented primary Al, (c) β-intermetallics, and final non-permeable structure both (d) without and (e) with β-intermetallics..... 117
Figure 4.3 Simulation setup for CFD calculation..... 118
Figure 4.4 Longitudinal images acquired via x-ray tomographic microscopy showing the typical microstructure evolution of Al-7.5Si-3.5Cu-0.6Fe (wt.%) during solidification. The images (a-d) represent microstructure at temperatures of 582±1°C, 575±1°C, 568±1°C and 555±1°C, respectively. The corresponding solid fractions were calculated to be 0.23, 0.30, 0.39, and 0.78, respectively. 119
Figure 4.5 The evolution in fS and fI observed in the *in situ* 3-D imaging of solidification as compared to the lever-rule and Scheil behaviour. Each discrete point (square, circle) represents one 3-D tomographic dataset, while the lines I-IV represent the fS corresponding to images (a-d) in Figure 4.4. The sequence of phase formation is also indicated. 120
Figure 4.6 Simulated pressure contours in the interdendritic liquid region (i.e., the negative volume of Figure 4.2) both (a,c,e) without and (b,d,f) with β-

intermetallics. The 3-D microstructures shown represent the pressure contours at solid fraction of (a,b) 0.30 (578°C), (c,d) 0.36 (572°C), and (e,f) 0.41 (565°C). The corresponding simulated liquid velocities both (g) without and (h) with β-intermetallics shown represent solid fraction of 0.33 (575°C)..... 122

Figure 4.7 2-D cross-sectional views of the calculated 3-D velocity magnitudes showing the fluid flow within the interdendritic region during solidification both (a,c,e,g) without, and (b,d,f,h) with β-intermetallics at solid fraction of (a,b) 0.30 (578±1°C), (c,d) 0.36 (572±1°C), (e,f) 0.41 (565±1°C), and (g,h) 0.56 (561±1°C). The primary Al-rich dendrites and eutectic are coloured in grey while the β-intermetallics are white. 123

Figure 4.8 The evolution in permeability for liquid flow (a) parallel and (b) normal to the primary columnar dendrites both without and with β-intermetallics. Dashed-lines indicated the temperatures where the nucleation of β-intermetallic and eutectic Al phases were observed in the 3-D renderings. 125

Figure 4.9 Simulated flow velocities in a sub-volume of interdendritic liquid extracted from the volume shown in Figure 4.7h for flow (a) parallel and (b) normal to the orientation of the β-intermetallic particles. Note the direction of v in each image showing the fluid flow. 127

Figure 4.10 Comparison between the simulated permeability and the regression fitting, Equations (4.3) and (4.4), for liquid flow both (a) parallel and (b) normal to the primary columnar dendrites in solidifying microstructures both with and without β-intermetallics. Note that the annotated *eut* indicates a structure containing eutectic material. 129

Figure 4.11 Comparison between the simulated permeability in solidifying microstructures both with and without β-intermetallics, analytical models (curves) [94, 117, and present work], and experimental data from Pb-Sn and borneol-paraffin alloys (crosses) [94, 100, 101] in units of dimensionless permeability for flow both (a) parallel and (b) normal to the primary columnar dendrites. Note that the annotated *eut* indicates a structure containing eutectic material..... 131

Figure 5.1 Calculated fraction of the β-intermetallics in Al-A319 alloys at two Fe-levels of (I) 0.2 wt.%Fe and (II) 0.6 wt.%Fe, assuming Scheil solidification model. (I) and (II) show high-resolution longitudinal sections of typical as-cast solidified microstructures..... 136

Figure 5.2 (a-b) Schematics of experimental setups for solidification and semi-solid uniaxial tension studies, respectively; and (c) photograph of thermal-mechanical testing rig. 137

Figure 5.3 (a) Rendered evolution of a pore during solidification (I-V represent temperatures of 565°C, 561°C, 550°C, 540°C and 502°C, respectively); (b) quantified volume and sphericity of the pore shown in (a). Quantified fraction of intermetallics is also illustrated. 140

Figure 5.4 Rendering of pore evolution (blue) with the presence of intermetallics (red) (a-d represent temperatures of 565°C, 561°C, 555°C and 550°C, respectively). Examples of pore growth along solid surface of intermetallics are shown in dashed-circles. 142

Figure 5.5 Typical evolution of damage during simulated hot tearing in Al-7.5Si-3.5Cu with 0.2 wt.%Fe (a-d) and 0.6 wt.%Fe (e-h). Note that a-d represent true strains (%) of 0, 14, 17, 19 and e-h represent true strains (%) of 0, 4, 5, 7, respectively. Dashed-circles indicate locations where critical damage initiated. 144

Figure 5.6 3-D rendering of hot tear formation in Al-7.5Si-3.5Cu with (a) 0.2 wt.%Fe and (b) 0.6 wt.%Fe as well as the quantified evolution in (c) the internal damage volume (int) and surface-connected damage volume (surf). I-IV represent true strains (%) of 0, 14, 17, 19 and 0, 4, 5, 7, for specimens with 0.2 wt.%Fe and 0.6 wt.%Fe, respectively. Note that internal damage is coloured in blue and surface-connected damage is labelled in red in (a-b). 145

Figure 5.7 (a,c) Longitudinal sections of post-failure microstructures in Al-7.5Si-3.5Cu with 0.2 and 0.6 wt.%Fe, respectively; and (b,d) magnified microstructures from an ROI (yellow square) in (a,c), respectively. 148

Figure 5.8 (a-b) Rendered internal voids (colour by volume) in Al-7.5Si-3.5Cu with 0.2 and 0.6 wt.%Fe, respectively, and (c) quantified number density and volume of internal voids shown in (a-b). 149

Figure 5.9 (a-b) 3-D rendering of internal void (coloured by local mean curvature) near fracture surface of Al-7.5Si-3.5Cu with 0.2 and 0.6 wt.%Fe, respectively. Intermetallics in (b) are shown in dark colour. 150

Figure 5.10 Orientation contour plot of all internal void in post-failure microstructures of Al-7.5Si-3.5Cu with (a) 0.2 wt.%Fe and (b) 0.6 wt.%Fe. Inset I-IV schematise orientation plot (each dot in circle) of an object with four different orientations. 152

List of tables

Table 3.1 Chemical composition of A319 alloy with 0.6Fe (wt.%) 79
Table 4.1 Parameters for Blake-Kozeny permeability expressions 128
Table 5.1 Chemical composition of A319 alloys (wt.%) 135

Nomenclature

Roman alphabet

Symbol	*Description*	*Unit*
A	surface or cross-sectional area	m^2
C	concentration of solute	wt.%
C_S^*, C_L^*	concentration of solute in the solid and liquid phases at the solid-liquid interface	wt.%
D	diffusion coefficient	m^2/s
d	diameter	m
f	fraction	
G	Gibbs free energy	J/mol
g	gravitational acceleration, 9.80665	m/s^2
I	rate of formation / nucleation rate	mol/s
K	permeability of the porous medium	m^2
K_p	permeability in direction of parallel flow	m^2
K_n	permeability in direction of normal flow	m^2
k	curvature	1/m
k_B	Boltzmann's constant, $1.380650424\times10^{-23}$	J/K
k_C	Carman-Kozeny constant	
k_p	equilibrium partition coefficient	
L_f	latent heat of fusion per unit mass	J/kg
m_L	slope of liquidus line	°C/wt.%
n	number of nuclei / nucleation density	
P	pressure	Pa
p	probability	
p_c	probability of capturing an atom at surface	
R	ideal gas constant, 8.3144621	J/(mol·K)
Re	Reynolds number	
r	radius	m
r_1 and r_2	principal radii of the curvature k	m
S^m	molar entropy	J/(mol·K)
SS	hydrogen supersaturation	ml/100g STP

Symbol	*Description*	*Unit*
T	temperature	°C / K
T_n	nucleation temperature	°C
$\dot{T}$	cooling rate	°C/s
t	time	s
t_n	time at nucleation moment	s
V	volume	m^3
v	velocity	m/s

Greek alphabet

Symbol	*Description*	*Unit*
α	Jackson factor	
Γ	Gibbs-Thomson coefficient	K·m
γ	interfacial energy	J/m^2
ΔG	Gibbs free energy change	J/mol
ΔS_f^m	molar entropy of fusion	J/(mol·K)
ΔS_V	entropy of fusion per unit volume	$J/(m^3 \cdot K)$
ΔT	undercooling	K
ΔT_σ	standard deviation of the undercooling distribution	K
ΔT_C	constitutional (solutal) undercooling	K
ΔT_g	undercooling for free growth (geometrically limited undercooling)	K
ΔT_k	kinetic undercooling	K
ΔT_M	mean of the nucleation undercooling distribution	K
ΔT_n	nucleation undercooling	K
ΔT_r	curvature undercooling	K
ΔT_t	thermal undercooling	K
ΔT_{total}	total undercooling	K
∇P	pressure gradient	Pa
θ	wetting angle, rotation angle	rad, deg
λ_1	primary dendrite arm spacing	m
λ_2	secondary dendrite arm spacing	m

Symbol	*Description*	*Unit*
v_0	atomic vibration frequency	Hz
μ	viscosity	Pa·s
ρ	density	kg/m^3
τ	tortuosity of the interdendritic liquid channels	

Subscripts, superscripts and indices (A = variable from symbol list)

Symbol	*Description*
A^*	critical value / evaluated at the interface
A_{actual}	actual value
A^m	amount per mole
A_{LG}	liquid-gas interface
A^{heter}	heterogeneous
A^{homo}	homogeneous
A^i	species i
A_G	gas phase
A_I	intermetallic phase
A_L	liquid phase
A_{liq}	liquidus
A_m	melting point
$A_{\max}$	maximum value
A_P	pore phase
A_S	solid phase
A_{SL}	solid-liquid interface
A_{sol}	solidus
A_0	nominal, reference, or initial value
A^∞	evaluated at position far away from interface

Chapter 1

Introduction

1.1 Motivation

Good castability and a favourable strength-to-weight ratio make aluminium alloys ideal candidates for automotive and aerospace components since they improve fuel economy and performance through weight reduction. Applications range from heat exchangers and engine blocks to aircraft bodies [1]. Aluminium can be produced by two different methods: (1) primary aluminium production from bauxite, and (2) secondary production via recycling of old aluminium products. The production of primary aluminium consists of three steps: bauxite mining, alumina production and electrolysis. To produce 1 kilogram of aluminium using primary production, 17 KWh of energy [2] is required for the Hall-Héroult electrolytic reduction process and 7.8 kg of CO_2 [2] is released into the environment. Secondary production involves the re-melting and the fluxing of existing metal to remove the impurities. This method is both less expensive and less energy intensive compared to the production of new aluminium through electrolysing aluminium oxide. In comparison with the primary production method, the secondary aluminium production method emits less than 1 kg of CO_2 and it requires approximately 10% of the energy used in primary production [3].

During the recycling process, iron (Fe) is inadvertently added, primarily through small amounts of Fe in the aluminium scrap that is difficult to remove when sorting. Therefore, the Fe-content invariably increases from less than 0.1 (wt.%) in primary aluminium alloys to 0.4-0.8 (wt.%) in secondary aluminium alloys [4]. This level of Fe is much greater than the solubility of Fe in Al, which is normally in the range of 0.03-0.05 (wt.%) [5]. The Fe therefore combines with other elements in order to form intermetallic phases of various types. The most common Fe-rich intermetallics in hypoeutectic Al-Si alloys are plate-like intermetallics (β-Al_5FeSi) and Chinese-script intermetallics (α-Al_8FeSi or α-$Al_{15}(Fe,Mn)_3Si_2$) [4]. The hard and brittle β-intermetallic plates are a well-known detrimental phase that potentially degrades the mechanical properties, particularly fatigue life, of cast and wrought components [6]. Additionally, the presence of β-intermetallics can increase an alloy's propensity for formation of other solidification defects, specifically hot tears [7] and porosity [1, 8], further degrading the final mechanical properties of cast components or even causing part rejection. This detrimental effect leads to the prevention of use of recycled feed-stock in many fatigue-sensitive applications.

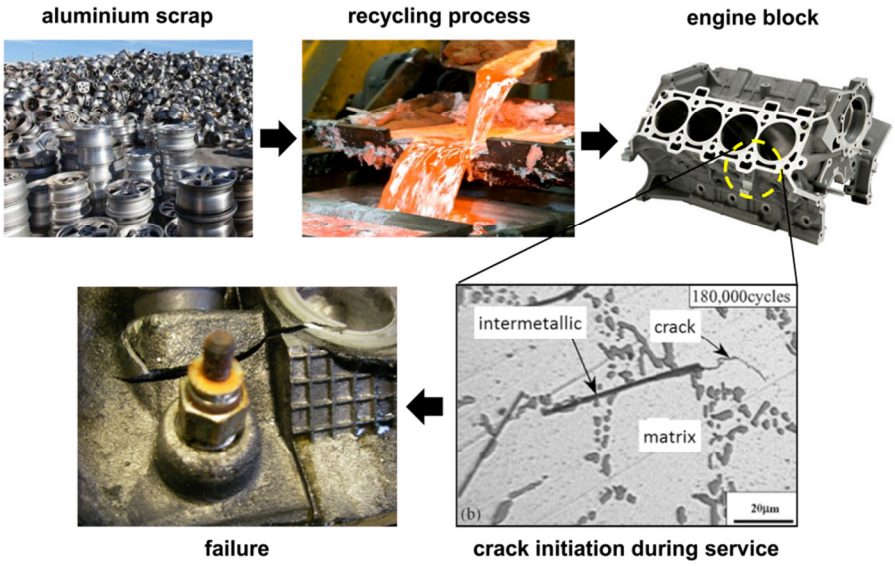


Figure 1.1 Influence of β-intermetallics in aluminium recycled alloys on crack initiation and failure (micrograph of crack initiation after [6]).

Figure 1.1 summarises recycling process and demonstrates an example of how intermetallics influences fatigue crack initiation and failure during service.

A number of attempts have been made to minimise the detrimental effects of Fe by altering the morphology of β-intermetallics into a less harmful and more compact form, such as script-like intermetallics [9]. Unfortunately, depending on the cooling rates and Fe levels, many of these treatments are ineffective in diminishing the presence of β-intermetallics. Therefore, a better understanding of the phase nucleation and growth kinetics of β-Al_5FeSi is required to control the formation of these potentially deleterious intermetallics. Without an adequate understanding of their nucleation and growth kinetics, minimising their effects will be limited to a trial and error experimental approach.

1.2 Objectives

The main objectives of this thesis are to:

(1) Perform fast *in situ* synchrotron x-ray tomographic experiments to observe microstructural evolution during *in situ* solidification and isothermal uniaxial tensile deformation of a commercial A319 alloy.

(2) Characterise the nucleation and growth mechanisms of β-intermetallics using novel image analysis techniques.

(3) Develop a method for coupling tomographic imaging with computational fluid dynamics to study the influence of β-intermetallics on flow blockage and permeability.

(4) Identify the effect of β-intermetallics on porosity and hot tear formation.

1.3 Thesis structure

The chapters are organised as follow:

Chapter 2 reviews the published research on thermodynamics and kinetics of intermetallic phase formation, fluid flow and permeability in semi-solid metals, mechanisms of porosity and hot tear formation, and influence of intermetallics on defect formation.

Chapter 3 investigates the mechanisms controlling the formation of β-intermetallics during *in situ* solidification. The β-Al_5FeSi phase solidification sequence as well as its nucleation and growth behaviours are characterised. The relationships between the evolution of β-intermetallics and both undercooling and time after nucleation event are determined. In addition, the incidents of direct impingement and potential branching are presented and discussed.

Chapter 4 studies the influence of β-intermetallics on interdendritic fluid flow. A coupled *in situ* imaging and computational fluid dynamics method is developed to quantify permeability evolution in observed solidifying microstructures, both with and without β-intermetallics. The impact of particle blockage is introduced as an additional term into the anisotropic Blake-Kozeny analytical expressions. Comparisons between the simulated results, prior experimental data from the literature and analytical expressions and are also explored.

Chapter 5 investigates *in situ* solidification and semi-solid deformation experiments in order to understand the influence of β-intermetallics on defect formation. β-intermetallics are found to promote porosity formation during solidification and aid pore growth, confirming previous hypothesised mechanisms [10, 11]. The brittle-like failure of the intermetallic-rich specimen is compared to the failure

of a base specimen with small, unresolved intermetallics and the contributions of the β-intermetallics to failure are quantified.

Chapter 6 summarises the key finding of the thesis and presents suggestions for further work.

Chapter 2

Literature review

In this chapter, the fundamental theories of solidification are briefly reviewed. This is then followed by a review of Fe-rich intermetallic phase formation in Al-Si alloys including thermodynamics and experimental studies. Finally, a review of the influence of intermetallics on permeability, porosity formation and hot tearing formation is presented.

2.1 Solidification Theory

Solidification is a transformation process in which liquid turns into one or more solid phases. When a system cools from the melt, the solidification process starts with the nucleation of solid particles and then continues with the growth of the solid phase.

2.1.1 Nucleation

As the temperature of a system drops to the solidification temperature the liquid phase is no longer in equilibrium, i.e. the free energy of the solid phase(s) will be lower than that of the liquid phase, and is likely to transform into the solid phase(s). However, this transformation process does not occur instantaneously since there is a free energy barrier for the creation of any new solid. Liquid can be kept in a supercooled

or supersaturated state to a certain extent as the system is cooled before the thermodynamic and the kinetic conditions are met for the nucleation of the solid phase. The nucleation theory will be explained in three parts: homogeneous nucleation, heterogeneous nucleation and nucleation kinetics.

2.1.1.1 Homogeneous nucleation

When solid clusters are formed in a melt free of any foreign materials or impurities, it is said to nucleate homogeneously [12]. Homogeneous nucleation involves the formation of solid clusters in the melt which form interfaces with the liquid phase. Assuming a spherical shape of the solid cluster and that the solid and liquid phases are homogeneous, the total free energy change (ΔG) for a single cluster with a radius r can be written as [13]:

$$\Delta G = \Delta G_V + \Delta G_I = V_S \frac{G_S^m - G_L^m}{V^m} + A_{SL}\gamma_{SL} = -\frac{4}{3}\pi r^3 \Delta S_V \Delta T + 4\pi r^2 \gamma_{SL} \qquad (2.1)$$

where ΔG_V is the free energy change associated with the volume of the cluster formed, ΔG_I is the free energy change due to the formation of solid-liquid interface, ΔS_V is the entropy of fusion per unit volume, ΔT is the undercooling, $G_S^m$and G_L^m are the molar free energies of the solid and liquid phase respectively, and $\gamma_{SL}$is the solid-liquid interfacial energy. The total free energy change as a function of radius r given in Equation (2.1) is illustrated in Figure 2.1.

At temperatures above or equal to the melting temperature (T_m), i.e. $\Delta T = T_m - T \leq 0$, the free energy in Equation (2.1) is positive and the transformation from the liquid to solid phase is not thermodynamically favoured. On the other hand, at temperatures below the melting temperature, i.e. $\Delta T > 0$, the interfacial free energy term increase with r^2 whereas the volume free energy term decreases proportionally to $r^3\Delta T$. At a large value of r, ΔG_V becomes greater than ΔG_I and the total free energy (ΔG)

becomes negative, hence making the nucleation of the solid phase in the melt thermodynamically favoured.

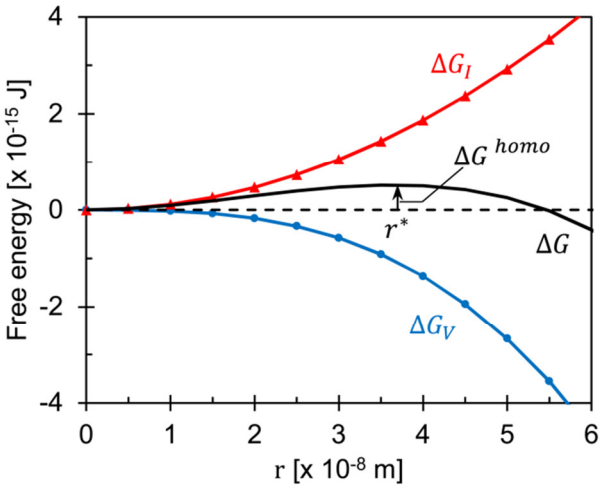


Figure 2.1 Free energy change associated with homogeneous nucleation of a spherical solid as function of its radius (using pure Al properties [14] at fixed undercooling of 5K)

It can be seen from Figure 2.1 that for a given undercooling there is a critical radius, r^*, that creates the maximum free energy, ΔG^*. The maximum free energy, also called the homogeneous nucleation barrier (ΔG^{homo}), at critical radius, $r^* = 2\gamma_{SL}/\Delta S_V \Delta T$, can be written as [15]:

$$\Delta G^* = \Delta G^{homo} = \frac{16\pi}{3} \frac{{\gamma_{SL}}^3}{{\Delta S_V}^2 \Delta T^2} \tag{2.2}$$

Clusters with $r < r^*$ will melt back into the liquid phase in order to lower the free energy of the system, whereas a cluster with $r > r^*$ is more likely to grow due to the resultant decrease in the free energy (note there are still stochastic fluctuations in this growth). It can be seen in Equation (2.2) that the homogeneous nucleation barrier is inversely proportional to the square of the undercooling. This means that as the undercooling increases, the barrier decreases and it becomes easier for the nucleation to occur. However, in reality, the undercooling required for nucleation of the primary solid phases in most castings is rather small, so homogeneous nucleation rarely happens in

practise and other mechanisms, i.e. heterogeneous nucleation, with a lower nucleation undercooling takes place.

2.1.1.2 Heterogeneous nucleation

When solidification is initiated from a foreign surface, i.e. solid particles suspended in liquid, oxide layers, or surface contact with a crucible wall, it is said to nucleate heterogeneously [12]. By forming a nucleus (assuming a spherical cap shape) on a surface of foreign substrate as shown in Figure 2.2, the positive interfacial term in Equation (2.2) can be reduced; hence the heterogeneous nucleation energy barrier is lower by a factor $f(\theta)$ [16]:

$$\Delta G^{heter} = \Delta G^{homo} f(\theta) = \frac{16\pi}{3} \frac{{\gamma_{SL}}^3}{{\Delta S_V}^2 \Delta T^2} f(\theta) \tag{2.3}$$

where $f(\theta)$ is a function of the wetting angle, θ, and its value is in the range of 0 to 1.

$$f(\theta) = \frac{(2 + cos\theta)(1 - cos\theta)^2}{4} \tag{2.4}$$

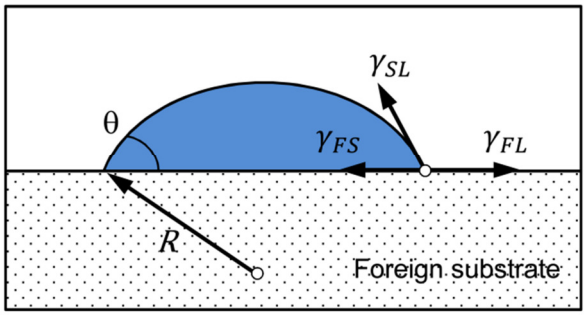


Figure 2.2 The nucleation schematic of a spherical solid cap at a liquid-substrate interface, after [14]

Since the heterogeneous nucleation barrier is lower than that of homogeneous nucleation for a solid cluster with a given radius r, it is much easier for heterogeneous nucleation to occur during solidification. The assumption of a spherical cap-shaped nucleus (as illustrated in Figure 2.2) in classical heterogeneous nucleation theory, however, becomes invalid for potent nucleation catalysis, i.e. θ, $f(\theta)$, and ΔG^{heter}

approach zero [17, 18]. By studying the effects of grain refiners (e.g. TiB_2 [19]) in aluminium melt, Quested and Greer [20] found that athermal nucleation dominates when potent nucleants (small wetting angles) initiate grains at small undercooling.

Figure 2.3 shows three regimes of nucleation on a foreign particle as a function of wetting angle and undercooling. In regime (i), heterogeneous nucleation on such a nucleant particle is not possible since the nucleant particle is not large enough to allow a hemi-spherical nucleus to form on its surface (assuming disk-shaped nucleants with diameter, d). Therefore, the system may need the same amount of undercooling as required for the homogeneous nucleation in order to nucleate solid grain.

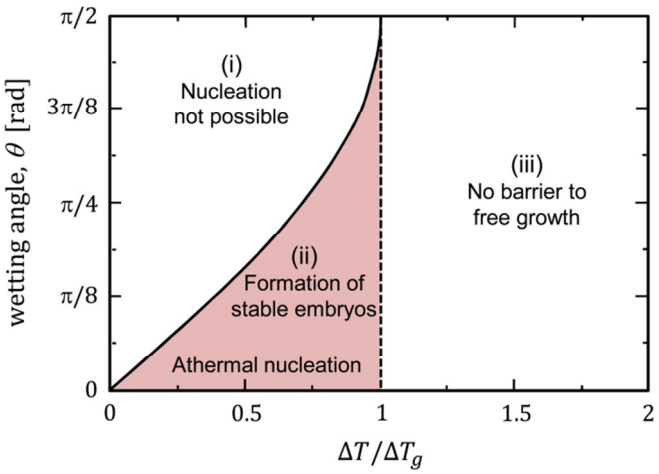


Figure 2.3 The nucleation schematic of a spherical solid cap at a liquid-substrate interface, after [14]

In regime (ii), the nucleant is not only sufficiently large for heterogeneous nuclei to form, but also small enough to geometrically limit the solid growth. The formation of heterogeneous nuclei on these nucleant particles can first occur very rapidly (athermal nucleation) at small wetting angles and undercooling. Once it forms, it can grow across the face of nucleant particles until the radius of curvature (R) of its interface reaches a critical value given by hemisphere, $R^* = d/2$. In order to allow further growth to occur, the undercooling must be increased to exceed the geometrically limited undercooling (or undercooling for free growth) ΔT_g [14], given by:

$$\Delta T_g = \frac{4\gamma_{SL}}{\Delta S_V d} = \frac{4\Gamma}{d} \tag{2.5}$$

where Γ is the Gibbs-Thomson coefficient. In regime (iii), undercooling is larger than ΔT_g and the free growth of the nucleus is thermodynamically favoured.

2.1.1.3 Nucleation kinetics

The rate of nucleation depends on the rate of diffusion and attachment of atoms to the solid-liquid nucleant surface and the number of critical clusters for which the free energy change (in Equations (2.2) and (2.3)) is negative. The diffusion of atoms is a thermally activated process, i.e. the rate of diffusion increases as the temperature increases and vice versa. Therefore, at high temperatures, the rate of diffusion of atoms to the nucleation site is high. However, at high temperatures the thermodynamic driving force for nucleation becomes less due to the lower undercooling and the number of critical clusters will be limited. As the temperature becomes very high and approaches the melting temperature of the system, the kinetic or the vibrational energy of the atoms increases and it becomes easier for atoms to detach from the nucleus and thus reducing the nucleation rate. At low temperatures, the thermodynamic driving force for the nucleation is large due to the large undercooling, but the rate of diffusion of atoms to the nucleation site is reduced (corresponding to the decreasing mobility of atoms). Thus there is a competition between the thermodynamic and kinetic effects of the nucleation. The overall influence of temperature on the rate of nucleation is described by Maxwell-Boltzmann distribution, given by [21]:

$$\frac{n_r}{n_L} = exp\left(-\frac{\Delta G(r)}{k_B T}\right) \quad \text{or} \quad \frac{n_N}{n_L} = exp\left(-\frac{\Delta G(N)}{k_B T}\right) \tag{2.6}$$

where n_r is the number of clusters with radius r per unit volume, n_L is the number of atoms in the liquid phase, n_N is the number of clusters with radius r and contains N

atoms, k_B is the Boltzmann's constant, $\Delta G(r)$ is free energy change to form a cluster of size r, and $\Delta G(N)$ is free energy change to form a cluster of radius r that contains N atoms. To find the density of clusters that reach the critical radius r^*, n_c, Equation (2.2) can be substituted into Equation (2.6) to obtain:

$$\frac{n_c}{n_L} = exp\left(-\frac{\Delta G^{homo}}{k_B T}\right) = exp\left(-\frac{16\pi}{3}\frac{{\gamma_{SL}}^3}{{\Delta S_V}^2 \Delta T^2 k_B T}\right) \tag{2.7}$$

The rate at which this cluster grows, when one or more atoms is added, is proportional to the atomic vibration frequency, v_0, and the probability of capturing an atom at the surface, p_c. Consequently, the rate of formation of homogeneous nuclei is [14, 22]

$$I^{homo} = v_0 p_c n_L \, exp\left(-\frac{\Delta G^{homo}}{k_B T}\right) = I_0^{homo} \, exp\left(-\frac{16\pi}{3}\frac{{\gamma_{SL}}^3}{{\Delta S_V}^2 \Delta T^2 k_B T}\right) \tag{2.8}$$

In contrast to the case of homogeneous nucleation, where the number of potential sites is equal to number of atoms in the liquid, the number of sites in heterogeneous nucleation depends on the amount and type of substrates. Therefore, Equation (2.8) can be re-written for heterogeneous nucleation as:

$$I^{heter} = v_0 p_c n_p \, exp\left(-\frac{\Delta G^{heter}}{k_B T}\right) = I_0^{heter} \, exp\left(-\frac{16\pi}{3}\frac{{\gamma_{SL}}^3}{{\Delta S_V}^2 \Delta T^2 k_B T} f(\theta)\right) \tag{2.9}$$

where n_p is density of nucleation sites in the melt that provide heterogeneous nucleation to occur with wetting angle θ. The rate of heterogeneous nucleation described in Equation (2.9) predicts that as soon as the required heterogeneous undercooling is reached, the number of viable nuclei is increased immediately from zero to a maximum at n_p. This implies that, at any cooling condition, the grain number density in the final casting solely depends on a constant number of potential nucleation sites (n_p). However, this is untrue in real casting, where grain density increases significantly with increasing cooling rate.

This leads to an introduction of a distribution of nucleants with varying potency. This assumption considers that each nucleant has different numbers of available nucleation sites and requires a different characteristic temperature to activate it, i.e. there is a distribution of n_p which is a function of ΔT. As shown for athermal nucleation in section 2.1.1.2, for each size d_i of nucleant particles, heterogeneous nucleation can occur immediately below the heterogeneous nucleation temperature but the growth of nuclei is geometrically limited until $\Delta T \geq \Delta T_g(d_i)$ (Equation (2.5)). By assuming that there exists a size distribution of nucleant particles in the melt, we can find a discrete distribution for the number density of active particles that produce new grains (Δn_i) as a function of undercooling $\Delta T_g(d_i)$. This distribution is illustrated in Figure 2.4(a).

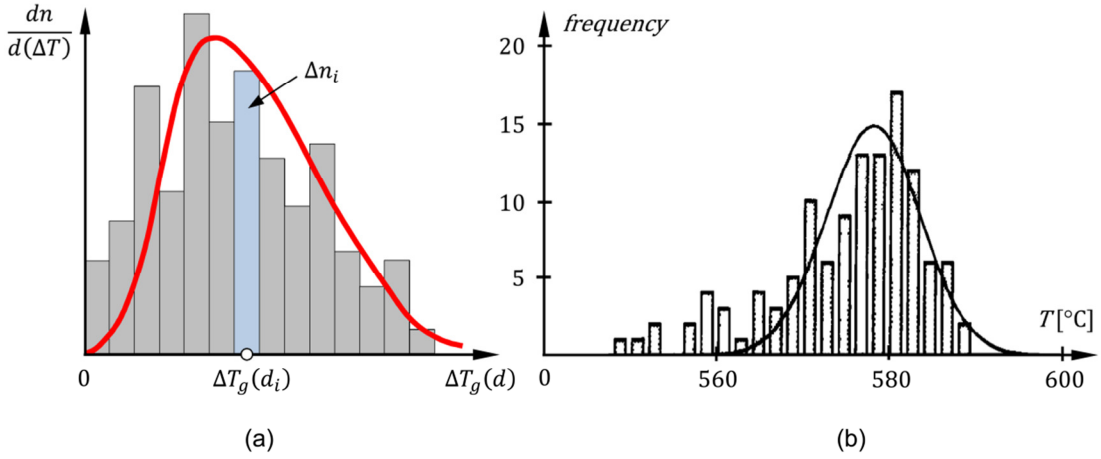


Figure 2.4 (a) The continuous distribution of active nucleation sites as a function of undercooling (after [14]); and (b) histogram and fitted Gaussian distribution of pore nucleation in Al-Cu alloy (after [23]).

For numerical simulation purposes, a continuous distribution of nucleation density can be used to approximate the discrete distribution [24] (red line in Figure 2.4a). One form that has been widely used to characterise the nucleation density as a function of nucleation undercooling is a Gaussian distribution:

$$\frac{dn}{d(\Delta T)} = \frac{n_{max}}{\Delta T_\sigma \sqrt{2\pi}} exp\left(-\frac{(\Delta T - \Delta T_M)^2}{2\Delta T_\sigma{}^2}\right) \tag{2.10}$$

where n_{max} is the maximum nucleation density, ΔT_M and ΔT_σ are the respective mean and deviation of the Gaussian nucleation undercooling distribution. Gandin and Rappaz [25] demonstrated that Gaussian distribution can be used in microstructural models for simulating grains. Lee and Hunt [26] also found a good fit between a Gaussian distribution and pore nucleation in their *in situ* directional solidification experiments (as shown in Figure 2.4b).

2.1.2 Growth kinetics

Once the nucleation of a nucleus has been completed, growth kinetics dominates the solidification process. The growth of solid is mainly driven by heat extraction from the casting which is hindered by heat transfer and solute transport in metal.

2.1.2.1 Diffusion

The following equations describe the diffusion of solute when convection effects are ignored [21] :

$$\frac{\partial C_L}{\partial t} = \nabla \cdot (D_L \nabla C_L) \quad and \quad \frac{\partial C_S}{\partial t} = \nabla \cdot (D_S \nabla C_S) \tag{2.11}$$

where C_L and C_S are solute concentrations in the liquid and solid phases, D_L and D_S are solute diffusion coefficients in the liquid and solid phases respectively. The local equilibrium condition at the solid-liquid interface gives:

$$C_S^* = k_p C_L^* \tag{2.12}$$

where k_p is the equilibrium partition coefficient. If the driving force for solidification is small, local equilibrium can be maintained [27] and thus the local solute concentration can be calculated using the lever rule:

$$C_S = C_0/[1-(1-k_p)f_S] \tag{2.13}$$

where C_0 is the initial concentration of the alloy and f_S is fraction solid. By assuming complete diffusion in the liquid phase and ignoring diffusion in the solid phase, the non-equilibrium Scheil-Gulliver equation [28, 29] can be written as:

$$C_S = k_p C_0 (1-f_S)^{(k_p-1)} \tag{2.14}$$

2.1.2.2 Undercooling

The dynamic equilibrium condition at the solid-liquid interface which is maintained during crystal growth can be expressed in terms of different undercooling contributions [30]:

$$\Delta T_{total} = T^0_{liq} - T_{actual} = \Delta T_t + \Delta T_C + \Delta T_r + \Delta T_k \tag{2.15}$$

where ΔT_{total} is the total undercooling at the interface, T^0_{liq} is the liquidus temperature at the initial concentration, T_{actual} is the actual temperature, ΔT_t is the thermal undercooling, ΔT_C is the constitutional (solutal) undercooling, ΔT_r is the curvature undercooling, and ΔT_k is the kinetic undercooling.

The thermal undercooling ΔT_t arises from the release of latent heat when a thermal gradient exists in the liquid phase. It can be calculated from the difference between the temperature at the interface T^* and the temperature (in the liquid) away from the interface T^∞, as shown in Equation (2.16).

$$\Delta T_t = T^* - T^\infty \tag{2.16}$$

The constitutional undercooling, ΔT_C, results from the compositional differences in the solid and liquid phases and can be calculated using the equilibrium phase diagram [31]:

$$\Delta T_C = T_{liq} - T^* = m_L(C_0 - C^*) = m_L C_0 \left(1 - \frac{C^*}{C_0}\right) \tag{2.17}$$

where T_{liq} is the liquidus temperature and m_L is the slope of the liquidus line.

Since capillarity relates the local equilibrium temperature of an interface between phases to the radius of curvature, the curvature undercooling ΔT_r is the difference in equilibrium temperatures between a curved interface and a planar one. It is given by Gibbs-Thomson relation [32] as follows:

$$\Delta T_r = \Gamma k \quad \text{with} \quad k = \left(\frac{1}{r_1} + \frac{1}{r_2}\right) \tag{2.18}$$

where Γ is the Gibbs-Thomson coefficient and r_1 and r_2 are the principal radii of the curvature k.

The last term on the right hand side of Equation (2.15), the kinetic undercooling ΔT_k, is estimated via rate theory, i.e. by calculating the transition rates of atoms from the liquid attaching themselves to the growing solid and vice versa. Assuming the kinetic undercooling is negligible, total undercooling would consist of three parts, namely:

$$\Delta T = \Delta T_t + \Delta T_C + \Delta T_r \tag{2.19}$$

2.1.2.3 Solid-Liquid interface

The development of melt-grown crystals into faceted and non-faceted morphologies is strongly dependent on the kinetics of atom attachment at the solid-liquid interface. Most metals solidify with microscopically smooth interfaces (Figure 2.5a) and exhibit non-faceted structures, whereas semiconductors and intermetallic phases typically form crystals having microscopically planar and angular surfaces (facets) (Figure 2.5c).

In non-faceted growth, structure and bonding of atoms in the liquid state and in the solid state are quite similar. Therefore, the transition from one phase to another is very gradual and occurs over some distance (6-8 atomic layers in thickness [33]), resulting in an atomically diffuse (rough) interface, as shown in Figure 2.5b. This type of interface exposes many favourable sites for the attachment of atoms arriving from the liquid and thus only requires small undercooling (as shown schematically in Figure 2.5a, the interface will grow at a temperature close to T_m). The solid-liquid interfacial energy (γ_{SL}) is typically nearly isotropic.

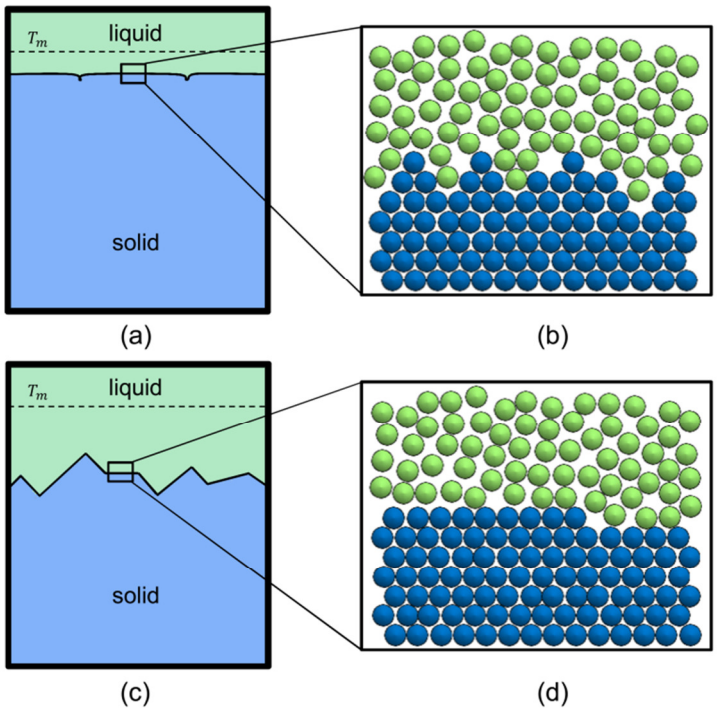


Figure 2.5 Types of solid-liquid interface: (a-b) non-faceted interface and (c-d) faceted interface. Images (a, c) represent interfaces at microscopic scale (after [21]) whereas images (b, d) represent interfaces at atomic scale (after [14]).

In semiconductors, compounds and intermetallic phases, the greater difference in structure and bonding of atoms in liquid and solid states leads to a sharp transition between phases, as shown in Figure 2.5d. This atomically smooth (sharp) interface exhibits little tendency for the attachment of atoms and may require an additional local undercooling. The growth becomes more difficult since a very high Gibbs free energy is

anticipated to position one atom/molecule at the solid surface. Atoms are usually attached to solid at steps and may sometimes prefer defects, e.g. twinning and screw dislocations, to ease their attachment. The interfacial energy (γ_{SL}) is typically anisotropic and hence very likely to exhibit a marked anisotropy in growth rate, resulting in a faceted morphology of the solid phase.

In order to predict crystallisation behaviour, a criterion based on latent heat of fusion and melting temperature has been widely used. This criterion was developed by Jackson [34] and can be described as:

$$\alpha = \frac{L_f}{RT_m} = \frac{\Delta S_f^m}{R} = \frac{S_L^m - S_S^m}{R} \tag{2.20}$$

where L_f is latent heat of fusion, R is ideal gas constant, ΔS_f^m is molar entropy of fusion, S_L^m is molar entropy of liquid phase, and S_S^m is molar entropy of solid phase. A value of the α-factor less than 2 (i.e. a small difference of molar entropy between two phase) predicts a growth of a non-faceted crystal form, while a faceted growth morphology is anticipated when $\alpha > 2$.

2.2 Fe-rich Intermetallics

Iron (Fe) is a common impurity in aluminium alloys and is usually considered detrimental to casting quality and production yield. Since the solubility of Fe in liquid Al is high (≈1.8 wt.%), Fe can enter molten aluminium in many ways, such as dissolution of Fe from steel casting tools, e.g. ladles, during the casting process [35]. Primary aluminium, which is produced from bauxite, typically contains 0.03-0.15 wt.%Fe [4]. In secondary aluminium, additional Fe impurities can be picked up from aluminium scrap during the recycling process, resulting in an increased amount of Fe-content up to 0.4-0.8(wt.%) in Al-Si alloys [4, 36]. This amount of Fe is sufficient to produce various forms of secondary Fe-rich intermetallic phases owning to its low

maximum equilibrium solid solubility (≈0.04 wt.%Fe) [4, 37]. These Fe-rich intermetallics, particularly a highly faceted plate-like β-Al_5FeSi intermetallic phase, can severely degrade the mechanical properties of casting components such as ductility [38], tensile strength [39], pitting corrosion resistance [40] and fatigue life [6]. It was found that fatigue cracks can initiate on the surface of the large plate-like intermetallics and then propagate along these brittle intermetallic phases [6]. Furthermore, the β-intermetallic has also been reported to degrade castability [9] and contribute to the formation of other solidification defects such as porosity [8] and hot tearing [7]. These topics regarding to defect formation will be reviewed in the following sections.

2.2.1 Intermetallic phases in Al and Al-Si alloys

In the binary Al-Fe system, the equilibrium solid concentration of Fe in aluminium is about 0.04 wt.% at the eutectic temperature of 655°C (928 K), as shown in Figure 2.6. Above this limit, Fe segregates during solidification and forms intermetallic compounds with Al and other elements that may be present in the alloys. Various types of intermetallic compounds can be observed in Al-Fe alloys. The equilibrium θ-Al_3Fe (also reported as θ-$Al_{13}Fe_4$) and metastable Al_6Fe phases were reported to form a eutectic with the Al phase [5, 41]. Typical microstructures of these two intermetallic phases are very similar and a transformation from Al_6Fe to $Al_{13}Fe_4$ can occur under equilibrium conditions [42]. In a non-equilibrium condition, such as real casting, many more metastable intermetallic phases can be found. These metastable phases are usually referred as Al_xFe ($x \approx 5$-6) or Al_mFe ($m \approx 4$-4.5) and the differences in their forms are very dependent on the cooling conditions [43, 44].

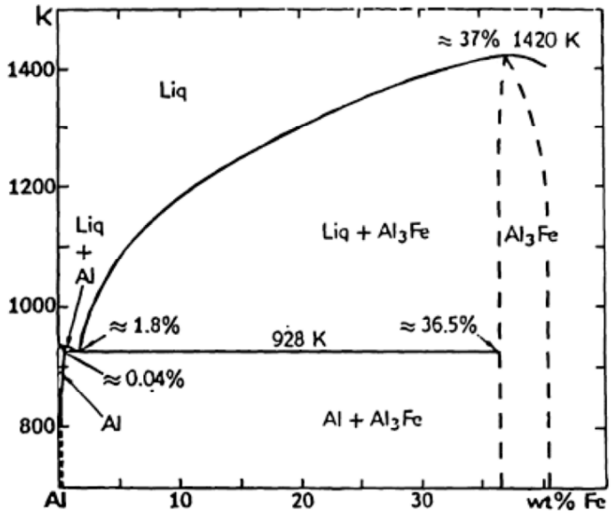
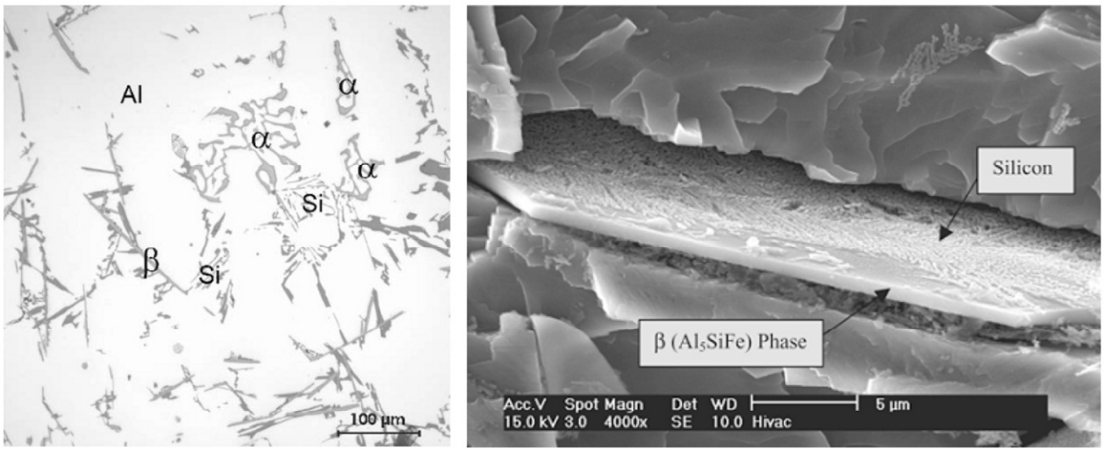


Figure 2.6 Al-rich corner of the equilibrium Al-Fe binary phase diagram, from [44].

In the Al-Si-Fe system, many forms (classified by their crystal structures and final morphologies) of Fe-rich intermetallic phases have been identified, including α (Al_8Fe_2Si and $Al_{15}(Fe,Mn)_3Si_2$), β (Al_5FeSi), π ($Al_8Mg_3FeSi_6$), δ (Al_4FeSi_2), γ (Al_3FeSi) and θ ($Al_{13}Fe_4$) [5, 43, 45, 46]. Among these phases, α-intermetallics and β-intermetallics are considered as the most important Fe-rich phases in Al-Si alloys. Since α-intermetallic has a more compact morphology (e.g. Chinese script and polygon) compared to plate-like β-intermetallic, as shown in Figure 2.7, it was reported to be less harmful to the mechanical properties.



(a) (b)

Figure 2.7 Typical 2-D morphologies of script-like α-Al_8Fe_2Si and plate-like β-Al_5FeSi from (a) optical microscopy (from [47]) and (b) scanning electron microscopy (SEM) (from [48]).

The α-Al_8Fe_2Si phase is hexagonal in a high purity Al-Si-Fe system. The minor additions of alloying elements, such as Mn, Cr, and V, promote a body-centered cubic (bcc) structure of the α-$Al_{15}(Fe,Mn)_3Si_2$ and α-AlFeSi phases [44]. Dinnis *et al.* [49] used serial sectioning method to observe a 3-D morphology of the $Al_{15}(Fe,Mn)_3Si_2$ phase and found that it exhibits two distinct morphologies. A large polyhedron crystal forms at the core of the particle when it first grows as primary phase. Once Al-rich dendrites have formed, a structure with highly convoluted arms subsequently occurs around existing polyhedral crystal as a coupled eutectic with Al. The 3-D morphology of this $Al_{15}(Fe,Mn)_3Si_2$ phase is shown in Figure 2.8a.

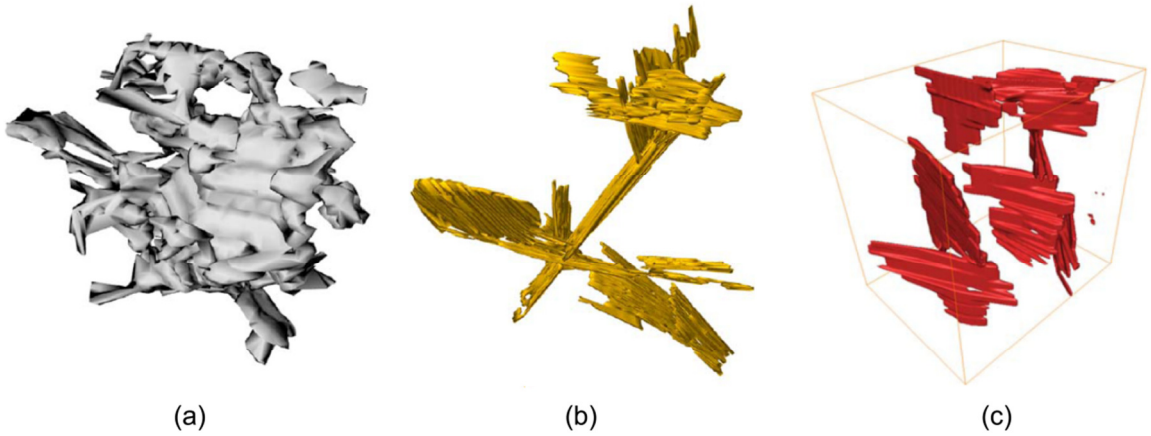


Figure 2.8 3-D morphologies of (a) α-$Al_{15}(Fe,Mn)_3Si_2$ and (b-c) *β*-Al_5FeSi intermetallics. Note that the 3-D renders in (a-b) were obtained from serial sectioning method (from [49]) whereas (c) were obtained from x-ray tomography (from [11]).

Although it is clear that needle-like *β*-Al_5FeSi intermetallic in 2-D (Figure 2.7a-b) is actually a complex plate-like structure in 3-D (Figure 2.8b-c), the crystal structure of this *β*-intermetallic remains a debated topic. Murali *et al.* [50] reported that *β*-Al_5FeSi is monoclinic with a=0.5792 nm, b=1.2273 nm, c=4.313 nm, and *β*=98.93°. Romming *et al.* [51] found an agreement that *β*-intermetallic ($Al_{4.5}FeSi$) is monoclinic but they reported with different lattice parameters (a=0.6161 nm, b=0.6175 nm, c=2.081 nm, and *β*=90.42°). In contrast, Zheng *et al.* [52] found that *β*-intermetallic is orthorhombic with a=0.618 nm, b=0.620 nm, and c=2.08 nm. Kral [46] claimed that the

β-intermetallic is actually consistent with the tetragonal δ-Al_3FeSi_2, rather than monoclinic or orthorhombic. To determine the fault structure of β-intermetallic, Hansen *et al.* [53] extended the study from Romming *et al.* [51] by performing a combined techniques of synchrotron powder diffraction, electron diffraction and high resolution electron microscopy. They proposed that periodic faults exist in the monoclinic structure.

In the Al-Si-Cu-Fe system at low Cu concentration (<5.8 wt.%Cu), the thermodynamics of the Fe-rich intermetallic formation in quaternary Al-Si-Cu-Fe systems are nearly identical to those in the ternary Al-Si-Fe alloys. This is due to the presence of Cu which only forms an Al/Al_2Cu eutectic at the end of solidification (~510°C) and does not affect the formation of Fe-rich intermetallics [4]. Salvo *et al.* [54] recently confirmed experimentally that the addition of Cu into Al-7.5Si-0.75Fe (wt.%) only lowers the nucleation temperature of the β-Al_5FeSi intermetallic but does not change the formation mechanism nor morphology of the β-intermetallic, as shown in Figure 2.9.

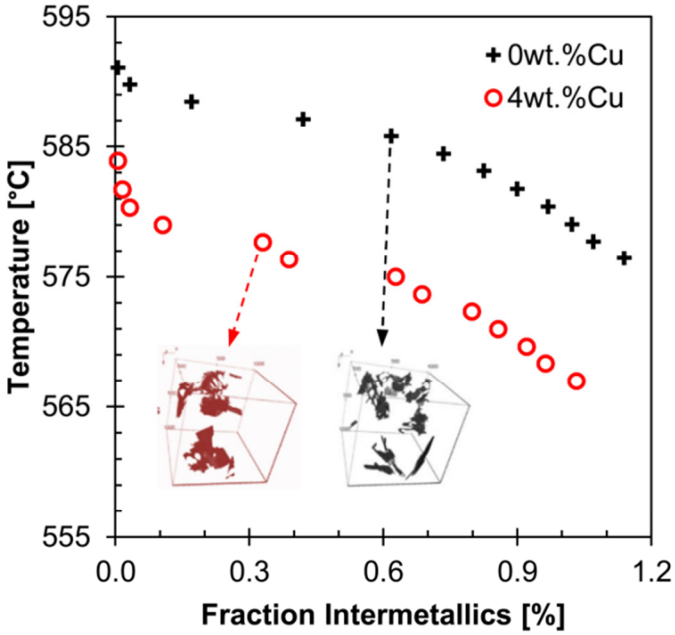


Figure 2.9 Volume fraction of β-Al_5FeSi intermetallic as a function of temperature, after [54].

2.2.2 Reactions governing β-Al_5FeSi intermetallic formation

Many attempts have been made to understand the thermodynamics of Fe-rich intermetallic phase formation during equilibrium solidification of Al-Si alloys. The Al-Si-Fe phase diagram is very complicated. As can be seen in Figure 2.10a, many forms of Fe-rich intermetallic phase can occur via various reactions during solidification. Although there is still some controversy on the availability of stable intermetallic phases as well as the temperature and composition of the invariant reactions, key eutectic and peritectic reactions have been experimentally confirmed [5, 36, 44, 47, 55, 56]:

(1)	Liquid	$\rightarrow$	α-Al + θ-$Al_{13}Fe_4$
(2)	Liquid + θ-$Al_{13}Fe_4$	$\rightarrow$	α-Al + β-Al_5FeSi
(3)	Liquid	$\rightarrow$	α-Al + α-Al_8Fe_2Si
(4)	Liquid + α-Al_8Fe_2Si	$\rightarrow$	α-Al + β-Al_5FeSi
(5)	Liquid	$\rightarrow$	α-Al + β-Al_5FeSi
(6)	Liquid	$\rightarrow$	α-Al + β-Al_5FeSi + Si

Allen *et al.* [55] used DSC and SEM to investigate 1xxx aluminium alloy (<0.2 wt.% Si) and found that the θ-$Al_{13}Fe_4$ intermetallic may occur via reaction (1). Sha *et al.* [56] used DSC, SEM and TEM to study intermetallic phase formation during directional solidification of 6xxx aluminium alloys (Al-0.6Si-0.8Mg-0.3Fe, wt.%). The experiments were performed at low growth velocities in a Bridgeman furnace. They observed a triple phase junction between α-Al, θ-$Al_{13}Fe_4$ and β-Al_5FeSi, suggesting that β-Al_5FeSi formed as a result of quasi-peritectic reaction (reaction 2). Backerud *et al.* [57] used cooling curves and Sperry [58] studied quenched microstructure of 6xxx aluminium specimens to confirm that an α-Al_8Fe_2Si intermetallic having Chinese script form can develop directly from the melt via reaction (3). Mulazimoglu *et al.* [59] not only observed the α-Al_8Fe_2Si intermetallic in the microstructure of a similar alloy system, but also found a needle-like β-Al_5FeSi intermetallic. They revealed that, in a few cases,

β-Al_5FeSi appeared in contact with α-Al_8Fe_2Si. Therefore, they hypothesized that the β-Al_5FeSi intermetallic formed via a quasi-peritectic decomposition (reaction 4) of the α-Al_8Fe_2Si intermetallic. Sha *et al.* [60] extended their directional solidification studies [56] and observed two types of composite particles: β-Al_5FeSi/α-Al_8Fe_2Si and β-Al_5FeSi/θ-$Al_{13}Fe_4$. They concluded from these results that two quasi-peritectic reactions, shown in 2 and 4, were likely to occur. However, no real-time observation of intermetallic phase formation has yet been made in 1xxx or 6xxx Al wrought alloys.

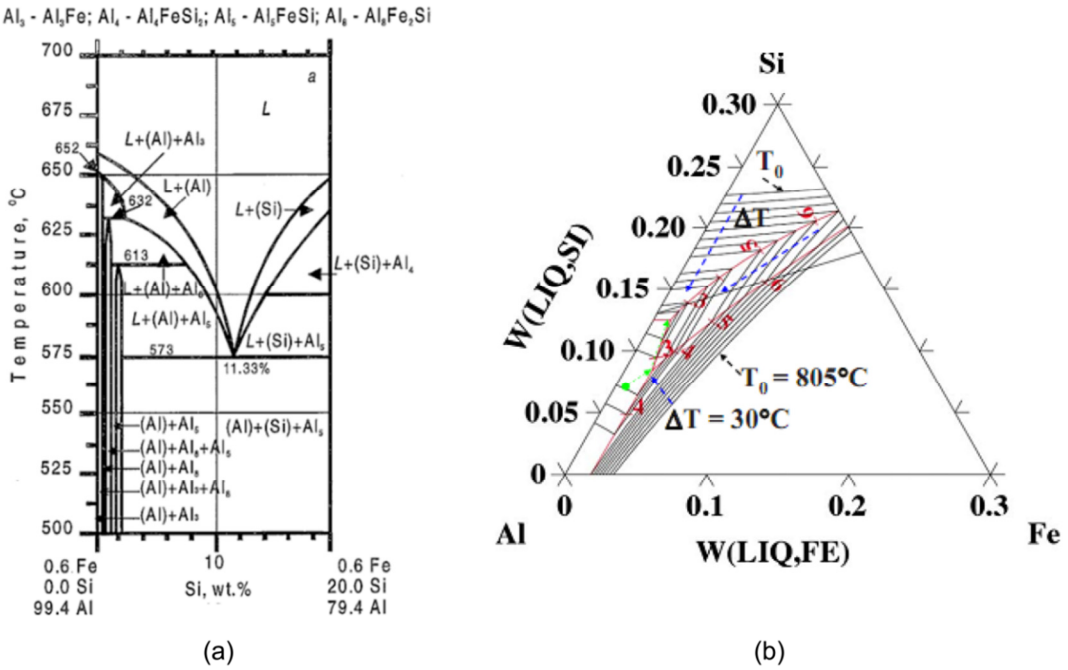


Figure 2.10 (a) Polythermal section of the Al-Si-Fe phase diagram at 0.6wt.%Fe (from [4]); and (b) liquidus projection of Al–Si–Fe system, where isothermal lines are shown in dark and red lines correspond to the invariant reactions (from [11]).

Lu and Dahle [47] carried out comprehensive studies (thermal analysis, SEM and EPMA) on both quenched and fully solidified microstructures of hypoeutectic Al-Si cast alloys (Al-7Si, wt.%) with and without the addition of alloying elements (e.g. Mn, Sr, P). In the base alloy (Al-Si-Fe), they proposed that the β-Al_5FeSi intermetallic can form via two eutectic reactions. At low Fe content (0.3 wt.%Fe), formation of β-Al_5FeSi intermetallic occurs through a ternary eutectic reaction (reaction 6). At higher Fe content (0.7 wt.%Fe), β-Al_5FeSi intermetallic form via both binary and ternary eutectic

reactions (reactions 5 and 6, respectively) but the majority of the β-intermetallic precipitates as a result of a binary reaction. No other form of intermetallic phase was found in the base alloy. However, they reported that small additions of Mn can suppress the formation of β-Al_5FeSi and can promote a script-like α-Al_8Fe_2Si intermetallic. Ashtari *et al.* [61] also reported that only the β-Al_5FeSi intermetallic existed in the fully solidified microstructure of the A319 alloy (Al-7.3Si-3.5Cu-0.6Fe, wt.%).

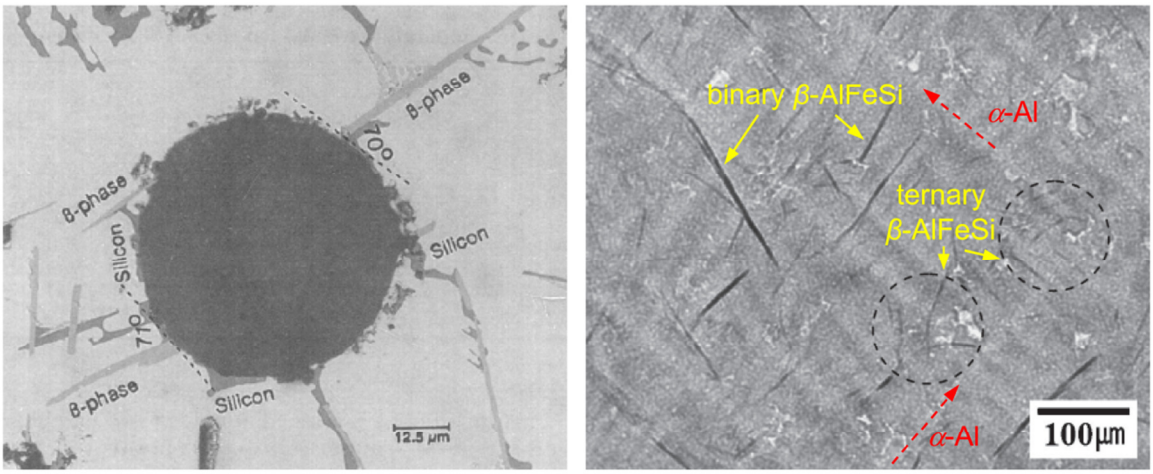
Du *et al.* [62] formulated a comprehensive thermodynamic database for the ternary Al-Si-Fe system. By using this database, Wang *et al.* [11] calculated the solidification path for an A319 alloy (Al-7.5Si-0.8Fe, wt.%, ignoring Cu content) which is shown as a green spot and dashed green line in Figure 2.10b. Although, they predicted that reactions 2 and 6 (numbers 4 and 3 in Figure 2.10b respectively) are thermodynamically favoured, they found in their *in situ* synchrotron x-ray radiography [36] that the β-Al_5FeSi intermetallic formed via two eutectic reactions as suggested by Lu and Dahle (reactions 5 and 6). In this first direct observation of intermetallic formation, only the intermetallic phase in the form of β-Al_5FeSi was observed during solidification of an Al-7.5Si-3.5Cu-0.8Fe (wt.%) alloy. Recently, Terzi *et al.* [63] carried out an *in situ* synchrotron tomographic experiment to study the evolution of intermetallic formation in 3-D during solidification of an Al–8Si–4Cu–0.8Fe (wt.%) alloy. The result exhibited a good agreement to prior studies [36, 47, 61] that eutectic reactions 5 and 6 are the key reactions for producing β-Al_5FeSi intermetallic in hypoeutectic Al-Si cast alloy.

2.2.3 Formation of β-Al_5FeSi intermetallics

The formation of the β-Al_5FeSi intermetallic is very complicated. Many nucleation and growth mechanisms have been reported in the literature.

2.2.3.1 Nucleation mechanisms

A few studies have been made to understand the nucleation mechanism of the *β*-intermetallic. Sigworth [64] proposed that the presence of phosphorus (P) in the melt leads to the nucleation of the *β*-intermetallic on aluminium phosphide (AlP) nucleant particles. Campbell and several authors [65-67] suggested that aluminium oxide (Al_2O_3) is also a potent nucleation site. They found that both the α-intermetallic and *β*-intermetallic can nucleate and grow on the wetted surfaces of double oxide films, known as bifilms, entrained in the melt. Miller *et al.* [68] verified the role of oxides in nucleating *β*-intermetallics by deliberately adding α-Al_2O_3 and $MgAl_2O_4$ oxide particles directly to the melt. Their results indicated that the *β*-intermetallic associated with both oxides added, agreeing with a previous hypothesis by Campbell. Narayanan *et al.* [69] externally added two types of oxides, γ- and α-aluminium oxides, to the melt to study nucleation behaviour of the *β*-intermetallic during solidification of A319 alloy. They reported that γ-aluminium oxide, both at the surface and within the melt, acted as good nucleation sites for the *β*-intermetallic (as shown in Figure 2.11a), while α-aluminium oxide particles were not favourable nuclei for the *β*-intermetallic. A recently published *in situ* experiment [63] observed all four nucleation events of the *β*-intermetallic at the specimen surface. They suggested based on this observation that the γ-Al_2O_3 formed at the specimen surface is an active nucleant for the *β*-intermetallic. In contrast, Khalifa *et al.* [70] observed that γ-Al_2O_3 oxides were potent nuclei for α-Al but exhibited poor potency to nucleate the *β*-intermetallic. They found that a TiB_2 grain refiner can promote nucleation of Fe-rich intermetallics, confirming other studies [71, 72].



(a) (b)

Figure 2.11 (a) Nucleation of *β*-intermetallic on γ-aluminium oxide (from [69]); and (b) radiograph showing *β*-intermetallic oriented parallel to near-by dendrite arms (from [73]).

Sha *et al.* [56] and Terzi *et al.* [63] reported that the *β*-intermetallic nucleated independently from the α-Al phase with no observation of a unique orientation relationship. However, it has been clearly observed that the strong anisotropic growth of the intermetallic always maintains the initial orientation first defined in the nucleation event [56]. Recently, Kim *et al.* [73] used x-ray radiography to observe *in situ* uni-directional solidification of an Al-9.5Si-3Cu-1.2Fe (mass%) alloy at 1 Hz. They found that *β*-intermetallics have a tendency to orient in the directions parallel to the near-by dendrite arms, as shown in Figure 2.11b, suggesting a strong dependency of *β*-intermetallic nucleation on Fe supersaturation around α-Al dendrites.

2.2.3.2 Growth mechanisms

The *β*-Al_5FeSi intermetallic was observed to exhibit faceted platelet morphology with a main facet plane of (001) [53, 56, 74]. Using high resolution electron microscopy (HREM), Mulazimoglu *et al.* [59] revealed that *β*-Al_5FeSi is highly faulted and has a high incidence of twinning along the (001) plane of faceted plate (Figure 2.12a). This was in good agreement with the observation of twin diffraction spots and streaks in typical selected area diffraction patterns (SADPs) of *β*-Al_5FeSi [53]. The presence of

these twin planes in parallel to the growth direction provides sites for atom attachment, thus promoting growth. This growth mechanism, which is referred to as "twin plane re-entrant edge growth" [59], strongly restricts the bending or twisting of the β-Al_5FeSi intermetallic during the growth, resulting in the final plate-like morphology. Furthermore, Sha *et al.* [60] observed steps on a (001) faceted boundary of β-Al_5FeSi in their high resolution transmission electron microscopy (HRTEM) image, as shown in Figure 2.12b. They proposed based on this observation that both twin plane re-entrant edge growth and step growth denominate the growth mechanisms of a β-Al_5FeSi intermetallic. However, no *in situ* observation has yet possible to be made.

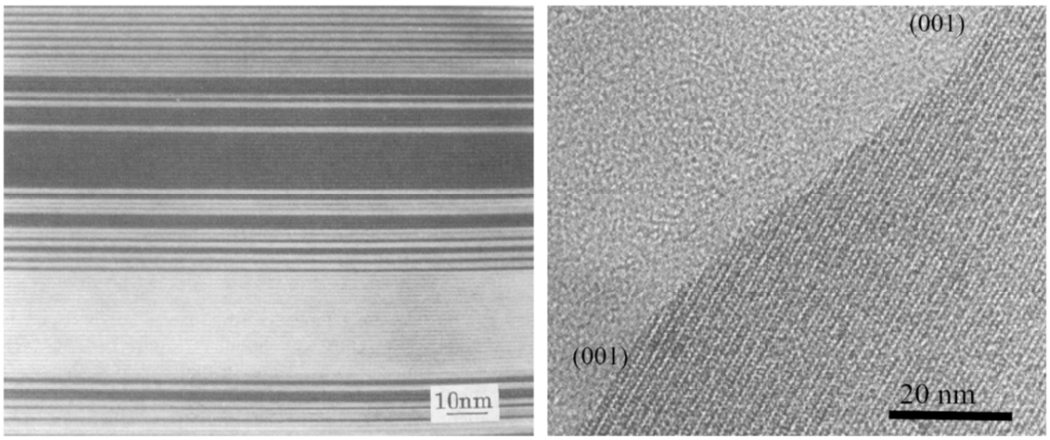


Figure 2.12 (a) HREM image β-Al_5FeSi intermetallic showing twinning (from [59]); and (b) HRTEM image showing steps on β-Al_5FeSi faceted boundary (from [60]).

In order to reveal the complexity of β-Al_5FeSi intermetallic growth, recent work [36, 63] has focused on the use of *in situ* methods. Fast *in situ* x-ray radiography [36] (acquired at 2 Hz) has shown an initial lateral growth spurt after nucleation of the β-intermetallic, followed by a slow thickening during the later stages of solidification. The growth evolution of β-intermetallic is shown in Figure 2.13a. The rapid lateral growth of β-intermetallic in the initial stage (Figure 2.13a, I-II) was thought to be a result of Fe supersaturation in the interdendritic liquid. The average growth velocity of β-intermetallics during this lateral growth stage was 34±20 μm/s.

In the later stages, the growth in the favourable directions is restricted by physical impingement of the β-intermetallic on surrounding aluminium dendrites. The growth can only continue via thickening in the direction normal to the plate faces (Figure 2.13a, III). This coupled lateral growth and thickening mechanism is similar to the ledge-wise growth mechanism proposed by Laird and Aaronson [75].

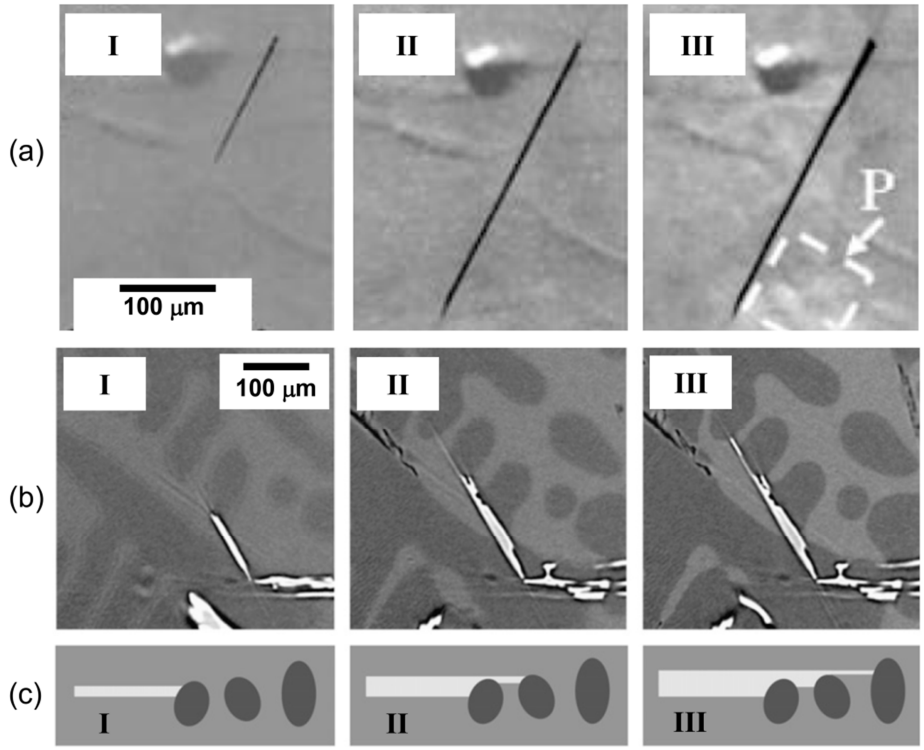


Figure 2.13 (a) Growth evolution of β-intermetallic from *in situ* x-ray radiography, after [36]; (b) tomography images showing erratic growth of β-intermetallic, after [63]; and (c) schematics of β-intermetallic growth mechanism proposed by [63]. Insets I-III in (a) represent the temperatures of 564°C, 558°C and 531°C respectively, whereas insets I-III in (b) show the time steps of 31.3min, 38.0min and 39.9min, respectively, after the first scan.

A subsequent *in situ* 3-D synchrotron tomographic experiment confirmed both the initial rapid growth in the lateral direction and the slow thickening rate of the β-intermetallics [63]. Based on the observation shown in Figure 2.13b, they suggested an erratic behaviour of β-intermetallic growth, as shown in Figure 2.13c. The intermetallic plate first grew quickly in a lateral direction until impinging on obstructing dendrites (Figure 2.13b-c, I). The growth then followed by slowly increasing its thickness along

the dendrite surfaces (Figure 2.13b-c, II). Once passed the obstacle, the fast growth resumed in the preferential lateral direction until the next impingement (Figure 2.13b-c, III).

In this previous tomographic experiment, adjacent 3-D scans were captured every 57 s at a cooling rate of 1.4˚C/min. Although the use of 3-D tomographic imaging provided improved insights into the growth mechanisms of the *β*-intermetallic as compared to the 2-D radiography techniques and post-mortem studies, the nucleation events and growth kinetics remain unclear due to the lack of temporal resolution. One main debating topic is the intermetallic-intermetallic interaction. Terzi *et al.* [63] hypothesised based on their 3-D tomographic observation that the mechanism of complex branching might take responsibility for creating very complex interconnected *β*-intermetallic plates, as shown in Figure 2.14. They also suggested that these branching events were not crystallographically related since a broad range of branching angles were observed. This result is contrary to other studies [11, 49] which suggested that the network of interconnected *β*-intermetallic plates formed through impingement of individual intermetallic plates.

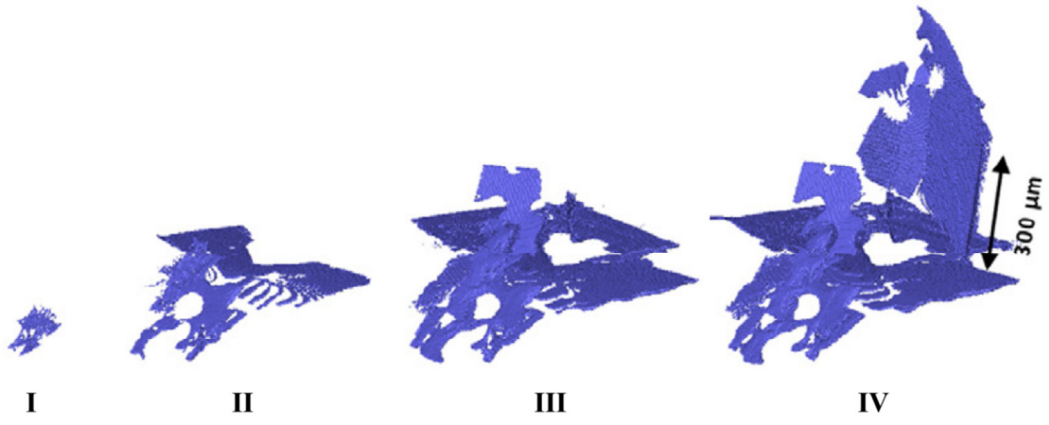


Figure 2.14 Evolution of an *β*-intermetallic via growth and branching mechanisms, after [63]. Insets I-IV show time of 27.6min, 28.5min, 30.4 and 32.3min after the first scan, respectively.

2.2.4 Modification of β-Al_5FeSi intermetallics

As discussed earlier, the presence of Fe-rich intermetallic phases leads to deleterious effects on mechanical properties and detrimentally impact castability of Al-Si alloys [9, 45, 76]. Since Fe impurity is inevitable and is very difficult to remove economically from the melt, various studies have been made in an effort to lessen the deleterious effect of Fe-rich intermetallics. It was found that the extent to which intermetallics adversely affect the mechanical properties of the castings depends strongly on their morphology and size [9]. For example, plate-like β-Al_5FeSi intermetallic is considered to be more harmful than the more compact form of script-type intermetallics. Furthermore, the larger the intermetallic particle, which is strongly influenced by Fe content and cooling conditions [77, 78], the more detrimental it is likely to be. Two major approaches have been widely used in order to neutralise the harmful effects of β-Al_5FeSi intermetallics: (1) addition of alloying elements and grain-refiners, such as Mn, Sr, Cr, Co, TiB_2, and (2) controlling cooling conditions. In the former case, morphology of β-Al_5FeSi intermetallic can be altered to less harmful and more compact forms, such as script-like α-Al_8Fe_2Si or α-$Al_{15}(Fe,Mn)_3Si_2$ intermetallics, where in the latter case, the size of the β-intermetallic in the microstructure can be refined or made smaller.

Many types of alloying additions have been studied to measure the effectiveness of morphological modification. Shabestari *et al.* [65, 79] reported that the addition of 0.9 wt.% Mn to the Al-Si-Fe alloy causes the fragmentation of the β-Al_5FeSi. At higher Mn levels, the script-like α-$Al_{15}(Fe,Mn)_3Si_2$ was formed instead of the plate-like β-Al_5FeSi. In the report, they also recommended a ratio of the compositions of Fe to Mn to be 2:1. Gustafsson *et al.* [80] and Mahta *et al.* [81] reported that an Fe:Cr ratio of 3 is required to promote the formation of script-like α-$Al_{13}(Fe,Cr)_4Si_4$ instead of β-Al_5FeSi and an optimum ratio of Fe:Co of approximately 1 is recommended to suppress the formation of

β-intermetallic plate. Many studies [79, 82, 83] reported that caution has to be taken when alloying with Mn and Cr since a hard complex intermetallic multi-component phase, $Al_{15}(Fe,Mn,Cr)_3Si_2$, is likely to be formed. This phase tends to agglomerate into what has been termed a "sludge", and has been shown to adversely affect the overall properties of cast components. Ashtari *et al.* [61] reported that Potassium (K) is also very effective in modifying plate-like β-intermetallic to script-like α-intermetallic. The addition of Sr to modify the morphology of Fe-intermetallics has also been an interesting topic for many studies. It was reported that Sr at low level (~250-350ppm) is very effective, particularly at low cooling rates, in refining the β-intermetallic (i.e. reducing the size of intermetallic) through fragmentation and dissolution mechanisms [77, 78, 84, 85]. At higher Sr concentrations, complete conversion of β-intermetallic to star-like (dendrite) morphology was observed [65]. Lu and Dahle [47] found that addition of Sr produced a little finer β-intermetallic but no transformation was observed.

Cooling conditions can also influence the formation of the β-intermetallic. At high cooling rates, segregation of Fe is limited and thus the formation of the β-intermetallic, resulting in smaller β-intermetallic particles [9, 10, 86]. Liu *et al.* [77] reported that smaller dendritic arm spacing (DAS) obtained at high cooling rate could physically restrict the growth of β-intermetallic in the interdendritic spaces, reducing the final length of the β-intermetallic. They also suggested that at a high cooling rate, the maximum solubility of Fe in an aluminium matrix will increase, leading to finer β-intermetallic particles. It has also been reported that the formation of Fe containing intermetallics in Al-Si-Fe alloys can be suppressed, refined or modified using rapid solidification processes [87, 88].

2.3 Permeability

Solidification defect formation during casting processes is closely linked with fluid flow in the mushy zone since the resistance to flow through the solid network causes a pressure drop in the liquid that can contribute to porosity formation [89], macrosegregation [90], and hot tearing [91, 92]. One parameter to characterise fluid flow in the mushy zone is permeability, i.e. a tensor measure of the ease of fluid flow through the solid network [93]. Permeability is a critical parameter in macroscopic casting models for predicting defects and is related to the geometry of the liquid channels and the grain morphology [94, 95].

2.3.1 Permeability measurements

In semi-solid aluminium alloys, flow of liquid metal through the evolving interdendritic channels is driven by the nearly seven percent volume change [96] associated with the liquid to solid phase transformation. The permeability of such alloys has traditionally been measured using an apparatus that applies a pressure gradient to a partially solid specimen while measuring the discharge velocity of a working fluid. Piwonka and Fleming [97] used this technique to measure, for the first time, permeability in solidifying Al-4.5Cu (wt.%). Apelian *et al.* [98] performed similar technique using water as fluid to measure permeability in Al-Si alloys. Using eutectic liquid as the fluid, Nasser-Rafi *et al.* [99] successfully examined the permeability of directional solidified Pb-20Sn (wt.%) alloy with various primary and secondary dendrite arm spacings. This work investigated both flow parallel and normal to primary dendrites at a fraction of liquid between 0.19 and 0.29. Poirier [94] later published extended results. Murakami *et al.* [100, 101] used a translucent borneol-paraffin organic alloy to provide permeability measurements in columnar dendritic structures with various primary and secondary dendrite arm spacings, for flow both parallel and

normal to the primary dendrite direction. Duncan *et al.* [102], Han *et al.* [103] and Nielsen *et al.* [104] investigated permeability in Al-Cu and Al-Si alloys with equiaxed microstructures. Studies using this type of device have focused on measuring the near-eutectic permeability of solidifying structures while attempting to reduce errors associated with the tendency of the microstructure to change during testing due to coarsening and diffusional processes [105].

2.3.2 Permeability models

Alternatively, it is possible to develop predictive numerical models assessing permeability as detailed in [106, 107]. Numerical models solve Stokes equations on a domain representing the interdendritic liquid. The advantage with using a simulated microstructure is that the permeability evolution as a function of fraction of solid can be easily studied for different grain sizes and morphologies. However, the main challenge with this method is the geometry of the domain itself. Since permeability is a characteristic of porous media that is based on the geometry of the flow channels, i.e. channel width, surface area and tortuosity, an accurate computational domain is critical for numerical determination of this parameter [108]. Recently, much attention has focused on using 3-D x-ray tomographic imaging to acquire representative semi-solid geometry for assessment of permeability during equiaxed-dendritic [106] and columnar [109] solidification and at alloy compositions both near-eutectic [107, 108] and low-eutectic [110] as a function of solid fraction. In these recent studies, tomographic imaging was performed on quenched specimens followed by image analysis to distinguish the eutectic (interdendritic liquid) from the dendrite structures. The results have shown a generally good agreement between the simulated permeability and experimental reference data [106, 109].

Numerically, permeability is defined by Darcy's law as [111]:

$$v_L = -\frac{K}{\mu_L}(\nabla P_L - \rho_L g) \tag{2.21}$$

where K is the permeability of the porous medium, μ_L is the viscosity, v_L is superficial flow velocity of the liquid, ∇P_L is the pressure gradient in the liquid, ρ_L is the liquid mass density and g is the acceleration due to gravity. For equiaxed dendritic structures, the isotropic Carman-Kozeny equation [112] is most-often adopted to approximate permeability in semi-solids. Carman-Kozeny equation, derived from solution of Poiseuille equation, is defined as:

$$K = \frac{(1-f_S)^3}{k_C S_V^2 f_S^2} \tag{2.22}$$

where f_S is fraction solid, S_V is surface area of solid-liquid interface per unit volume of solid, and k_C is Carman-Kozeny constant. It was found that k_C is ~3 for equiaxed dendritic [113] and ~5 for granular microstructures [114].

However, for columnar-dendritic structures, the permeability is anisotropic due to the directional nature of the dendrite arms [100], and thus Carman-Kozeny is not appropriate. To investigate anisotropy in permeability, Poirier [94] used multilinear regression analysis of experimental data to propose an empirical relationships based on the Blake-Kozeny equation,

$$K_p = C_1 \frac{f_L^3 \lambda_1^2}{1-f_L} \tag{2.23}$$

$$K_n = C_2 \left(\frac{\lambda_1}{\lambda_2}\right)^p \frac{f_L^3 \lambda_1^2}{(1-f_L)^n} \tag{2.24}$$

where K_p and K_n are the permeabilities in the directions parallel and normal to the primary dendrites, λ_1 and λ_2 are the primary and secondary dendrite arm spacings, f_L is the fraction liquid and C_1, C_2, p, n are fitting constants calculated from the regression analysis. Schneider *et al.* [115] and Heinrich *et al.* [116] continued work in this area and

proposed multi-expressions for different ranges of fraction liquid. In an alternative approach, Santos and Melo [117] used the Hagen-Poiseuille flow equation and derived a physically-based permeability expression for flow both parallel and normal to the primary dendrite arms as:

$$K_p = \frac{f_L^2 \lambda_1^2}{8\pi\tau_p^3} \tag{2.25}$$

$$\tau_p = 1 + \left(\frac{\lambda_2}{\lambda_1}\right) + \left(\frac{\lambda_2}{\lambda_1}\right)^{f_L} + \left(\frac{\lambda_2}{\lambda_1}\right)^{f_L^2} + \left(\frac{\lambda_2}{\lambda_1}\right)^{f_L^3} \tag{2.26}$$

$$K_n = \frac{f_L^2 \lambda_1 \lambda_2}{8\pi\tau_n^3} \tag{2.27}$$

$$\tau_n = 1 + \left(\frac{\lambda_2}{\lambda_1}\right) + \left(\frac{\lambda_2}{\lambda_1}\right)^{f_L} + \left(\frac{\lambda_2}{\lambda_1}\right)^{f_L^2} \tag{2.28}$$

where τ_p and τ_n are the tortuosities of the interdendritic liquid channels in the directions parallel and normal to the primary dendrites. In both cases, the permeability predictions were found to be in good agreement with experimental data.

2.3.3 Particle blockage

During solidification of most commercial alloys, intermetallics and/or inclusions would be expected to be present in the solidifying microstructures, typically in the interdendritic regions where the remaining liquid metal must flow. The existence of these growing particles may block the fluid path and make the flow even more difficult. In Ni-based superalloys, TiC carbide precipitation was reported to reduce viscosity and permeability of the mush [118, 119]. Al-Jarba and Fuchs [118] suggested that flow blockage resulted from TiC particle may responsible for the increasing in solidification defects. Ness *et al.* [119] demonstrated that these blocking particles altered permeability and may influence the formation of freckle defect. They simulated columnar dendrite microstructure with the presence of blocky carbides, as shown in

Figure 2.15a, and used this obtained microstructure to calculate permeability at various locations of different solid fraction. They found that carbide particles significantly impacted permeability near the dendrite tips but only slightly influenced permeability at deeper locations in the mush (i.e. higher fraction solid).

As can be clearly seen in Figure 2.15b, the formation of plate-like β-Al_5FeSi intermetallics in Al-Si alloys could also block the interdendritic channels. Many authors have suggested that this could leads to the restriction of interdendritic fluid flow and thus reduction of permeability in the mush [8, 120]. However, the quantified impact of β-intermetallic on permeability of solidifying microstructure has never been made.

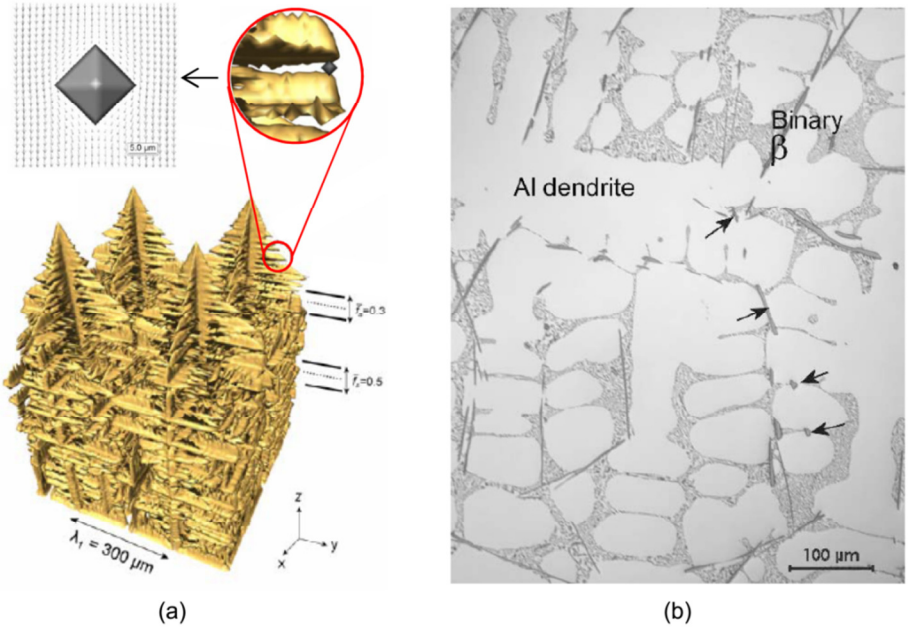


Figure 2.15 (a) Flow simulation of columnar dendrites with blocking carbides in Ni-based superalloys, after [119], and (b) quenched Al-Si microstructure showing β-intermetallics in the interdendritic regions, from [47].

2.4 Solidification defects

In addition to the negative effects on the mechanical properties of the final product, β-Al_5FeSi intermetallics are also reported to be deleterious to castability and can increase alloy propensity for the formation of other solidification defects,

particularly porosity and hot tearing. This section reviews briefly mechanisms involved the formation of these defects, as well as reports prior studies in which investigated the effect of β-intermetallics on defect formation.

2.4.1 Porosity

One of the most important defects in aluminium casting components is porosity. The presence of macroporosity and/or microporosity in the microstructure can limit elongation and fatigue properties of casting components [121-123].

2.4.1.1 Formation of porosity

There are two primary causes for the formation of porosity in the castings: volumetric shrinkage and supersaturation of the dissolved gases. As solidification takes place, the volume of the material decreases (as solids are denser than liquids) and the surrounding liquid flows in to compensate for that decrease in the volume of the material. However, if this feeding occurs through an area that is partially or completely solidified, the flow can be so restricted that the pressure is reduced locally. This leads to the forming of many small pores called micro-shrinkage porosity. Differences in hydrogen solubility in solid and liquid can also cause porosity. In aluminium, hydrogen is the only element which has a measurable solubility in liquid (~0.69ml/100g$_{STP}$) [124]. However, once the liquid is transformed into solid, the solubility of hydrogen is decreased dramatically to ~0.036ml/100g$_{STP}$ [124]. This leads to the supersaturation of hydrogen at the solid-liquid interface that can promote the nucleation of the pores if the local chemical potential becomes significant enough to overcome the nucleation barrier [125]. This type of porosity is termed gas porosity. Whittenberger and Rhines [126] illustrated that driving forces from both shrinkage and gas contribute to the formation of porosity.

Jones *et al.* [127] reviewed theories of gas bubble nucleation in a supersaturated solution and concluded that four types of bubble nucleation could be classified: (I) classical homogeneous nucleation, (II) classical heterogeneous nucleation, (III) pseudo-classical nucleation and (IV) non-classical nucleation. Similar theory of nucleation for solid phases, as discussed in section 2.1.1, can be used to describe types I and II of bubble nucleation but the effect of pressure must also be introduced to bubble formation. The formation of bubbles occurs when the critical supersaturation is exceeded. In types III and IV nucleation, gas pockets exists within the liquid which reduce the degree of supersaturation required for bubble formation. Athermal nucleation mechanism, as discussed in section 2.1.1.2, could also be valid where the gaseous phase is active for pore nucleation. The difference in types III and IV is that the curvature of the gas pocket surface is less than the critical curvature for growth in type III but larger than the critical curvature in type IV. Fox and Campbell [128] observed that some air and oxide bi-films could be entrained in the melt during pouring which could then promote types III and IV bubble formation. Lee and co-workers [23, 129, 130] used an x-ray temperature gradient stage (XTGS) to observe *in situ* porosity formation in Al-Cu and Al-Si alloys. They found that very small degrees of supersaturation were required, suggesting the association of type III or IV nucleation mechanism.

Once a pore forms, it will first grow freely in the melt as a spherical shape, as shown in Figure 2.16a. The analytical expression for the pressure inside a spherical pore of radius r_P is given by:

$$P_G = P_L + \frac{2\gamma_{LG}}{r_P} \tag{2.29}$$

where P_G and P_L are pressure inside pore and liquid, respectively, and γ_{LG} is interfacial energy of liquid-gas. The growth of the pore is subsequently constrained by developing

dendrites, making the curvature of the pore depend upon solid geometry (as shown in Figure 2.16b). The internal pressure of pore in Equation (2.29) becomes:

$$P_G = P_L + \frac{2\gamma_{LG}}{(r_1 + r_2)} \tag{2.30}$$

where r_1 and r_2 are principal radii of curvature for non-spherical interface. During the growth, the pore can grow through an interdendritic area where radii of curvature increase, as shown at point A in Figure 2.16b. However, radii may also decrease, such as when the pore grow into point B in Figure 2.16b, resulting in an increasing in pore pressure. The pore finally becomes less round and has a complex interconnected morphology.

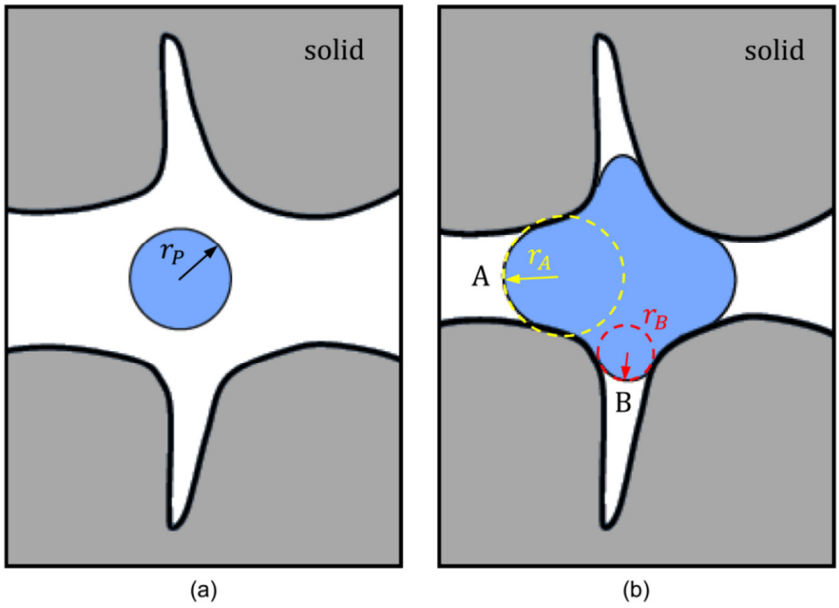


Figure 2.16 Schematic of pore growth between dendrites at solidification time: (a) t_1 and (b) $t_2 > t_1$.

2.4.1.2 Effect of intermetallic on porosity

Fe-rich intermetallics are reported to be deleterious to castability and can increase alloy propensity for formation of solidification defects, such as an increase in porosity content [8, 47, 78, 131]. It has been suggested that this might be due to the intermetallic phase: acting as pore nucleation sites [132], causing flow blockage in the

interdendritic channels [120], inducing the development of bigger Al-Si eutectic grains that may degrade feeding [133], and/or aiding pore growth [11].

Roy *et al.* [132] carried out an extensive porosity study in Al-9Si-3Cu (wt.%) alloys using statistical analysis based on metallography of 72 wedge castings. They observed that Fe forms many types of Fe-rich intermetallics, including β-Al_5FeSi, α-$Al_{15}(Mn,Fe)_3Si_2$ and π-$Al_8Mg_3FeSi_6$, depending on alloy composition. Pores were found along planar surfaces of β-intermetallic particles in most fully-solidified micrographs, as shown in Figure 2.17a. They hypothesised based on this observation that β-intermetallics acted as effective pore nucleation sites. Furthermore, they found that β-intermetallics can play a role in restricting the growth of both gas and shrinkage pores, as shown in Figure 2.17b.

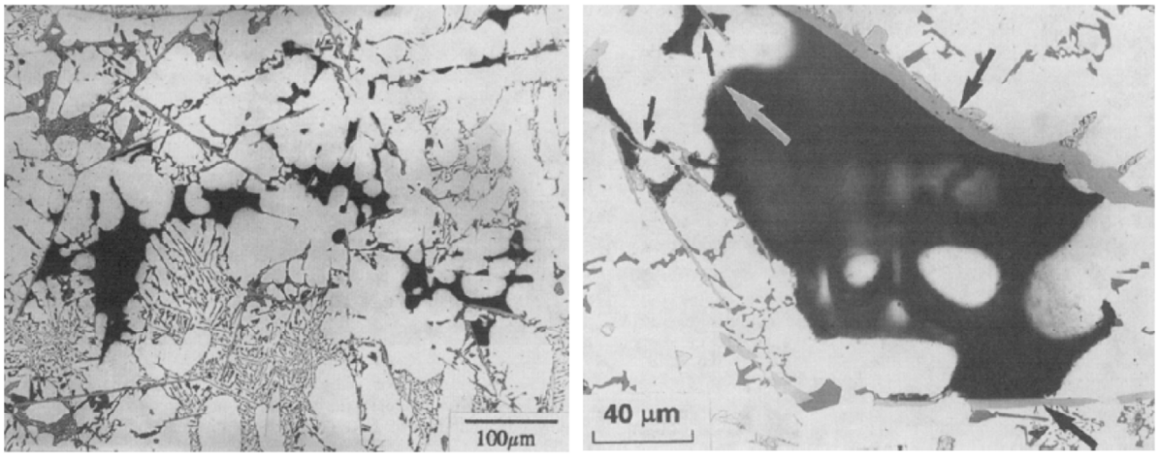


Figure 2.17 Solidified microstructures of Al-9Si-3Cu-1Fe (wt.%) showing (a) pore nucleation along β-intermetallic and (b) restriction of pore growth by β-intermetallic (indicated by arrows), from [132].

Dash and Makhlouf [120] studied the effect of alloying elements on feeding characteristics of Al-Si alloys and concluded that Fe (and Si) alone do not influence porosity formation. It is instead the formation of Fe-bearing intermetallic phases, e,g. β-Al_5FeSi and α-$Al_{15}(Mn,Fe)_3Si_2$, that leads to a poor feeding characteristic of liquid metal. Differences in size and morphology of intermetallics make different contribution

to feeding, and thus porosity. They found that needle-like β-Al_5FeSi intermetallics heavily blocks interdendritic paths and thus hinders liquid flow in these regions. Shorter plate-like β-intermetallics, resulting from lower Fe levels, and compact script-like α-intermetallic, resulting from Mn addition, were found to improve interdendritic feeding. This observation agreed well with previous studies [69, 134, 135], which reported that increases in Fe content leads to a poorer feeding and hence promotes shrinkage porosity.

Otte *et al.* also reported similar results that increasing Fe content increases shrinkage porosity [136]. They suggested that this may associate with the change in solidification sequence at different levels of Fe. This observation is in contrast to the studies from Taylor *et al.* [131, 137] whom proposed that the relationship between Fe-content and porosity is non-monotonic. Porosity formation was found to be minimised at a critical Fe content since the solidification proceeds directly via ternary eutectic reaction. They also observed that critical Fe content is a function of Si level of the alloy. Dinnis *et al.* [8] further suggested that the non-monotonic relationship Fe-porosity is dependent on both Si and Cu concentration.

Dinnis *et al.* [133] later proposed that size of β-Al_5FeSi intermetallic together with Al-Si eutectic grain size determine porosity level. They found that AlP particles are effective nuclei for both β-intermetallic and Al-Si eutectic. The formation of β-intermetallics prior to Al-Si eutectic decreases available AlP nuclei and thus limits number of eutectic nucleation events. This leads to the development of less but bigger Al-Si eutectic grains. These large grains as well as β-intermetallic can physically block the feed path, hence reducing permeability.

Recently, Wang *et al.* [36] used x-ray synchrotron radiography to capture real-time formation of β-Al_5FeSi intermetallic and pore in an Al-7.5Si-3.5Cu-0.8Fe (wt.%) alloy. In this 2-D *in situ* observation, pores were observed to form near or around β-

intermetallics, as shown in Figure 2.18a, providing evidence that β-intermetallics influence porosity formation. They hypothesised later [11], based on this 2-D result, that the presence of β-intermetallic reduces liquid-gas interfacial energy, both lowering nucleation barrier and aiding pore growth. They also suggested that β-intermetallic may block hydrogen diffusion path and increase hydrogen supersaturation within each subdomain, promoting nucleation of pores.

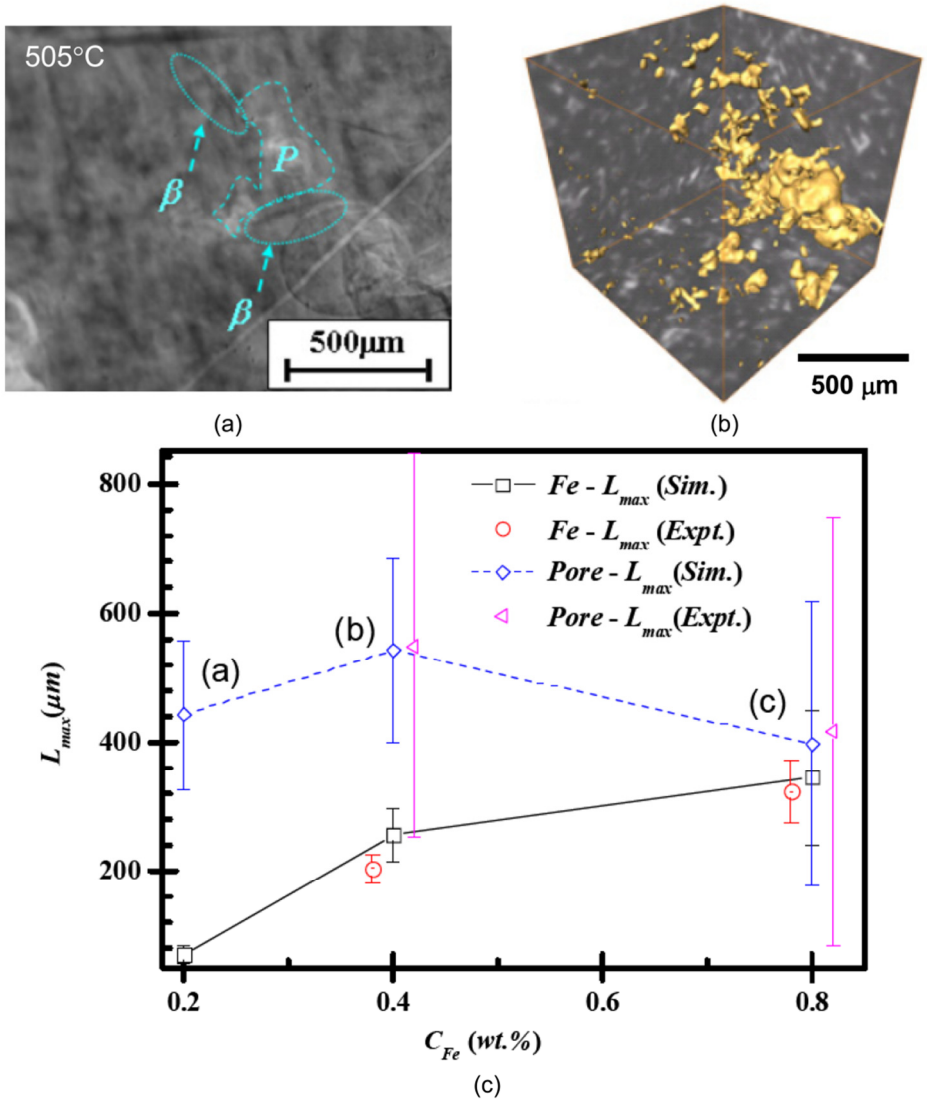


Figure 2.18 (a) radiograph showing β-intermetallics (β) and pores (P) during *in situ* solidification of Al-7.5Si-3.5Cu-0.8Fe (wt.%) (from [36]); (b) 3-D rendering of porosity in fully solidified microstructure of Al-7.5Si-3.5Cu-0.4Fe (wt.%) (from [138]); and (c) influence of Fe content on maximum size of β-intermetallics and pores (from [11]).

These assumptions were implemented into their multi-scale model [11] to predict the interaction between β-intermetallics and porosity formation. This model was validated using x-ray tomography results of fully solidified microstructures, as shown in Figure 2.18b. As can be seen in Figure 2.18c, good quantitative agreement was found when predicting pore formation in Al-7.5Si-3.5Cu (wt.%) alloys at two different Fe levels (0.4 and 0.8). This indicates that the hypothesised mechanism of reduced liquid-gas interfacial energy may have a significant contribution.

Discrepancies amongst prior studies highlight the question of how exactly β-intermetallic particulates affect porosity formation during solidification.

2.4.2 Hot tearing

Hot tearing is a term applied to the formation of macroscopic defect, usually in the greatest thermal strained region, when an alloy is still in the semi-solid or 'mushy' state. Hot tears, also known as hot cracking, are generally large (visible to naked eyes) and appear as cracks, either on surface or inside the casting. The formation of hot tears usually results in part rejection during production.

2.4.2.1 Formation of hot tearing

The formation of hot tears is a complex phenomenon caused by insufficient liquid feeding compensating for solidification shrinkage in the presence of thermal strains and stresses [139]. It has been shown that hot tears are localised at grain boundaries and can nucleate on pores, oxides and liquid films [139-141]. As reviewed by Eskin *et al.* [142], a number of experiments and numerical models have been investigated to understand the processing parameters and criteria that play a role in making alloys and castings less susceptible to hot tearing. Many theories were proposed that considering hot tearing to be introduced by stress [143], strain [144], and strain rate [145]. Sistaninia *et al.* [146] recently suggested that the feeding condition of the

mushy zone controls hot tearing. Strain accumulation is a critical factor when feeding is insufficient, while strain rate plays a bigger role if the mushy zone is well fed. It is also believed that an alloy with a larger freezing range is more prone to hot tearing since the alloy must experience the vulnerable stage for a longer time [147]. Grain size and morphology were also found to have an effect on hot tearing. It was suggested that a small globular/equiaxed structure postpones the dendrite coherency point, as compared to a large dendritic structure, resulting in a lower tendency to form hot tears [148, 149]. However, most of these studies only observed the influence of processing parameters postmortem, i.e. after the failure.

Input from the direct observation of microstructural evolution during semi-solid deformation (e.g. [92, 150-154]) provides distinctive insights into semi-solid deformation response and defect formation mechanisms. Various techniques have been used to achieve *in situ* observation of hot tearing. Pellini [144] used x-ray radiography and simultaneous temperature measurement to observe hot tearing in an Al–Cu alloy. He proposed based on this first observation that hot tearing is a strain-controlled mechanism. Although the experiment was carried out *in situ*, the observation was taken only at 30s to 60s intervals. Davidson *et al.* [155] and Mitchell *et al.* [156] performed *in situ* observations via a high-resolution video recording device on an Al-Cu alloy. It was found that hot tearing started at a very low load and the locations that hot tears occurred seemed to be consistent with the strain localised regions. Even though hot tear formation was observed in real-time, it was limited to the specimen surface. Farup *et al.* [140], who used succinonitrile-acetone as an analogue of a binary metallic alloy, identified that hot tearing always occurred at grain boundaries. Although the solidification conditions of a metal were successfully mimicked in this transparent alloy, the mechanical behavior was, however, not identical.

Phillion *et al.* [92] used high speed x-ray radiography to directly observe semi-solid Al-12wt.%Cu subjected to tensile testing over a range of temperatures. A capture rate of 1.25 Hz and a spatial resolution of 3 μm were used, with load and displacement being measured during image capture. As shown in Figure 2.19, the key microstructure features of strain localisation (marker A), flow of liquid, damage nucleation and growth (marker B-C), and final failure (marker D) were successfully resolved. The study, however, was done in 2-D, thus the observation of the complexity of connected pores and interdendritic liquid was limited.

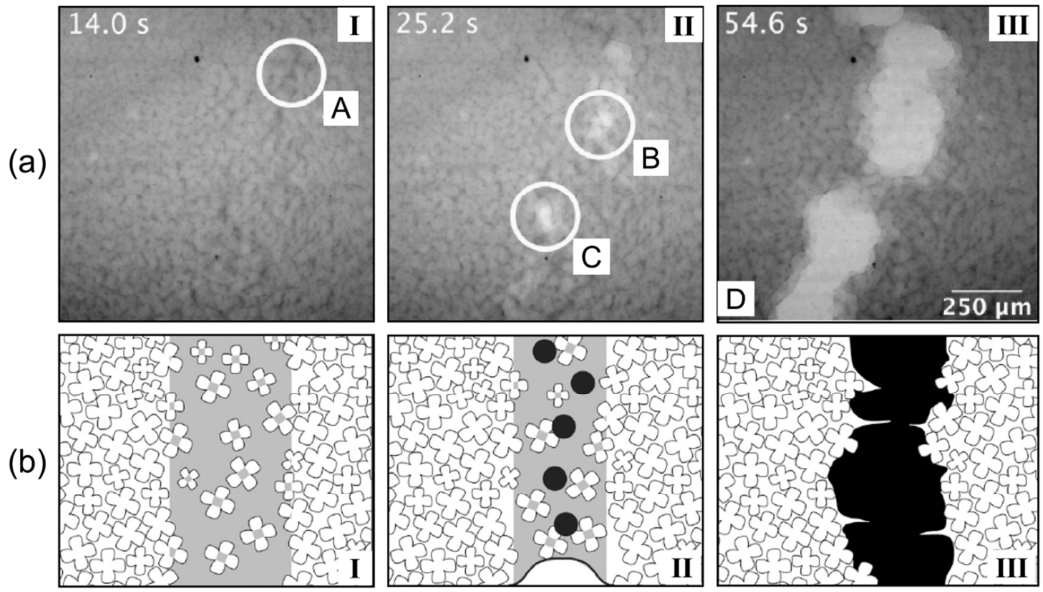


Figure 2.19 Evolution of hot tearing: (a) sequence of x-ray radiographs obtained during isothermal horizontal tensile loading of Al-12Cu (wt.%) at 580 °C (f_S~0.62) and (b) schematic. Strain localisation and fluid flow towards this region, nucleation and growth of damage, and final fracture are shown in inset I-III (of both a and b), respectively, after [92].

Terzi *et al.* [157] used *in situ* x-ray microtomography to image 3-D inhomogeneous deformation of a semi-solid Al-8wt.% Cu alloy under tensile conditions. Each 3-D volume of data was obtained every 27s with a spatial resolution of 2.8 μm. Accumulation of liquid and void formation were successfully observed in 3-D, as shown in Figure 2.20, but only qualitative characterisations were made regarding void formation and its relationship with final specimen failure. Moreover, the

microstructure only contained a few coarse grains across the specimen's diameter hence the continuum of hot tearing behavior might not be represented.

This *in situ* result was recently further analysed [151, 158] and used to validate a 3-D coupled hydromechanical FE/DEM model [146, 158]. The model predicted that strain localises along few preferential paths within the liquid channels in the direction perpendicular to tension. Furthermore, hot tears were predicted to form in the widest liquid channels at the free oxidised surface, i.e. initiate in contact with ambient air. Although this prediction of surface-connected hot tears agrees with the *in situ* observation of Terzi *et al.* [157], it cannot predict the formation of internal hot tears demonstrated by Phillion *et al.* [92]. This contradiction underlines the complexity of hot tear formation and posts an open question for further studies.

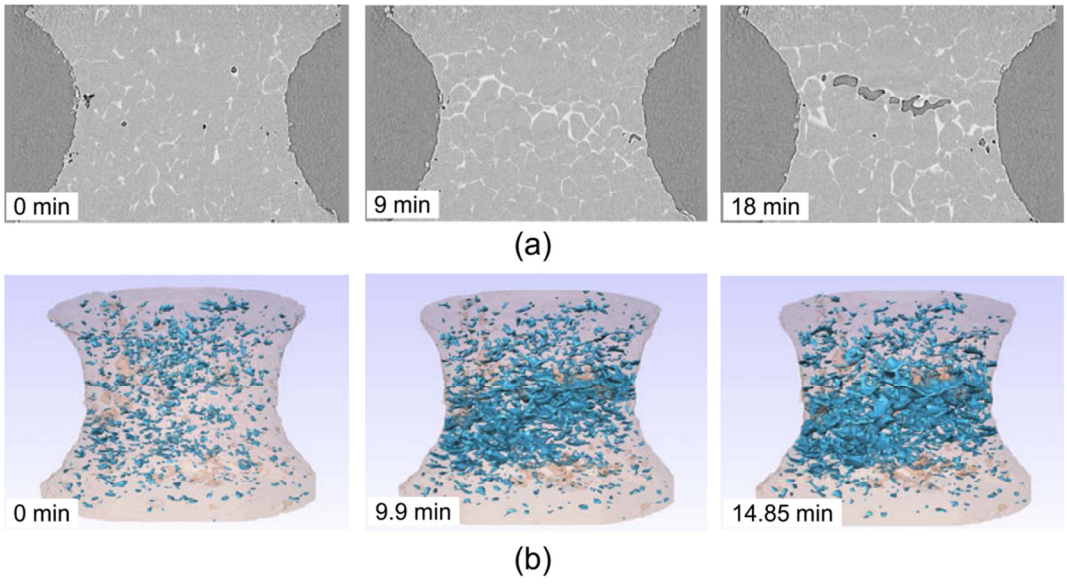


Figure 2.20 (a) 2-D longitudinal sections and (b) 3-D images of liquid accumulation in the notched area during isothermal vertical tensile loading of Al-8Cu (wt.%) at 555°C (f_S~0.93), after [157]. Note that liquid appears white in (a) and blue in (b) whereas damage (void) appears dark in (a) and not rendered in (b).

2.4.2.2 Effect of intermetallic on hot tearing

While an extensive number of experimental and numerical investigations have been made, mostly in binary alloys, to relate various alloying and processing

parameters to hot tearing susceptibility [139, 140, 142, 145], little is known about hot tearing in commercial Al-Si alloys. Sweet *el al.* [159] demonstrated a strong relationship between Fe-contents and hot tearing susceptibility in AA-6060 alloys, which may relate to differences in morphology and prevalence of Fe-rich intermetallic phases. In A319 alloys, it has been shown that the addition of Sr or TiB_2 has beneficial effect in reducing hot tearing susceptibility [7, 160]. In parallel, Sr-modifications [47] and TiB_2-grain refiner [70] have been determined to greatly alter the size and morphology of plate-like intermetallic phases. Therefore, while the role of β-intermetallics on hot tear formation has not been directly examined, the correlation between the morphology modification of intermetallics due to composition additions and the reduction in the hot tear response points to a direct influence of intermetallics on hot tear formation via underlying mechanisms which are still unclear.

Chapter 3

Formation of β-intermetallics*

As seen in Chapter 2, understanding the nucleation and growth of secondary phases has been a long-standing subject of research for metallurgists. In Al-Si alloys, secondary phase formation provides one of the most widely used strengthening mechanisms through age hardening, but also limits the use of recycling in many engineering applications especially where the fatigue life is critical [6]. As reviewed in section 2.2, the enhancement of Fe levels during aluminium recycling is sufficient to promote the formation of highly faceted plate-like β-Al_5FeSi intermetallics during solidification. These plate-like intermetallics are usually hard and brittle, have a low cohesion with the aluminium matrix [79], and thus may degrade the mechanical properties of cast components [74].

Although it would appear from prior experimental studies [47, 55, 85] that the final size and morphology of β-intermetallics can be refined through alloying elements and optimised solidification conditions detailed in section 2.2.4, knowledge of nucleation mechanisms and growth kinetics of β-intermetallics remains limited. This knowledge is

* Note, this chapter has been submitted in modified form to Acta Materialia as the paper entitled "In situ synchrotron quantification of the nucleation and growth of Fe-rich intermetallics during Al alloy solidification" by Puncreobutr, C., Fife, J.L., Phillion, A.B., Rockett, P., Horsfield, A., Lee, P.D.

needed to control the nucleation process and to improve casting quality. As discussed in sections 2.2.2 and 2.2.3, the formation of β-intermetallics in Al-Si is very complicated and may involve various reactions and mechanisms. In order to reveal the complexity of β-intermetallic nucleation and growth, recent work [36, 63] has focused on the use of *in situ* methods. While an initial rapid growth in the lateral direction and a slow thickening rate of β-intermetallics were both observed in these *in situ* experiments [36, 63], its nucleation mechanisms and growth interactions remain unclear due to a lack of temporal resolution.

The aims of this chapter is to investigate the mechanisms controlling the formation of β-intermetallics during *in situ* solidification of an Al-7.5Si-3.5Cu-0.6Fe (wt.%) alloy via fast 3-D *in situ* synchrotron tomographic imaging. The chapter is divided into 5 sections. Details of the materials, the 3-D imaging and the quantitative image analysis techniques are presented in the first section. Sections 2 to 5 explore, respectively, key findings relating to the solidification sequence, nucleation mechanisms, growth kinetics, and intermetallic-intermetallic interactions of the β-Al_5FeSi intermetallic phase.

3.1 Methods

3.1.1 Specimen preparation

An aluminium A319 alloy with a nominal composition of Al-7.5Si-3.5Cu-0.6Fe (wt.%) was prepared using a commercial Al-A319 ingot (as-received from Ford Motor Company, USA) and a commercially pure Al-10Fe (wt.%) master alloy (London & Scandinavian Co Ltd., UK). To prepare this alloy, a clay-bonded graphite crucible and a well-fed steel permanent mould [161] were first coated with Dycote® (Foseco, UK) and preheated in a furnace at 200°C for 4 hours to remove moisture. The metals were then

melted at approximately 730˚C in the preheated graphite crucible within an electric-resistance furnace. Before the casting, degassing was done by injecting Ar gas into the bottom of the crucible for approximately 2 minutes. The degassed melt, without the addition of grain refiner and eutectic modifier, was then cast into the preheated permanent mould [161] to form a wedge-shaped specimen. The casting process and dimensions of the wedge-shaped specimen are shown in Figure 3.1. Two cylindrical specimens of 2.5 mm in diameter and 4 mm in length were subsequently cut from the casting wedge using wire-electric-discharge machining for use in the *in situ* solidification studies. The actual chemical composition obtained using wavelength dispersive x-ray fluorescence (Phillips PW 1480 spectrometer) is given in Table 3.1. Note that the precision of the measurement for major elements obtained from used spectrometer is generally better than ± 0.1wt.%.

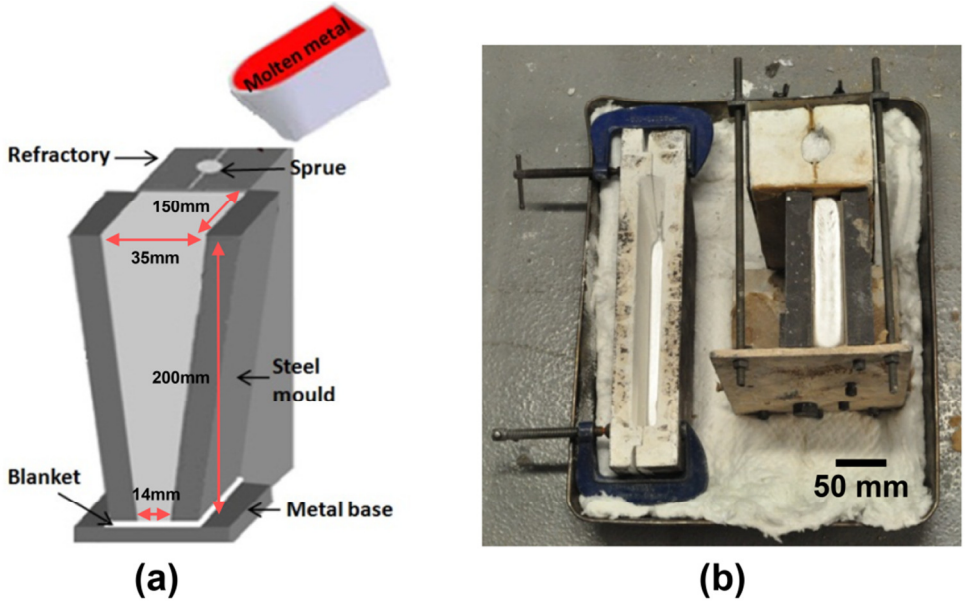


Figure 3.1 (a) Schematic and (b) photograph of wedge mould casting.

Table 3.1 Chemical composition of A319 alloy with 0.6Fe (wt.%)

A319	Al	Si	Cu	Fe	Mn	Mg	Ti	Zn
0.6Fe	balance	7.52	3.53	0.59	<0.01	0.07	0.07	0.01

3.1.2 *In situ* solidification experiments

The *in situ* solidification experiments were performed on the TOMCAT beamline at the Swiss Light Source (Paul Scherrer Institut, Switzerland) [162] using a bespoke resistance furnace with six enclosed alumina heaters. The furnace was designed to have a hole from top to bottom through which the specimens and thermocouples could be inserted, and two windows on opposite sides to allow the x-ray beam through. The specimens were contained in a high-purity boron-nitride (BN) holder that was fitted on top of a pyrophyllite rod on the rotation stage, as shown schematically in Figure 3.2a. A K-type thermocouple was placed underneath the specimen holder to measure temperature during the experiments. The experimental setup, mounted within the hutch of the TOMCAT beamline at the SLS, is shown in Figure 3.2b. Note that an adjustable holding arm affixed to the TOMCAT base stage was designed to independently hold the *in situ* furnace over the specimen holder, as shown in Figure 3.2c.

The experimental procedure consisted of first gradually heating the specimen up to 650°C, holding it for 5 minutes to ensure complete melting, and subsequently cooling it at a controlled rate of 0.05°C/s until fully solid. During solidification, fast x-ray tomography was conducted, collecting 1001 projections over 180° of rotation every 2s [163]. Polychromatic radiation filtered to 5% power (an approximate average peak energy of 30keV) was used in combination with a high-speed pco.DIMAX CMOS camera, which acquires individual projections orders of magnitude faster than traditional CCD cameras. The detector incorporated an optical microscope designed for high numerical apertures and polychromatic radiation. It was tuned close to 4x magnification, resulting in a pixel size of 2.75 μm. The field of view was large enough to capture the entire cross-section of the specimen. This fast tomography ensured that

microstructural evolution within a 3-D volume was small as the temperature change within 2s for capturing a 3-D volume was ~0.1°C.

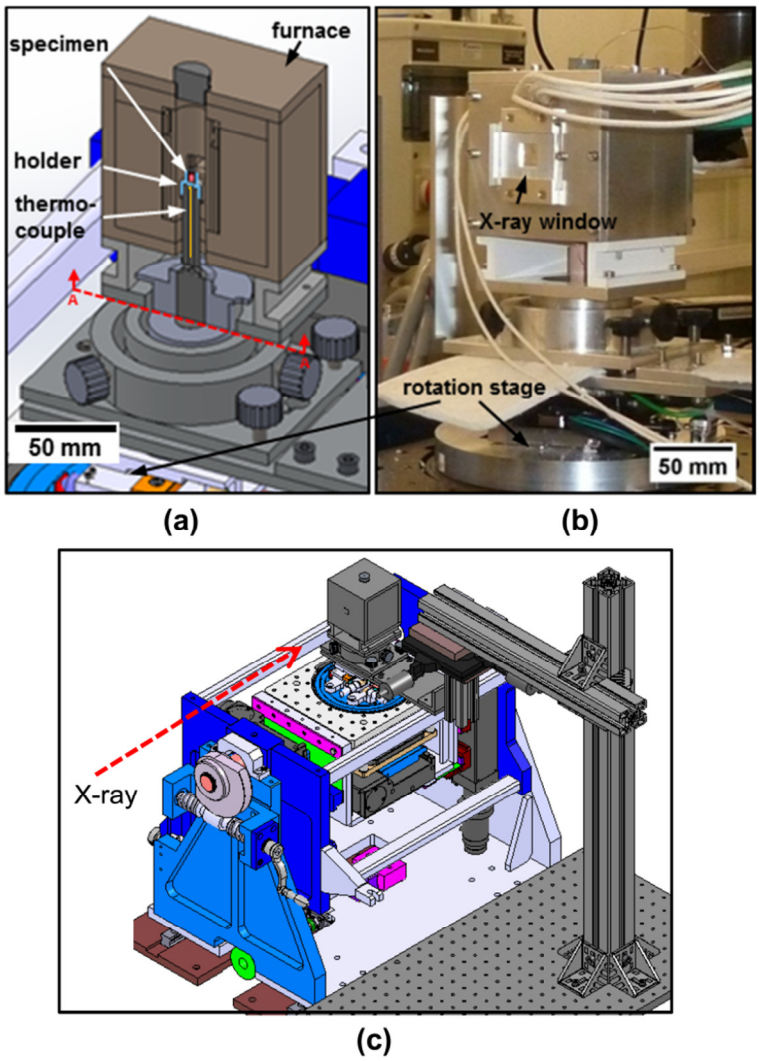


Figure 3.2 (a) Cross-sectional schematic of the experimental setup, (b) photograph of the furnace mounted on the TOMCAT beamline of the SLS and (c) schematic of the holding arm affixed to the TOMCAT base stage.

Two *in situ* experiments with the same solidification conditions were completed. While the imaging conditions for each experiment were identical, the time between acquisitions of subsequent 3-D volumes, referred to as downtime, was 70s in the first experiment and 10s in the second experiment. The total capture interval between scans (where the total time includes acquiring one full 3-D volume and preparing for the next scan) was thus 72s and 12s in the first and second experiments, respectively. In the first experiment, the downtime of 70s was used to transfer captured data out of the

camera's buffered memory to the data repository server. As the buffered memory on the camera was cleared after every imaging sequence, observation of the entire solidification sequence was possible. In contrast, with the shorter downtime of 10s, the tomographic datasets were stored in the camera's memory buffer and only transferred out at the end of the experiment. While the short downtime allowed for greater temporal resolution and thus quantification of the rapid initial growth of the β-intermetallic particles, only thirteen 3-D volumes could be stored until the camera buffer was filled. It is worth noting that the beginning of fast tomographic imaging in the second experiment was based on observations in the first experiment, ensuring that the rapid initial growth stage of β-intermetallics was captured.

3.1.3 Tomographic reconstruction

The procedure of tomographic acquisition and reconstruction is summarised in Figure 3.3. As discussed above, the application of fast x-ray tomography (Figure 3.3, inset I) during *in situ* experiments generates a series of two-dimensional x-ray projections (radiographs) taken at different illumination angles θ. This full set of acquired data (Figure 3.3, inset II) is used as an input to digitally reconstruct the 3-D structure of the specimen. First, the projections are transformed into a set of sinograms (Figure 3.3, inset III), which allows efficient reconstruction artifact removal. A sinogram represents a plot of absorption intensity as a function of rotation angles θ, which is obtained by taking the same row x from each projection (yellow lines in Figure 3.3, inset II) and stacking them (Figure 3.3, inset III). Applying a reconstruction algorithm on one sinogram results in a single reconstructed slice of the 3-D structure (Figure 3.3, inset IV). By performing an identical procedure on the entire set of sinograms, a full reconstructed 3-D volume of the specimen is obtained (Figure 3.3, inset V). There are many algorithms available for tomography reconstruction, with the

Fourier transform method (FTM) and the filtered back projection method (FBP) being widely used due to their high accuracy and amenability for fast implementation [164].

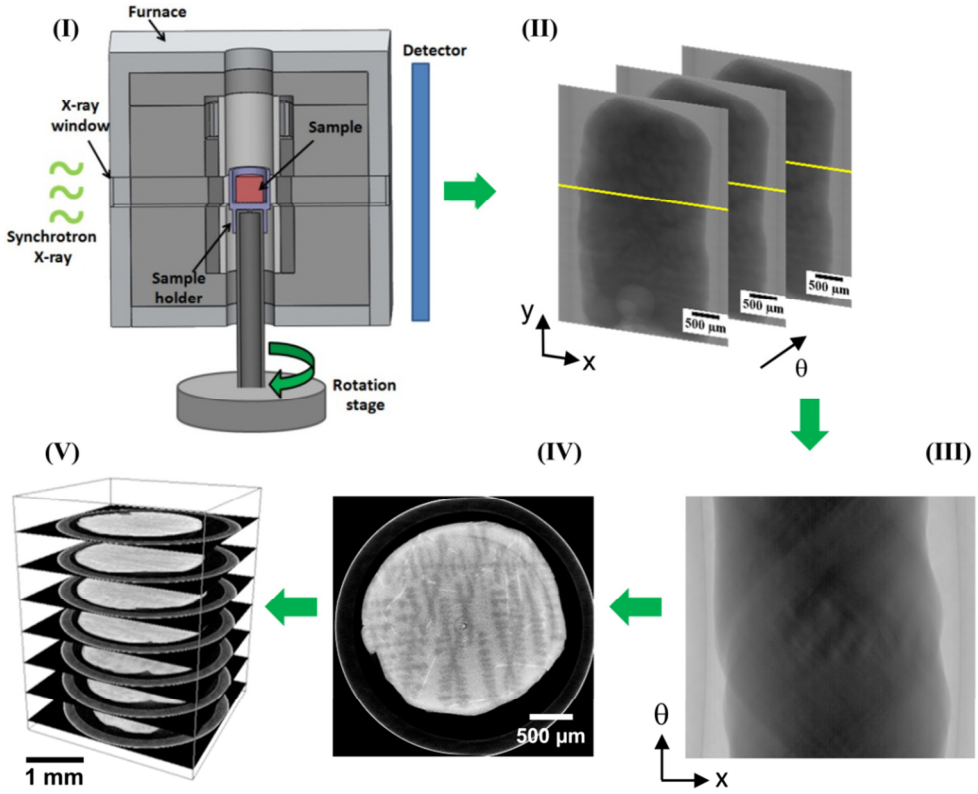


Figure 3.3 X-ray tomographic acquisition and reconstruction.

At the TOMCAT beamline, the tomographic images were reconstructed using a fast reconstruction algorithm known as gridrec based on FTM [165, 166] to obtain time-resolved 3-D volumes. This reconstruction process was done together with the application of flat-field correction, dark-field correction and ring artifact removal algorithms [167] in order to improve the quality of the 3-D volumes. The resulting 3-D reconstructed volume consists of 1104x1104x1468 voxels at a voxel size of 2.75 µm per edge, providing a field-of-view sufficient to capture the entire cross-section of the specimen.

3.1.4 Image processing and segmentation

Registration

After reconstruction, all time-resolved 3-D volumes were aligned using a 3-D affine registration method [168]. This process was performed using the Avizo software (VSG, France) with a hierarchical approach, starting from coarse resampling to finer resolutions. The normalised mutual information method [169] was used to measure the similarity between two 3-D images. A registered slice is shown in Figure 3.4a.

Masking

In order to mask out the background and isolate the specimen, a 3-D convolution method [170] was used to enhance the contrast at the specimen/background interfaces. Based on this contrast in intensity levels, a mask was created as shown in Figure 3.4b. In those cases where large pores with similar intensity values as the background exist at the specimen surface, a 3-D convex hull [170] was performed to estimate the specimen surface in that local region. Applying the mask to the original reconstructed volume isolates the specimen from the background and permits further analysis.

Noise reduction

A 3-D anisotropic diffusion filter [171] was performed to reduce noise and improve quality of tomographic images. The result is shown in Figure 3.4c, which can be compared to the original image in Figure 3.4a.

Segmentation

After noise filtering, image segmentation was used to distinguish the different phases of the microstructure. A 3-D region growing algorithm [172] was applied to the filtered volume to separate primary α-Al, Al-Si eutectic (if present) and pores from the solidifying liquid. Manual segmentation based on intensity difference was used to select the β-intermetallics. An example of the segmented phases is shown in Figure 3.4d.

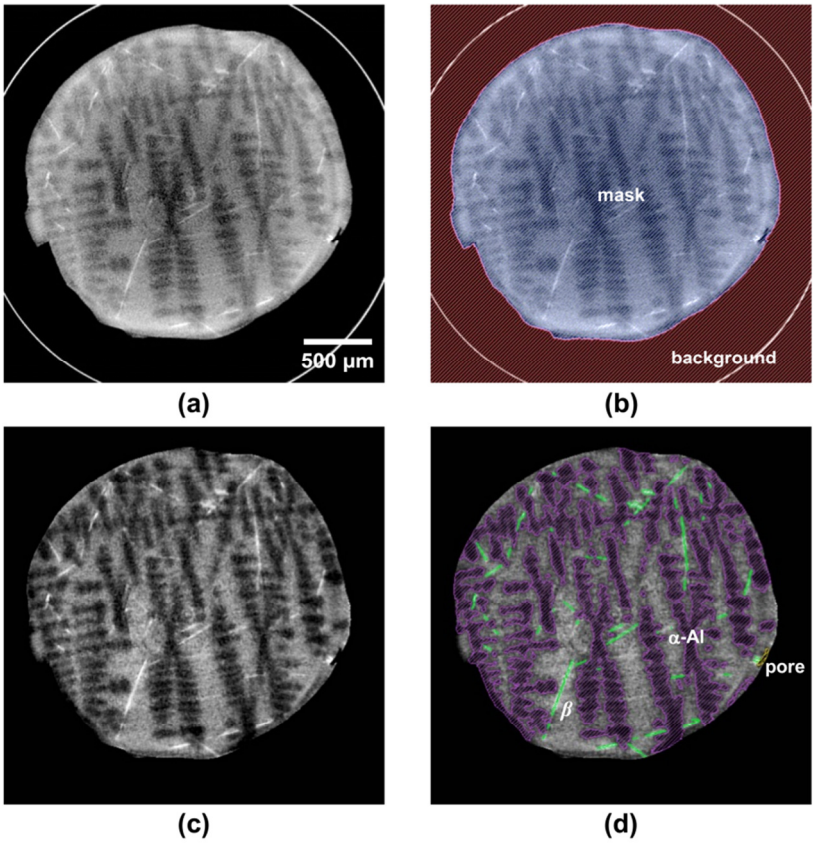


Figure 3.4 Image processing steps: (a) slice of the original reconstructed data, (b) masking of the specimen (blue) and the background (red), (c) masked and filtered slice, and (d) segmentation of the α-Al dendrites (purple), *β*-intermetallics (green) and pores (yellow).

3.1.5 Characterisation

After segmentation, a number of techniques were used to isolate individual *β*-intermetallics and characterise their orientation and centroid. First, all binarised *β*-intermetallics (Figure 3.5a) were individually separated and labelled based on their connected regions and orientations, as shown in Figure 3.5b. Second, a principle component analysis (PCA) [173] was performed to identify the normal direction of each separated *β*-intermetallic, as illustrated in Figure 3.5c. Third, the geometrical center (centroid) of each *β*-intermetallic was calculated [170]. If the centroid of any *β*-intermetallic was positioned in a non-intermetallic-labelled voxel (e.g. in the case of a bent intermetallic), that centroid was projected back along the normal of its

intermetallic to the closest intermetallic-labelled voxel. The final centroids of the labelled β-intermetallics in Figure 3.5c are shown in Figure 3.5d.

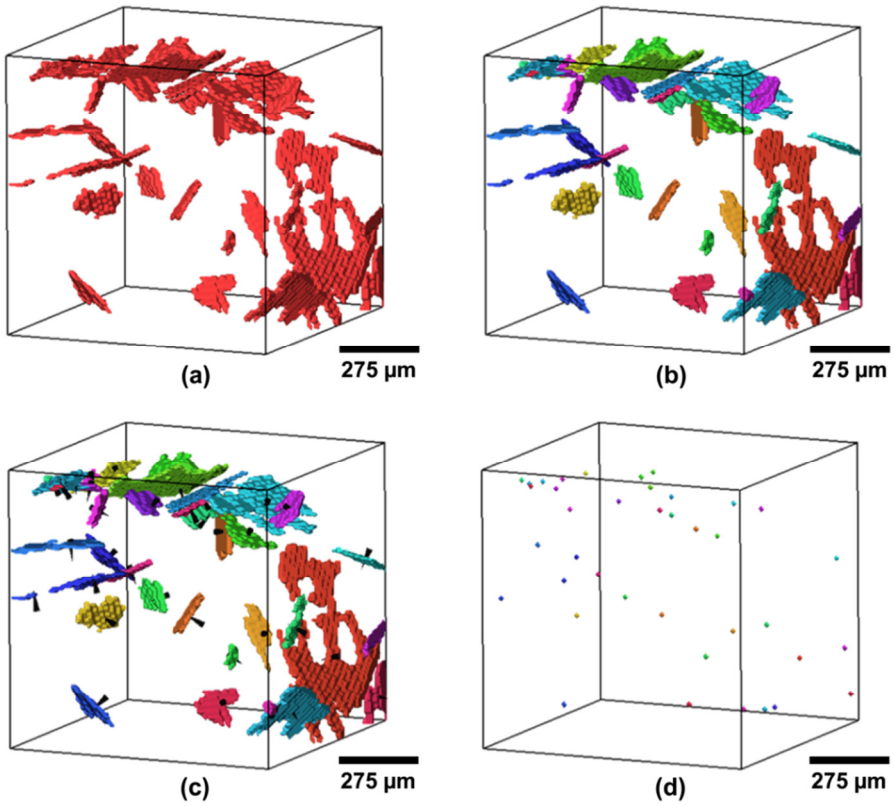


Figure 3.5 Characterisation steps: (a) segmented β-intermetallics, (b) individual β-intermetallics separated and labelled with different colours, (c) normals of labelled β-intermetallics shown as cone directions, and (d) centroid of each β-intermetallic.

Finally, a particle tracking algorithm [174] based on the centroid position and the normal vector of each intermetallic was applied to track the β-intermetallics through the time-resolved volumes.

3.1.6 Quantification

After segmenting the various phases and characterising and tracking each β-intermetallic, quantitative image analysis was performed on all the time-resolved 3-D volumes. A combination of principle component analysis (PCA), marching cube triangulation, skeletonisation and Euclidean distance transform was used to quantify orientation and growth evolution (such as volume, length, growth rate, and thickness)

of each tracked β-intermetallic [173, 175]. These 3-D measurements were performed using the Matlab software (MathWorks, USA).

Quantitative image analysis was performed on a region of interest in the first experiment to save computational time, since the change in the β-intermetallics is small during the later stages of solidification. The region of interest sub-volume was sized 400x400x400 voxels (~1 mm^3) and is shown in Figure 3.9b. In the second experiment, quantitative image analysis was performed on the full volumes because of their better temporal resolution.

The details of the 3-D quantification techniques developed in this chapter are provided below:

Volume and surface area

A marching cube triangulation technique [176] was used to calculate the polygonal surface boundary of each labelled region, i.e. each individual intermetallic, pore, etc. The enclosed volume and surface area of this isosurface were then used as an approximation for the volume and surface area of each labelled region respectively. This marching cube triangulation technique allows more correct volume and surface area estimates to be obtained compared to the more classical approach of voxel counting [177].

Intermetallic orientation and length

As mentioned in section 3.1.5, both the orientation and normal of each intermetallic plate were measured using PCA. By defining each labelled β-intermetallic as one object, PCA calculates the object's major axes from the eigenvectors of a covariance matrix based on the x–y–z coordinates of all the voxels making up that object. The first principal component was used as the object's orientation, whereas the third principal component was used as the normal of the object. For illustrative

purposes, a cone is used to show the direction of the normal of each β-intermetallic plate in Figures 3.5c and 3.6a.

The maximum length of a plate-like β-intermetallic can be better approximated using PCA when compared to a more classical approach such as the axis-aligned bounding box method [175]. In the bounding box method, the maximum length of any object is given as the diagonal length of the smallest box with sides parallel to the Cartesian coordinate system that is needed to fully contain the object. However, as shown in Figure 3.6a, this is not a true measure and often provides a significant over-estimation [175]. In PCA, the maximum length of an object is directly measured along its longest multi-dimensional major axis, as shown in Figure 3.6b. Comparing the measurement via standard bounding box diagonal (Figure 3.6a) and PCA (Figure 3.6b) shows an error of 34% for the maximum length for an example intermetallic (diagonal box length of 99.8 µm instead of a more correct PCA length of 74.6 µm).

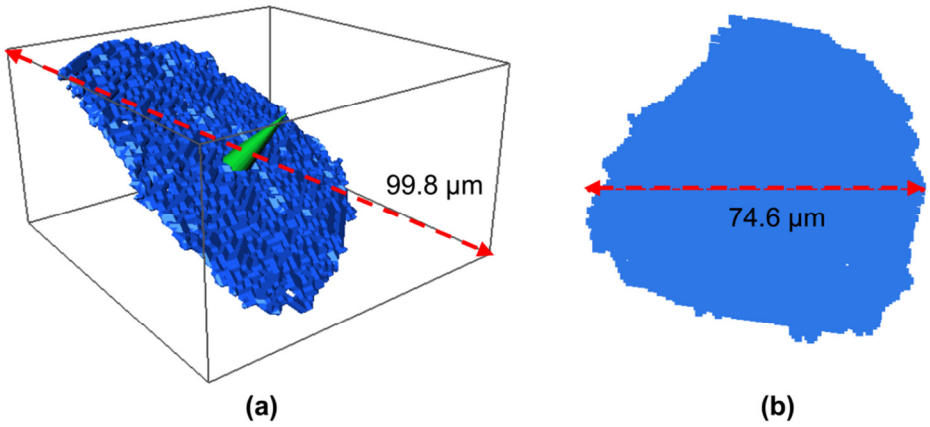


Figure 3.6 Measurement of the length of an intermetallic: (a) bounding box method and (b) PCA method.

Intermetallic thickness

In order to measure the thickness of plate-like β-intermetallics, a technique based on skeletonisation and distance transform was developed and is summarised in Figure 3.7. A random intermetallic is shown in Figure 3.7a. First, a tree-structure skeleton centrally located within the intermetallic (centerline tree) was calculated using

the algorithm described in [178]. The centerline tree for the intermetallic in Figure 3.7a is shown in Figure 3.7b. Second, the Euclidean distance [179] to the nearest surface boundary (i.e. the distance map) of each voxel inside the intermetallic was measured and is shown in Figure 3.7c. Finally, the values of the distance map along the centerline tree were doubled to obtain the local thickness of the intermetallic. The final thickness of the intermetallic was taken as the mean value of its local thickness along the centerline tree.

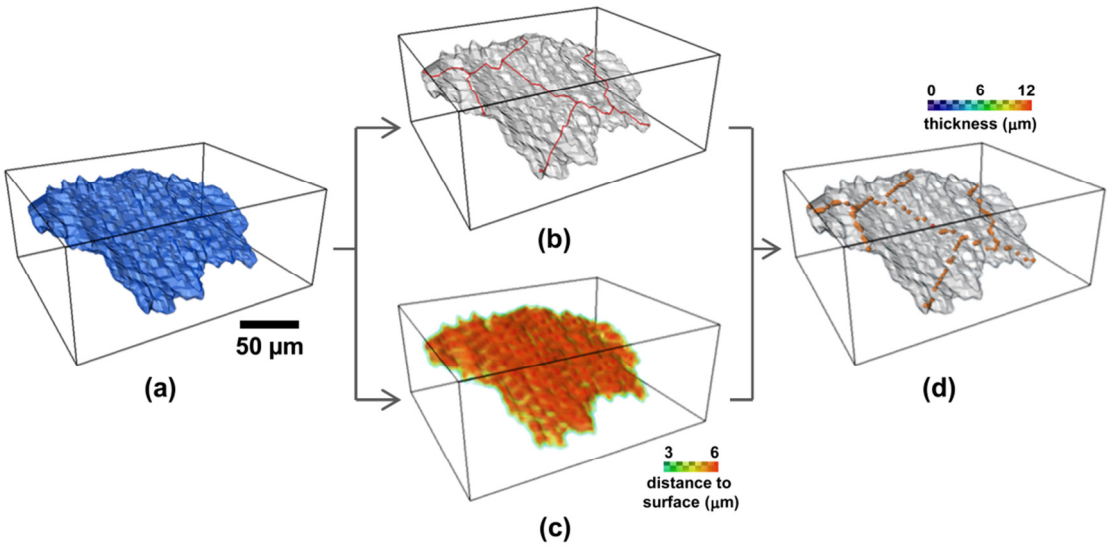


Figure 3.7 Thickness measuring steps: (a) an intermetallic, (b) centerline tree (red) calculated from (a), (c) boundary distance map calculated from (a) and (d) thickness along the center-lines calculated from (b-c).

Interface normal distribution (IND)

To characterise directionality in the primary α-Al dendrites, the probability of finding an interfacial normal in a given direction was determined [180]. This was done by first calculating interfacial normals to the object. Note that, unlike the calculation of the single normal of each β-intermetallic, interfacial normals were calculated for every triangular faces that made up the surface of the object, as shown in Figure 3.8. Next, these unit interfacial normals were stereographically projected onto a specific plane. Finally, a contour plot was created from these projected results to form an interface normal distribution (IND).

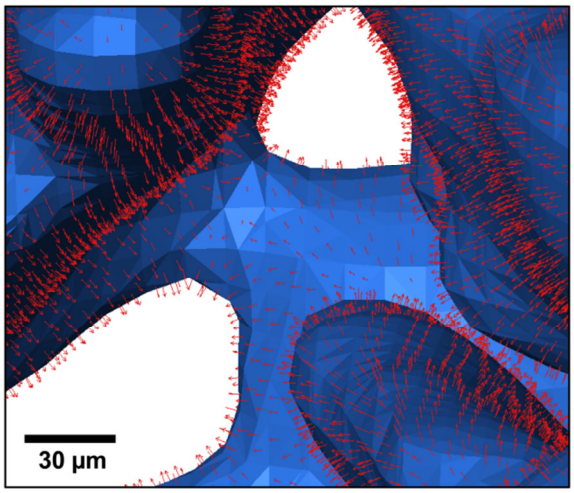


Figure 3.8 Interfacial normals (red arrows) of each triangular face.

3.1.7 Visualisation

The Avizo software (VSG, France) was used for visualisation of all the 3-D structures.

3.2 Solidification Sequence

Microstructural evolution during solidification of Al-7.5Si-3.5Cu-0.6Fe (wt.%) is illustrated in Figure 3.9. Segmented 3-D images of the various phases taken from the first experiment with a capture interval of 72s are shown in Figure 3.9 (a,c,e,g,i), while 2-D longitudinal sections are shown in Figure 3.9 (b,d,f,h,j).

The first occurrence of primary aluminium dendrites (Figure 3.9b), is observed at 600°C. They appear slightly darker than the solidifying liquid due to the attenuation contrast between the primary α-Al dendrites and the Cu-enriched interdendritic liquid. As the growth and coarsening of α-Al proceeds, the attenuation contrast increases due to the continual partitioning of Cu to the liquid. Figure 3.9c-d show the solidified structure at 582°C. As can be seen, only the α-Al phase is present in the 3-D volume. At the next capture interval, 72s later at 578°C and shown in Figure 3.9e-f, a few *β*-intermetallics have appeared in the 3-D volume as a whiter phase that is more attenuating than both the α-Al and the liquid. Further decreasing the temperature down to 572°C and shown in Figure 3.9g-h, a combination of *β*-intermetallic growth and nucleation of new *β*-intermetallics is observed. Although not shown in Figure 3.9, the formation of *β*-intermetallics is observed to be largely complete at 565°C, while the formation of the Al-Si eutectic is first observed at 561°C, around/nearby the surface of the α-Al dendrites. It is not possible, however, to resolve the Al-Si eutectic structure in 3-D due to its attenuation being very similar to the α-Al dendrites. A final amount of nucleation and growth of *β*-intermetallics, shown in Figure 3.9i-j, is detected at 550°C.

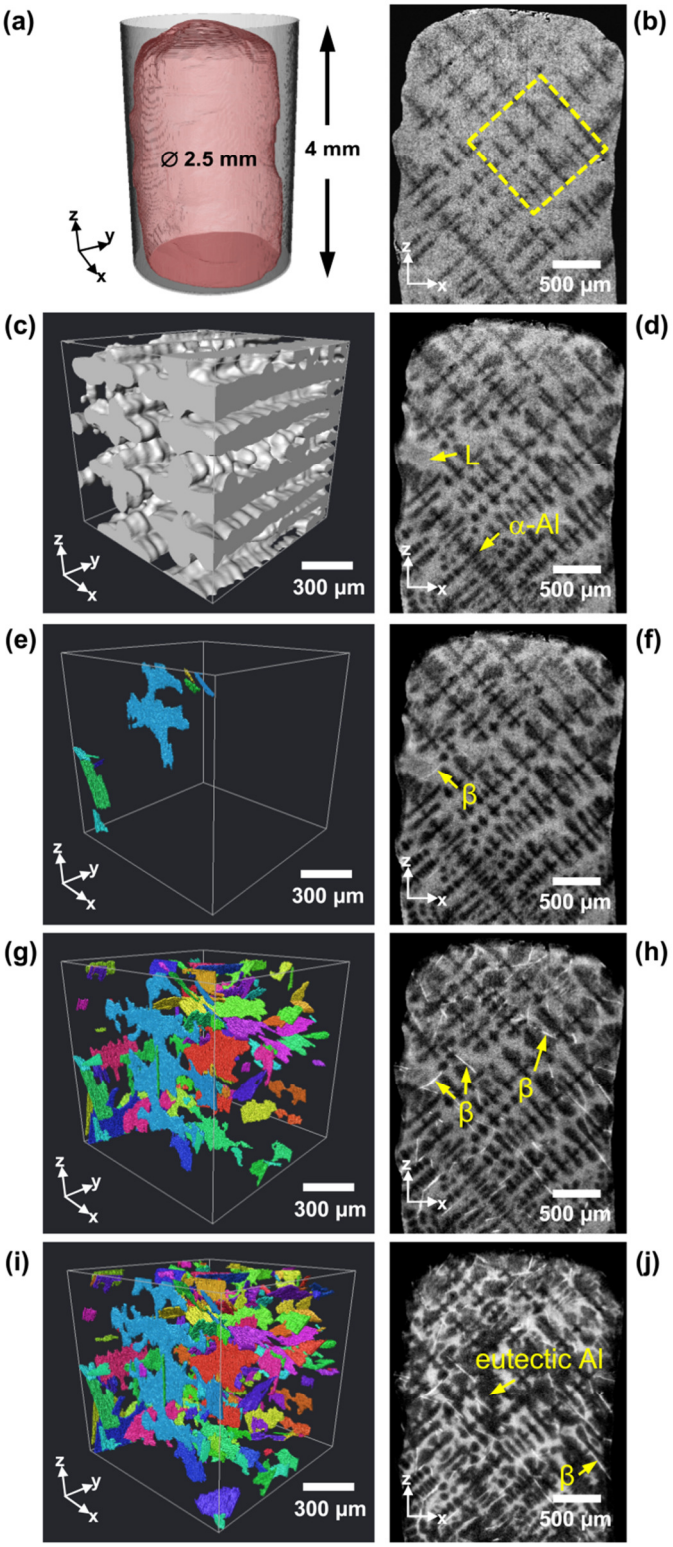


Figure 3.9 (a) Rendering of the specimen (red) inside the BN holder, (b,d,f,h,j) typical microstructure evolution during solidification of Al-7.5Si-3.5Cu-0.6Fe (wt.%), (c) 3-D rendering of the dendritic structure, and (e,g,i) 3-D rendering of the *β*-intermetallics (multi-colour is used to separate different intermetallics whereas the same colour is kept for the same intermetallics at different temperatures). The microstructures and rendering volumes represent temperatures of (b) 600°C, (c-d) 582°C, (e-f) 578°C, (g-h) 572°C and (i-j) 550°C. Note that these results were taken from the first experiment with a capture interval of 72s.

While the entire solidification sequence can be observed in the first experiment, the nucleation and growth of *β*-intermetallics in the initial stages is rendered with a greater temporal resolution in the second experiment due to the 12s capture interval,

allowing for observation of changes in the β-intermetallic structure at every ~0.5°C of cooling. The evolution of β-intermetallic formation during the initial stage is shown in Figure 3.10. The first visible β-intermetallic nucleation is at 579±1°C (Figure 3.10a). This demonstrates good agreement with the first experiment where the β-intermetallics were observed to first nucleate between the 3-D volumes acquired at 582±1°C and 578±1°C. As the temperature decreases, more nucleation events occur, providing evidence of a wide range of nucleation temperatures for β-intermetallics.

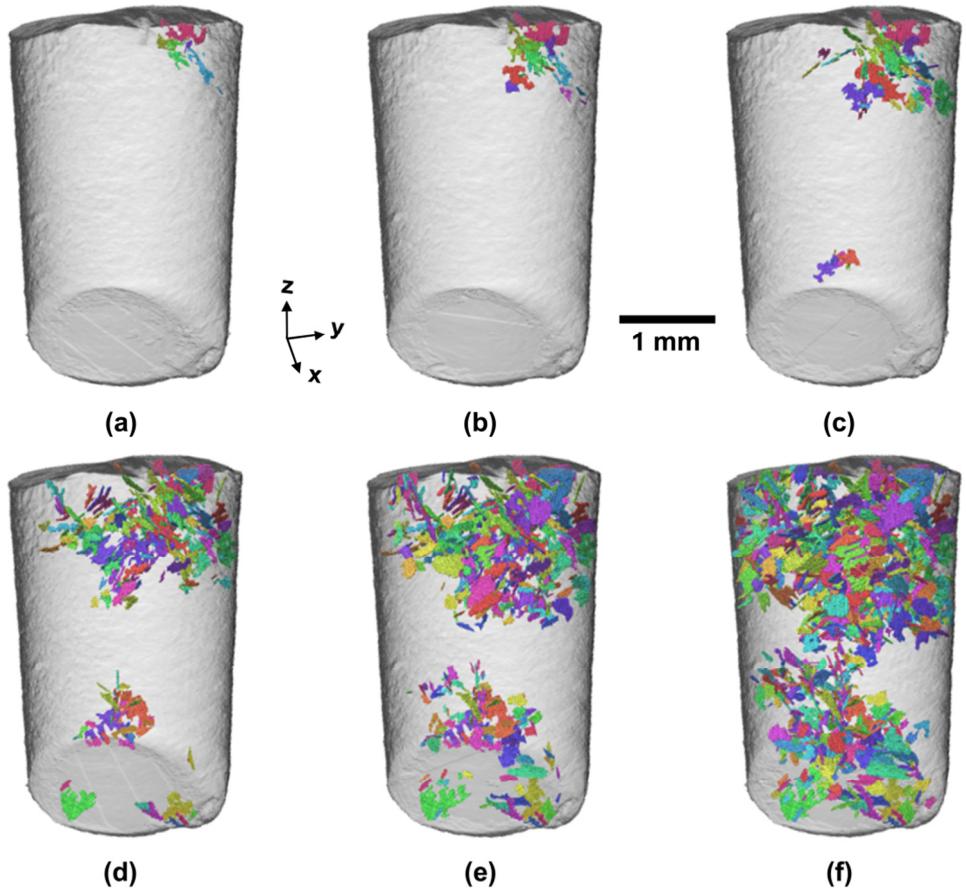


Figure 3.10 Evolution of intermetallic formation at (a-f) 579°C, 578°C, 577°C, 576°C, 575°C and 574°C, respectively. Note that these results were taken from the second experiment with a capture interval of 12s.

The evolution in the volume fraction of the β-intermetallic phase during solidification is quantified and plotted in Figure 3.11. Combining the first (72s) and the second (12s) experiments provides the complete solidification path of the β-intermetallic phase. The measured first nucleation temperature of a β-intermetallic particle is at

579°C. This initial nucleation temperature is in reasonably good agreement with previous experimental studies [63, 181], and is slightly below the value of 580°C predicted using Thermo-Calc (Thermo-Calc Software AB, Stockholm) using a Scheil solidification approximation [62]. A good agreement between the total volume fraction of the β-intermetallic phase and the predicted fraction of ~2.1% is also observed.

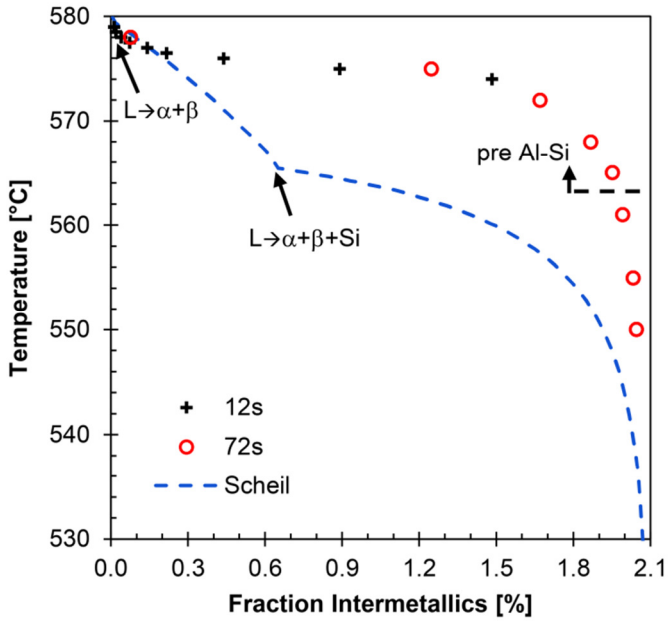


Figure 3.11 Fraction of the β-intermetallic phases as quantified from the first and second experiments, and compared to calculations from the Scheil solidification model.

The solidification path in Figure 3.11 reveals that nearly ~90% of the total volume of β-intermetallic phase forms at temperatures above the Al-Si eutectic via a eutectic reaction of L → α-Al + β-Al_5FeSi. The formation of these two eutectic components is weakly coupled, with the α-Al evolving as further growth of existing aluminium dendrites. The β-intermetallic phase appears, in most cases, to nucleate near/on the α-Al dendrites. Terzi *et al.* previously observed similar irregular eutectic growth of these two eutectic components and suggested that this eutectic reaction can occur in two different formations, coupled and uncoupled, closer to a divorced eutectic [63]. Below the eutectic temperature, development of the final 10% volume fraction of the β-intermetallics is observed to occur, via a ternary eutectic reaction of L → α-Al +

β-Al_5FeSi + Si. Similar results were reported in [11, 36, 63]. This result, however, is in contrast with the thermodynamic predictions shown in Figure 3.11 where the β-intermetallics preferentially form in the post Al-Si eutectic period.

3.3 Nucleation mechanisms

The nucleation temperature of each β-intermetallic plate was recorded and the development of each plate was tracked through the quantitative image analysis. This technique, used previously to study pore nucleation [129] (see Figure 2.4b), was applied in order to generate a histogram of nucleation density versus nucleation temperature and nucleation undercooling. The results are shown in Figure 3.12. Note that the bin size is 1°C and the nucleation undercooling (ΔT_n) is estimated to be the difference between observed nucleation temperature (T_n) and predicted nucleation temperature of 580°C from the thermodynamic calculation. A large nucleation temperature range for the β-intermetallics was observed, beginning from 579°C and ending at 568°C. Most of the nucleation events were observed at 574°C. At the temperature where the first β-intermetallic was recorded, 579°C, the primary α-Al solid fraction was measured to be ~0.3, indicating that the formation of β-intermetallic started well after the dendrite coherency point of this alloy (f_s~0.21) [149].

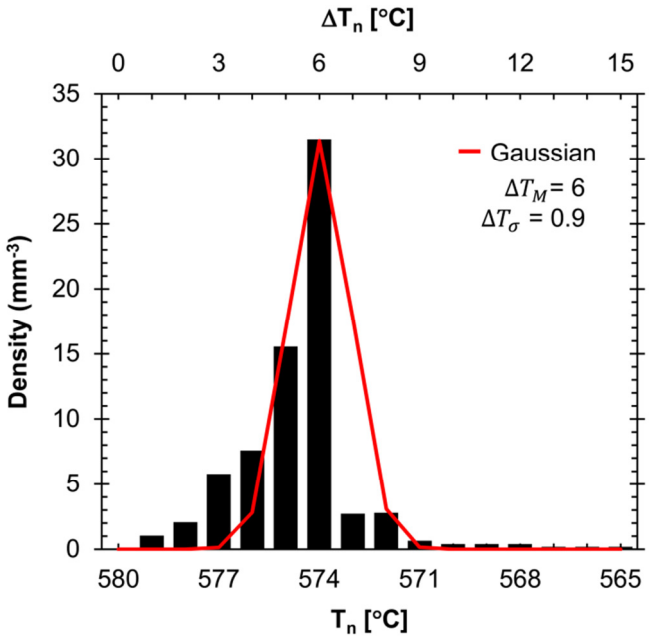


Figure 3.12 Histogram of the nucleation density of the β-intermetallic phase as a function of nucleation temperature (T_n) and nucleation undercooling (ΔT_n). The Gaussian distribution fitted on the histogram is also shown.

A Gaussian distribution was then fitted to each histogram in Figure 3.12 to characterise the nucleation density as a function of nucleation undercooling:

$$n = n_{max} exp\left(-\frac{(\Delta T_n - \Delta T_M)^2}{2\Delta T_\sigma{}^2}\right) \tag{3.1}$$

where n is the nucleation density of β-intermetallics per unit volume, n_{max} is the maximum nucleation density, ΔT_n is the nucleation undercooling, and ΔT_M and ΔT_σ are the respective mean and deviation of the Gaussian nucleation undercooling distribution. In this slow-cooling study, ΔT_M and ΔT_σ was found to be 6°C and 0.9°C respectively. The maximum activated nucleation density (n_{max}) was approximately 32 mm^{-3}. Equation (3.1), together with these values, can be used in analytic or numerical microstructural models of solidification, as demonstrated by Gandin and Rappaz [25] for grains and Lee and Hunt [26] for pores. Note that the observed n_{max} in this study is lower than what was suggested by Lee *et al.* [26] to use in a numerical model ($n_{max_{\text{Lee}}}$=100 mm^{-3}) for simulating β-intermetallic nucleation. This may be contributed

to the limited potential nuclei that can become activated. Lee and Hunt [182] observed and discussed similar contribution in pore nucleation.

Nucleation of β-intermetallics was observed throughout the entire specimen, both away from and near the specimen surface. Figure 3.13 highlights four main nucleation mechanisms. The first three, captured in a small volume of ~0.1mm^3 at the top right of the specimen shown in Figure 3.10, are rendered Figure 3.13a-f while another similar volume was rendered in Figure 3.13g-h. (1) The specimen surface, hypothesised to be the oxide Al_2O_3, proved to be an active nucleation site for β-intermetallics as previously observed by Terzi *et al.* [63]. As shown in Figure 3.13a-b, the red β-intermetallic first appears in contact with the specimen surface, without contact to any other surrounding pink β-intermetallics. (2) Nucleation also occurred in the bulk of the specimen. An example of nucleation away from the specimen's surface is shown in blue in Figure 3.13c-d. This independent nucleation event with no contact to any of the pre-existing β-intermetallics shown in pink either occurs very close to the α-Al dendrites, such as in Figure 3.13d, or in the remaining liquid. (3) Intermetallics themselves also appear to act as nucleation sites for new β-intermetallics, as shown in Figure 3.13e-f. At a distance from the specimen surface, the green β-intermetallic first appears in contact with the pre-existing blue β-intermetallic. (4) As-cast porosity will also nucleate the β-intermetallic, as shown in Figure 3.13g-h. As can be seen, the orange β-intermetallic forms on a pre-existing as-cast pore without connection to any other surrounding pink β-intermetallics.

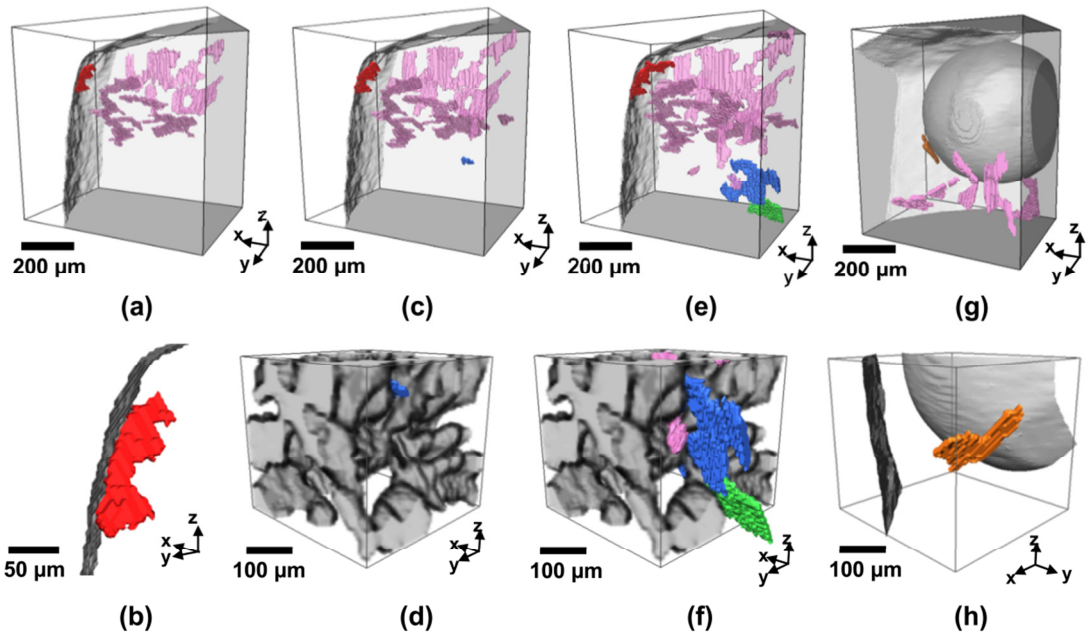


Figure 3.13 Examples of β-intermetallics nucleation mechanisms: (red intermetallic in a-b) specimen surface, (blue intermetallic in c-d) α-Al dendrite, (green intermetallic in e-f) existing intermetallic and (orange intermetallic in g-h) as-cast porosity. Al-dendrites and pores are rendered in grey whereas surrounding intermetallics are rendered in pink. Rendering volumes represent temperatures of (a-b) 579°C, (c-d) 578.5°C, (e-f) 578°C and (g-h) 576°C.

To quantify the contribution of each nucleation mechanism, every β-intermetallic in the second experiment was classified according to the above-mentioned categories: (1) specimen surface, (2) on/near aluminium dendrites, (3) existing β-intermetallics and (4) as-cast pores. This classification is summarised in Figure 3.14, and reveals that all four types of nucleation sites were active over a wide range of temperatures. Although the results confirm the observations of previous studies [64, 68], which suggest that aluminium oxide is an active nucleant for the β-intermetallic, it appears that the oxide is only one of many mechanisms of nucleation. By quantifying all the nucleation events, it can be seen that the most prevalent one is on/near aluminium dendrites (617 of 959 events, ~64%).

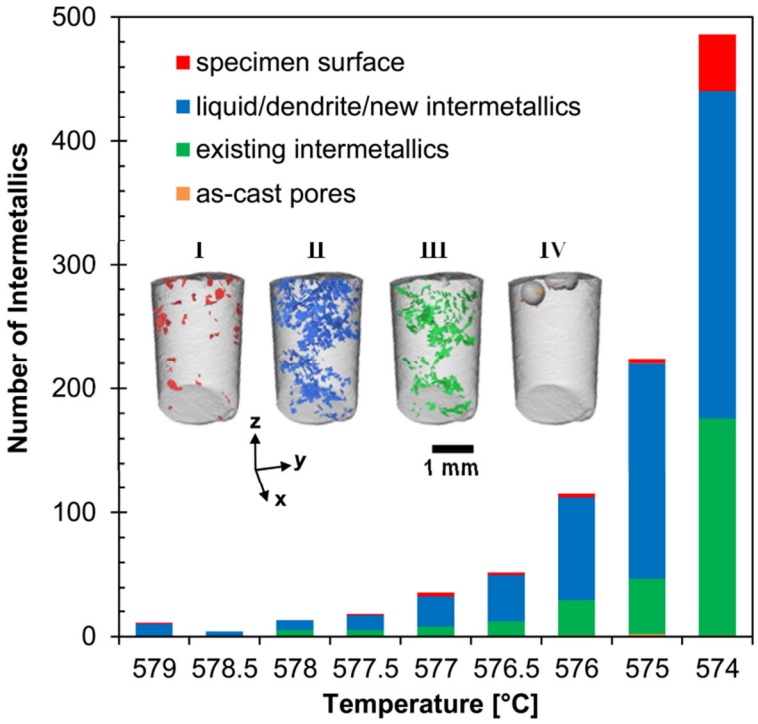


Figure 3.14 Quantified β-intermetallic nucleation rate, classified by 4 types of nucleation sites. Insets I-IV illustrate intermetallics that were nucleated on specimen surface, as-cast pores, existing intermetallics, and liquid/dendrite, respectively. Note that each intermetallic is rendered as it first appeared in the specimen.

This is contrary to previous observation by Terzi *et al.* [63] who detected nucleation events of 4 β-intermetallics limited to the vicinity of the aluminium oxide. As seen from the fast observations made in this study, β-intermetallics first nucleate near dendrites in a region close to the specimen surface due to the temperature gradient, and subsequently grow and come into contact with pre-existing β-intermetallics and/or the specimen surface. Even in this study, the value of 64% is a lower limit as the tremendous growth velocity in the early growth stages means capturing every 12 s may not entirely resolve nucleation before separated plates impinge. Nucleation of β-intermetallics on small entrained oxide films [68, 183], double oxide films (bifilms) [67], and aluminium phosphide nucleant (AlP) [47, 184] was not observed in this study. This observation, however, should not be used to invalidate these proposed nucleation mechanisms due to the different solidification conditions used in the various studies.

The relationship between β-intermetallic nucleation orientation and the aluminium dendrites was also examined by comparing the normal of each β-intermetallic to the orientation of the secondary dendrite arms. The normal vector of each β-intermetallic plate was determined using PCA and a pole figure was obtained using the orientation of the secondary dendrite arms as a reference direction. As shown in the schematic of Figure 3.15's inset, where a β-intermetallic is shown in red and its normal is shown with an arrow, if a β-intermetallic is perpendicular to the secondary dendrite arms direction, the pole is situated at the centre. If the plate is aligned parallel to the secondary dendrites, the pole is located on the circumference. By integrating the pole-figures for all the intermetallics, a contour plot is obtained and shown in Figure 3.15a. In this contour plot, higher concentrations are shown in red whereas each white dot represents a calculated pole-figure. It is shown that the concentration is mostly along the circumference, indicating that β-intermetallic plates align preferentially along the orientation of the secondary dendrite arms.

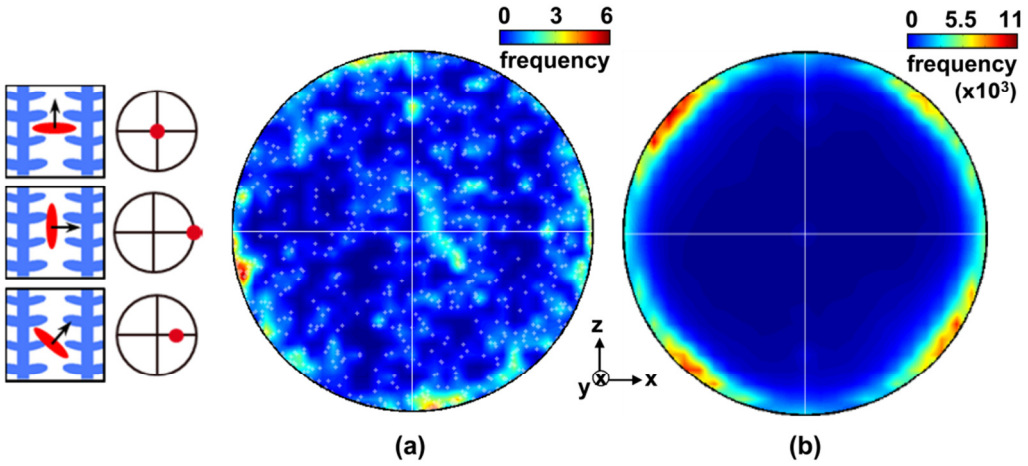


Figure 3.15 (a) Orientation contour plot of the normal distribution of all intermetallic plates as compared to the growth directions of the secondary dendrite arms; (b) IND of the dendritic structure. Each white dot in (a) represents the normal of each plate. The insets illustrate how each white dot was determined.

In order to quantify the directionality of the primary aluminium dendrite structures in the specimen, the interface normal distribution (IND) [180], detailed in

section 3.1.6, was calculated and is shown in Figure 3.15b. The result illustrates a strong 4-fold symmetry of the equiaxed dendritic structure, thus implying that the β-intermetallics frequently nucleate with a preferential crystallographic orientation to the primary dendrites via growing in the space between secondary dendrite arms.

3.4 Growth kinetics

After nucleation, the β-intermetallics grow very rapidly in the lateral direction. The growth evolution of individual β-intermetallics during this initial spurt growth period is shown in Figure 3.16. Intermetallics initially grow with a thin plate-like morphology [60]. However, these experiments show that it is the restriction of their growth to the interdendritic regions, impinging on dendrites, that causes them to acquire very complex plate shapes with branches and holes, as demonstrated in Figure 3.16b-c. The growth progresses rapidly in the lateral direction during the initial growth stage. Despite the presence of obstructing dendrite arms, β-intermetallics can continue growing in their preferred direction by growing around the obstacles. This seems to occur with ease, and the sides of the plate growing around the obstructing arms can join up again, creating a cavity in the β-intermetallic as shown in Figure 3.16d. The growth also propagates through a narrow gap between the dendrite arms and enlarges its growth front after passing the constraint gap as shown in Figure 3.16b. Intermetallics can sometime develop/deform into bent plates, as shown in in Figure 3.16e. It is observed that after their impingement the plates can also grow along nearby developing plates. In a few cases, the plates can even grow around an obstructing β-intermetallic, such as Figure 3.16f where the blue plate grows around an obstructing green plate.

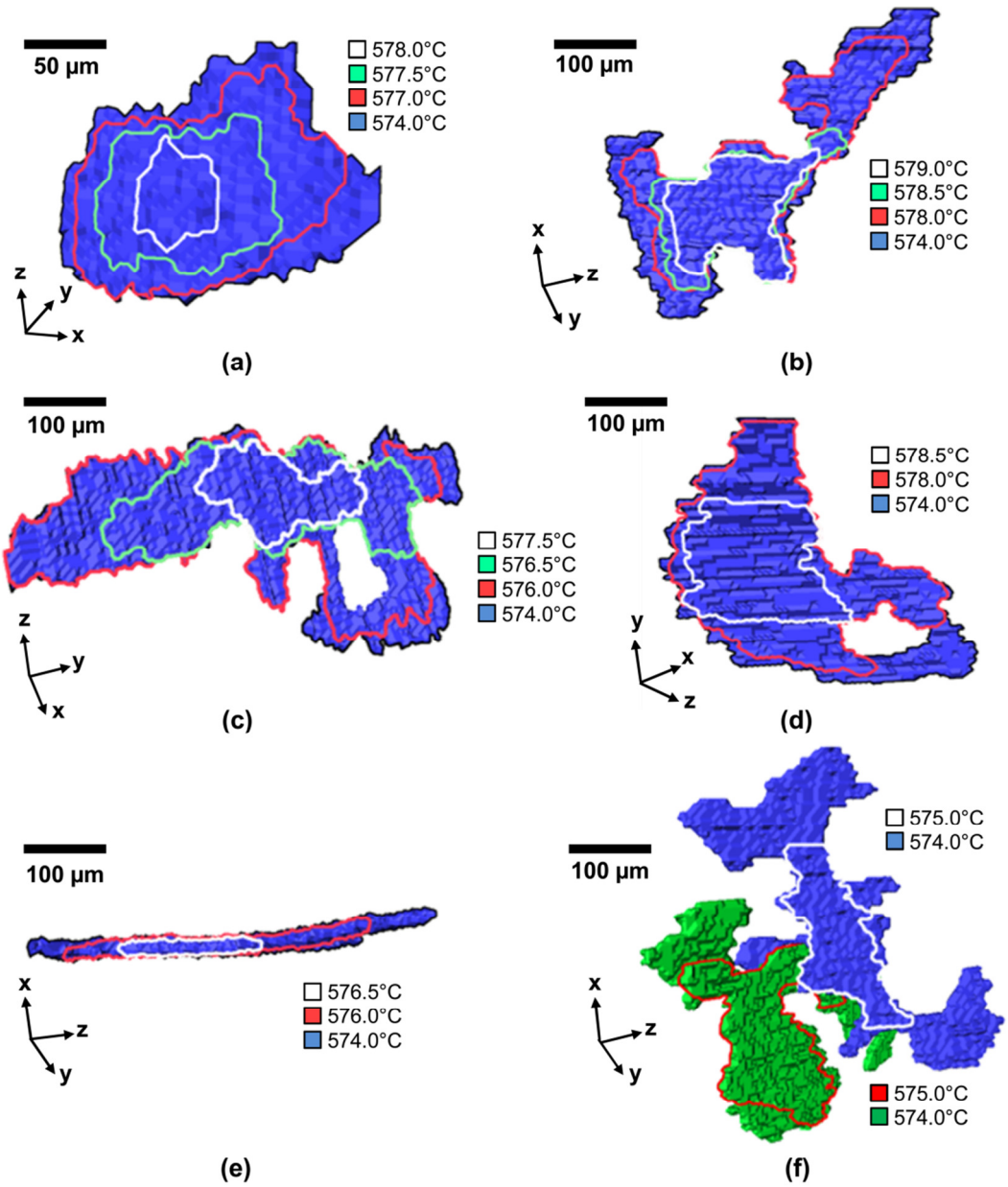


Figure 3.16 The different growth evolutions of β-intermetallics during solidification: (a) standard plate-like growth, (b-c) growth of complex plate-like shapes, (d) growth around dendrite arm and subsequently forming a cavity by joining up the separated growth, (e) formation of bent intermetallic and (f) growth of one intermetallic passing an obstructing intermetallic.

By calculating the maximum length of each β-intermetallic along its most preferential growth direction, i.e. along the first principle component of each plate (as discussed in section 3.1.6), the distribution of the maximum β-intermetallic length as a function of temperature can be determined, as shown in Figure 3.17. As each β-

intermetallic nucleates at a different temperature, the undercooling relative to each β-intermetallic nucleation temperature (T_n - T) was used to compare growth behaviour. A narrow distribution of β-intermetallic length is observed at the temperature where the β-intermetallics first appear (T_n - T = 0). For larger temperature differences (i.e. for greater times after nucleation), broader distributions are observed. This broader variation in β-intermetallic length corresponds to the greater complexity of microstructure toward further solidification. Intermetallics can grow easily in regions with larger interdendritic spaces, while growth is more restrained by the limited space at higher fraction solid.

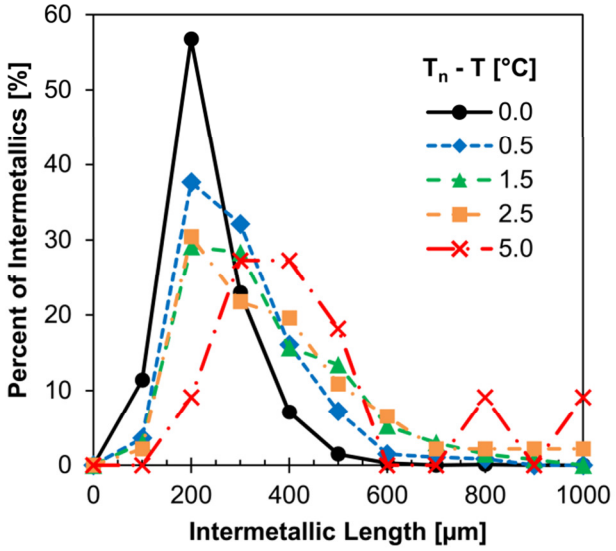


Figure 3.17 Distribution of β-intermetallic length at different temperatures after nucleation (T_n - T).

Figure 3.18 illustrates that the average β-intermetallic length is ~180 μm when imaged immediately after nucleation. The average length of β-intermetallics with similar temperature differences significantly increases with increasing temperature difference. It increases rapidly from ~180 μm to ~300 μm only 2°C after nucleation and slowly reaches ~350 μm 3°C afterwards, as shown in Figure 3.18.

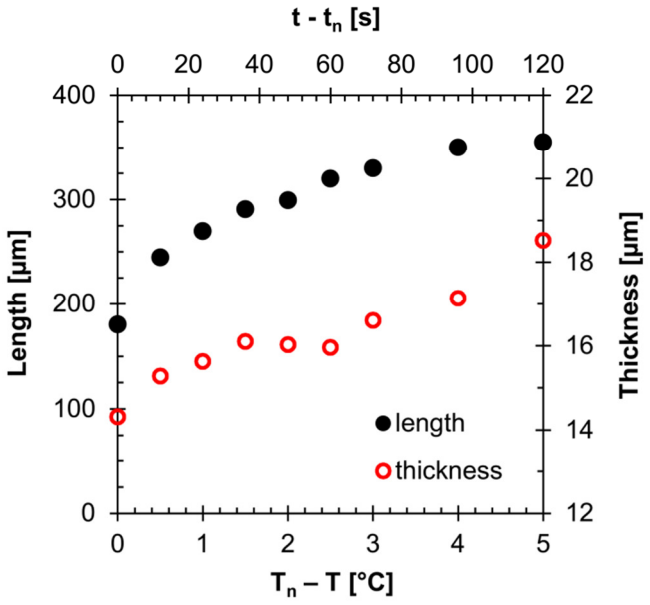


Figure 3.18 Average length and thickness of intermetallics as a function of temperature (T_n - T) and time (t - t_n) after nucleation.

The second part of Figure 3.18 describes the increase in thickness of the β-intermetallics with decreasing temperature (i.e., greater T_n - T). The measured thickening rate of the plates was found to be much slower than the lateral growth rate. This is most likely due to slower attachment kinetics resulting from the difficulty of depositing atoms on the facet plane [60].

To investigate the mean initial growth velocity as a function of nucleation undercooling, an average of the initial growth velocity for all β-intermetallics that nucleate at the same temperature (T_n) was calculated, i.e. an average for β-intermetallics having the same nucleation undercooling (ΔT_n). The result is shown in Figure 3.19a. Although there is a small variation in the plot, it can be seen that initial growth velocity of β-intermetallics increases with nucleation undercooling. The relationship between initial β-intermetallic velocity and nucleation undercooling can be described by a power function:

$$v = a + b(\Delta T_n)^m = 12.84 + 13.79(\Delta T_n)^{0.14} \quad (3.2)$$

where v is growth velocity and a, b, m are fitting parameters. The application of nonlinear least-squares regression gives a=12.84, b=13.79 and m=0.14. This result confirms the key role of undercooling with respect to the lateral growth of β-intermetallics, as well as providing an easy-to-use equation for microstructural models. Solidification time can be used instead of nucleation undercooling, although it will be cooling rate dependent.

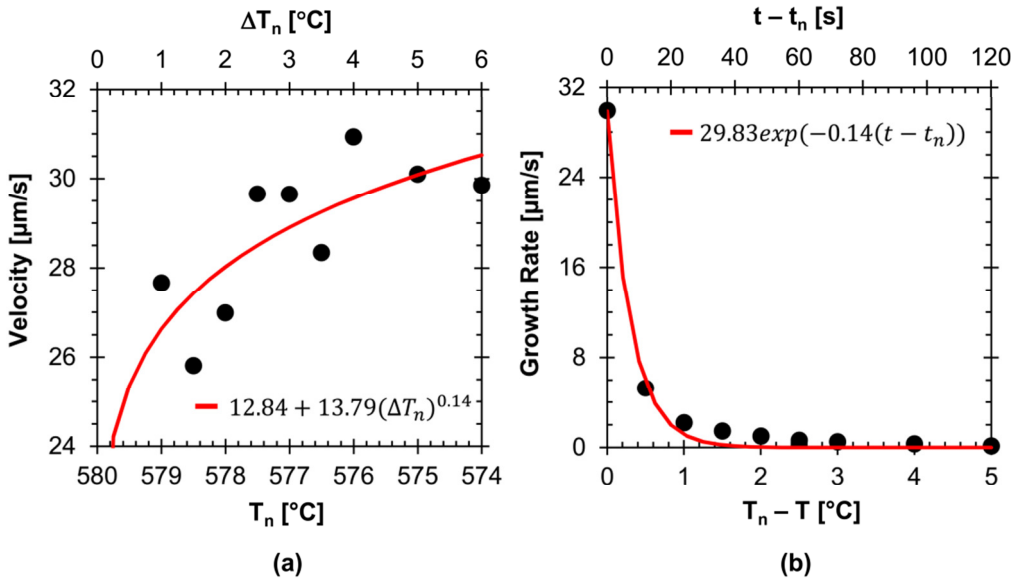


Figure 3.19 (a) Average initial growth velocity as a function of nucleation temperature (T_n) and nucleation undercooling (ΔT_n), and (b) mean growth velocity as a function of temperature (T_n - T) and time (t - t_n) after nucleation.

The mean lateral growth velocity as a function of time/temperature after nucleation is illustrated in Figure 3.19b. It is worth noting that, unlike Figure 3.19a, the growth velocity average was calculated using β-intermetallics that share both the same temperature (T_n - T) and the same time (t - t_n) after nucleation events. The mean growth velocity is observed to be highest at the first growth step (~30 µm/s). It then decreases exponentially with increasing time (which further reduces temperature) and reaches ~1 µm/s 50s after nucleation. A decrease in growth velocity with time can be described as:

$$v = p \times \exp\big(q(t - t_n)\big) = 29.83 \times \exp\big(-0.14(t - t_n)\big) \quad (3.3)$$

where v is growth velocity, $t - t_n$ is time difference after nucleation, and p=29.83 and q=-0.14 are fitting parameters. It is worth nothing that this equation is only for a cooling rate of 3°C/min.

Rapid lateral growth in the early stages of β-intermetallic growth has previously been observed in a similar alloy system with higher Fe-levels (0.8 wt.%Fe): a growth rate of 12.5 μm/s was measured at a very slow cooling rate (1.4°C/min) [63] and an average growth rate of 34 μm/s with a maximum growth rate of 100 μm/s was found at a much higher cooling rate (20°C/min) [36]. After the initial rapid growth, solute depletion significantly contributes to the large decrease in the growth rate, as seen in Figure 3.19b. This decrease may also be impacted by the physical blocking caused by surrounding aluminium dendrites and nearby growing β-intermetallics. Although lateral β-intermetallic growth can still continue by growing around the obstacles, as shown in Figure 3.16, it happens at a much slower speed compared to the initial rapid growth.

Both the lateral growth and the thickening of β-intermetallics are largely completed before the formation of the Al-Si eutectic. The final morphology of β-intermetallics is thus relatively unaffected by the growth of the Al-Si eutectic. During the entire solidification, the β-intermetallic phase grows as faceted plates, due to its large entropy of fusion [185] (as previously discussed in section 2.1.2). In this alloy system, the Jackson's α factor ($\Delta S_f^m/R$) was reported with a range of values greater than 2 [63]. This α>2 indicates that the phase has a large anisotropic solid-liquid interfacial energy (typically atomically sharp interface) and is faceted.

3.5 Intermetallic-intermetallic interactions

During solidification, both pre-existing and newly formed β-intermetallics often make contact with other surrounding β-intermetallics. Three types of interaction between intermetallics were observed in this study and are summarised in Figure 3.20. The first type of intermetallic-intermetallic interaction corresponds to an impingement mechanism. This occurs when two (or more) separated β-intermetallics grow towards each other and impinge on one another. Impingement of β-intermetallics can occur at various angles – high (Figure 3.20a), medium, and low (Figure 3.20b). It can also be seen that impingement does not entirely stop intermetallic growth. After impingement, the growth of each β-intermetallic can still continue both along the contact points and in other directions. As shown in Figure 3.20c, impingement of multiple β-intermetallics can also occur. This impingement mechanism leads to the formation of complex β-intermetallic clusters. Plate-like intermetallics initially nucleate separately, grow with high lateral speed and subsequently impinge onto surrounding β-intermetallics. Since the nucleation of two (or more) independent β-intermetallics can occur at very similar times and is followed by very rapid growth, insufficient temporal resolution may not allow capture of all the impingement events.

The second type of intermetallic-intermetallic interaction occurs when new β-intermetallics appear already in contact with pre-existing β-intermetallics. The interaction may potentially correspond to the hypothesised branching mechanism [63]. Similar to impingement, branching was observed at various angles – high, medium (Figure 3.20d) and low (Figure 3.20e). In a few cases, complex branching was observed. As shown in Figure 3.20f, two new β-intermetallics (green and pink) are both branches of one parent β-intermetallic (blue), with the green β-intermetallic directly branched out from the parent and the pink β-intermetallic indirectly branched out from a branch of the parent β-intermetallic. It is possible that impingement may have actually

occurred instead of branching. This incidence of very rapid growth interaction, however, requires faster time-resolution during acquisition. In this study, these instances were classified as "potential branching" in order to separate them from direct impingement events.

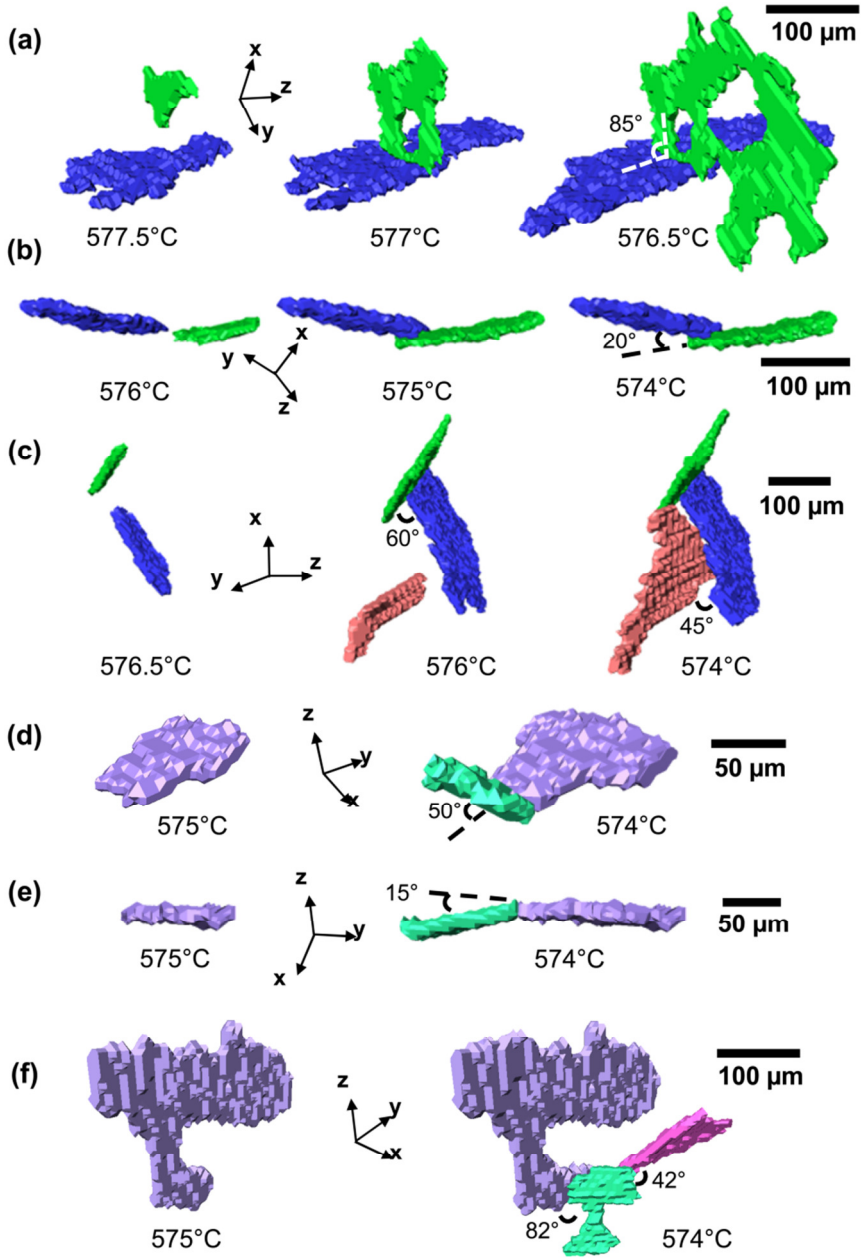


Figure 3.20 Types of intermetallic-intermetallic interactions: (a-c) impingement mechanism and (d-f) potential branching mechanism. Measurements of 3-D angles between each contact are also detailed.

The third interaction is referred to as "unclassifiable". Any interaction is put into this category when two or more β-intermetallics already in contact appear but are totally separated from any pre-existing β-intermetallics. Improved temporal resolution is required to further investigate this type of interaction.

By classifying every intermetallic-intermetallic contact using the aforementioned criteria, the number of occurrences of different types of interactions as a function of temperature was obtained and is shown in Figure 3.21. The three intermetallic-intermetallic interactions are schematically illustrated in insets I-III of this image. It is found that intermetallic-intermetallic contacts increase with deceasing temperature. All three types of interaction were observed at all temperatures, but branching and impingement take a slight precedence (~40% and ~37%, respectively). Angles between each intermetallic-intermetallic contact were measured in 3-D, for all three categories. The measurements are similar to those shown in Figure 3.20. The result is plotted as a histogram in inset IV of Figure 3.21. All three types of interaction exhibit a large range of contact angles, and there does not seem to be preferential angles between intermetallic-intermetallic contacts, neither for impingement nor for branching interactions.

Distributions of measured contact angles therefore demonstrate no difference between the branching and impingement mechanisms. As clearly illustrated in the inset IV of Figure 3.21, both branching and impingement can occur at various angles ranging from high, medium, to low angles. This may imply that these branching events are potentially associated with physical obstructions and may not be crystallographically related. It has been suggested in the literature that the β-Al_5FeSi intermetallic can grow by a twin plane re-entrant edge mechanism [63] since it has a twinning fault structure on the (001) plane [53, 60] (as reviewed in section 2.2.3.2). By considering the distribution spread of angles in the branching category, two

mechanisms can be hypothesised: either (1) it is more likely that branching occurs via a sideways growth mechanism rather than a twin branching mechanism, or (2) these branching observations are simply unresolved impingement events.

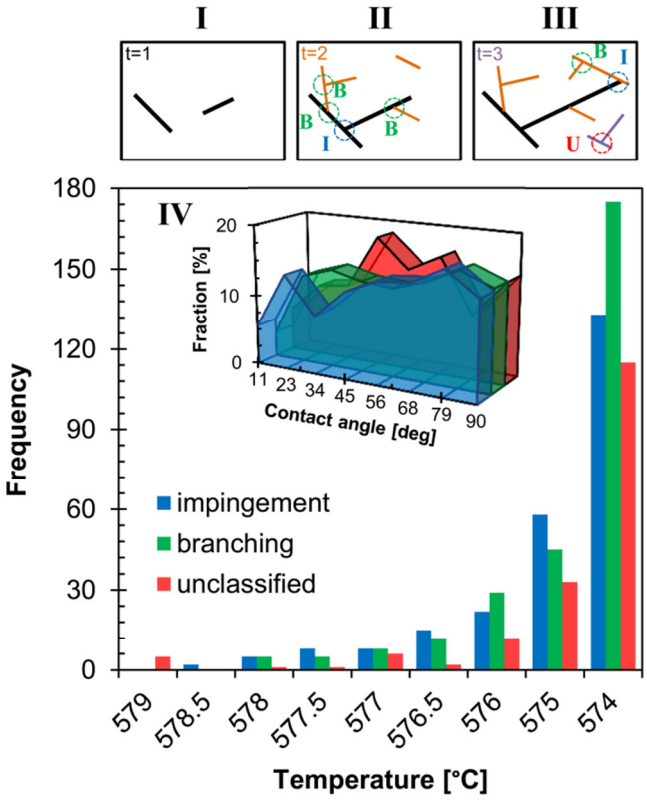


Figure 3.21 Quantified number of occurrences of different types of intermetallic-intermetallic interactions. Insets I-III illustrate criteria used to classify growth interactions into (I) impingement, (B) branching, and (U) unclassifiable. Inset IV plots the histogram of angles between each contact over different types of interactions.

Terzi *et al.* [63] have previously attempted to observe intermetallic-intermetallic interactions. They showed only branching events, with no direct observation of impingement. In their work, each 3-D tomographic volume was obtained in 36s and a total time to scan one 3-D volume and prepare for the next scan was 57s, producing a temperature change of ~0.8°C within a scan and ~1.4°C between two adjacent scans. As shown in Figure 3.10, a large amount of β-intermetallic growth will occur during 0.8°C cooling. It is therefore highly possible that some of their branching events may actually be β-intermetallics impinging on one another.

3.6 Summary

The formation of β-Al_5FeSi intermetallics during solidification of an Al-7.5Si-3.5Cu-0.6Fe (wt.%) alloy was quantitatively investigated in this chapter via *in situ* synchrotron x-ray tomography. Two *in situ* solidification experiments, under the same conditions, were performed at capture rates of 72s and 12s respectively in order to observe both the slower kinetics of a full solidification sequence and the initial nucleation and rapid growth of β-intermetallics.

Findings show the nucleation of the β-intermetallics is observed throughout the volume of the specimen and evolves over a range of temperatures. Nucleation events are observed both inside the specimen volume, e.g., near the primary aluminium dendrites, bulk liquid, as-cast pores, and existing β-intermetallics, and outside the specimen volume at the oxidised specimen surface. A good correlation between nucleation density and nucleation temperature is found and can be described using a Gaussian distribution. The β-intermetallics have a strong preferential orientation parallel to the secondary dendrite arms of the α-Al dendrites, suggesting that they nucleate on this phase.

After a nucleation event, β-intermetallics initially grow rapidly in the lateral direction via effective solute rejection at the edges of the plates. A higher initial growth velocity is observed and driven by higher undercooling. Following the initial growth phase, β-intermetallic plates continue evolving along preferential directions and have the ability to grow around and in between obstructing primary dendrite arms. The mean lateral growth velocity is observed to decrease exponentially with time after nucleation occurs. Thickening of the plates is also observed but at a much slower rate compared to lateral growth. Direct impingement and potential branching, which result in a very complex morphology of interconnected β-intermetallic clusters, are observed with a wide range of contact angles, indicating that these events might not be

crystallographically related. It is proposed that growth is governed by lateral growth mechanisms and is dominated by impingement events.

The following chapter will demonstrate how these improved insights into the nucleation mechanisms and growth dynamics of β-intermetallics are critical to the evolution of permeability in intermetallic-rich solidifying microstructures.

Chapter 4

Influence of β-intermetallic formation on permeability*

The characterisation of nucleation and growth kinetics of β-Al_5FeSi intermetallics detailed in the previous chapter has demonstrated how the β-intermetallics form and develop into complex connected clusters within the interdendritic regions upon solidification. This previous observation has highlighted the need to achieve a better understanding of how these complex β-intermetallics affect flow and feeding in the solidifying microstructures. Since this resistance to fluid flow is closely linked with the defect formation, as shown in Chapter 2, insights into influence of β-intermetallic formation on permeability is critical to design better alloys and applications.

In this chapter, coupled *in situ* imaging and numerical fluid flow simulations were developed to investigate the influence of β-intermetallics on the interdendritic flow

* Note, this chapter in modified form has been accepted for publication in Acta Materialia as the paper entitled "Coupling in situ synchrotron x-ray tomographic microscopy and numerical simulation to quantify the influence of intermetallic formation on permeability in aluminium-silicon-copper alloys" by Puncreobutr, C., Phillion, A.B., Fife, J.L., Lee, P.D.

and permeability. Unlike previous numerical studies of permeability (as detailed in section 2.3.2) that utilised quenched specimens in combination with post-mortem tomographic imaging [106-110], this work has extracted the geometry directly from a microstructure captured during solidification. This is the first use of *in situ* tomography for such studies, and the results provide a novel, detailed permeability assessment of an individual microstructure morphology that is changing both in solid fraction and in intermetallic phase evolution rather than assessing a post-mortem set of snapshots typically given by quenched experiments.

The chapter is split into 6 sections. The first section presents the method for coupling *in situ* tomographic imaging with numerical CFD modelling that is used in this study. The second section reviews the microstructural evolution observed via *in situ* tomography. The third and fourth sections explore simulated results of flow and permeability. The analytical permeability expression with particle blockage factor is introduced in the fifth section. Finally, a comparison between the present study and the published literature is addressed in the sixth section.

4.1 Methods

A method for coupling *in situ* synchrotron x-ray tomographic imaging with numerical computational fluid dynamic (CFD) modelling consists of three steps as described below.

4.1.1 *In situ* tomographic imaging

In order to obtain intermetallic-containing solidifying microstructures of a commercial Al-A319 alloy at varies solid fractions, the results obtained from the first *in situ* solidification experiment in Chapter 3 are used in this chapter. As full details of the experimental procedure were given in sections 3.1.1 and 0, only brief details are

provided here. The experiment was conducted on a commercial Al-A319 alloy with composition Al-7.52wtSi-3.53Cu-0.59Fe (wt.%) at the TOMCAT beamline of the Swiss Light Source (Paul Scherrer Institut, Switzerland) [162] using a bespoke resistance furnace (Figure 3.2). In this experiment we first gradually heated the specimen to 650°C, then held it for 5 minutes to ensure thermal equilibrium, and finally cooled it to below the solidus temperature (505°C) of the specimen at a rate of 0.05°C/s. During the cooling stage, 1001 radiographs were captured over 180° of rotation in 2 s, and this image acquisition sequence was repeated every 70 seconds. From these images and the corresponding angular information, tomographic 3-D volumes of 1104x1104x1468 voxels with a voxel size of 2.75 μm per side were generated using reconstruction procedure described in section 3.1.3.

In total, thirteen 3-D volumes were acquired during the solidification sequence over a solid fraction range between 0 and 0.85. Although the time between sequential 3-D volumes was approximately 1 minute due to camera memory limitations, the fast tomographic imaging (2 s) and slow cooling rate ensured that the microstructural evolution during acquisition of the radiographs for a single 3-D volume was small, minimising movement artifacts.

There was a small thermal gradient present in the furnace during cooling, which resulted in the solidification microstructure being dendritic elongated in the heat extraction direction. Figure 4.1 shows a 3-D rendering of the full dendritic structure that was captured at 582±1°C, corresponding to a solid volume fraction of 0.27. Note that the calculation of solid fraction was done by applying a marching cubes algorithm [173] on the segmented solid phase, as described in section 3.1.6. The process of image segmentation is detailed in the following section.

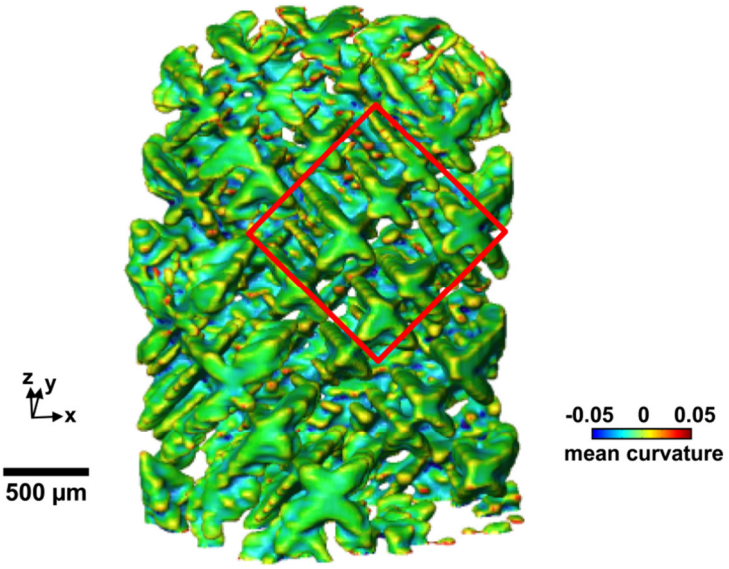


Figure 4.1 Rendering of the full dendritic structure from the dataset captured at 582±1°C (f_S=0.27), coloured by the local mean curvature. The highlighted box (red) is the region chosen for the permeability study.

4.1.2 Preparing datasets for flow simulation

After image acquisition, significant post-processing was necessary to prepare non-permeable domains for flow simulations. First, all of the 3-D datasets were rotated to align the primary dendrites with the *x*-axis in order to reduce errors in the flow studies. Second, a sub-volume of 400^3 voxels was extracted from each 3-D volume to reduce the computational cost. This volume meets the mesh size and physical length scale requirements for a representative volume element previously identified by Bernard *et al.* [106] and Fuloria *et al.* [109]. Third, a 3-D anisotropic diffusion filter [171] was applied to each dataset to reduce noise. Last, 3-D region growing segmentation [172] and manual segmentation processes were applied to separate the Al-rich dendrites along with Al-Si eutectic (if present) and the *β*-intermetallics from the solidifying liquid, respectively. More details regarding to noise reduction and segmentation processes can be found in section 3.1.4.

An example of this process is shown in Figure 4.2, with Figure 4.2a corresponding to the original data rotated and a smaller volume selected (i.e. the

highlighted box in Figure 4.1), Figure 4.2b,c corresponding to the segmented Al-rich and β-intermetallic phases respectively, and Figure 4.2d,e corresponding to the full segmented datasets both without and with β-intermetallics, respectively, for use as the input geometries for the numerical simulations.

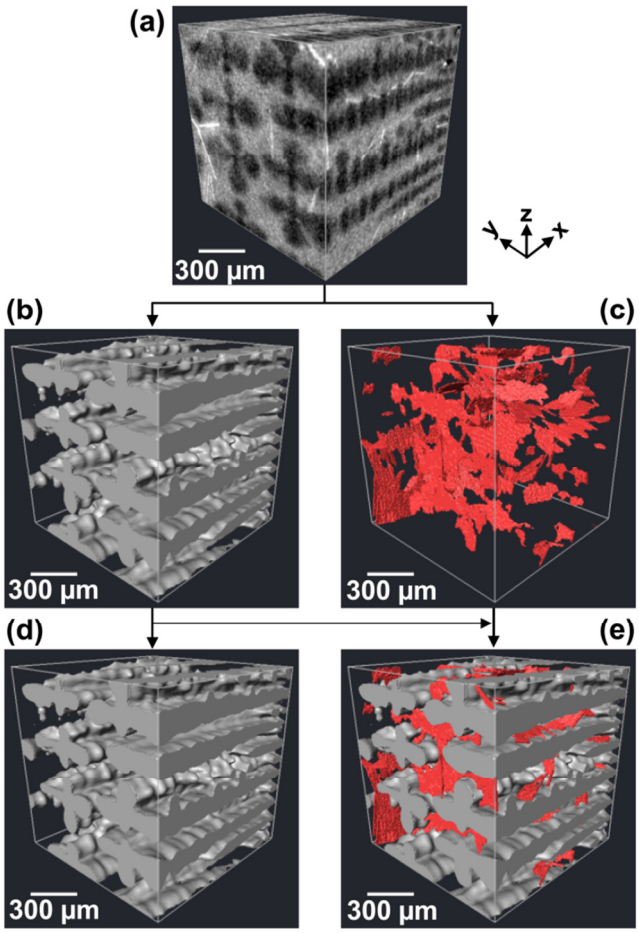


Figure 4.2 Schematic outlining the segmentation process utilized to obtain the non-permeable domain for the CFD calculation: (a) original data, (b) segmented primary Al, (c) β-intermetallics, and final non-permeable structure both (d) without and (e) with β-intermetallics.

4.1.3 Flow simulation

In order to determine the evolution of permeability in the semi-solid Al-A319, the flow problem based on Stokes equations was simulated in the thirteen tomographic datasets using the commercial CFD software Avizo XLab Hydro (VSG, France). This software, developed based on research by Bernard *et al.* [106], utilises a finite volume

method applied directly to a tomographic dataset for flow predictions. The Stokes equation describing interdendritic flow at the microscopic scale can be expressed as:

$$-\nabla P_L + \mu_L \nabla^2 v_L = 0 \tag{4.1}$$

$$\nabla \cdot v_L = 0 \tag{4.2}$$

where ∇P_L is the pressure gradient in the liquid, μ_L is the viscosity, and v_L is the superficial flow velocity of the liquid. Note that gravity was ignored. 50 voxel layers of divergence and convergence channels, as shown in Figure 4.3, were added to both the inlet and outlet faces in order to create a fluid stabilisation zone where the pressure is quasi-static and the liquid can freely spread on the inlet face [186].

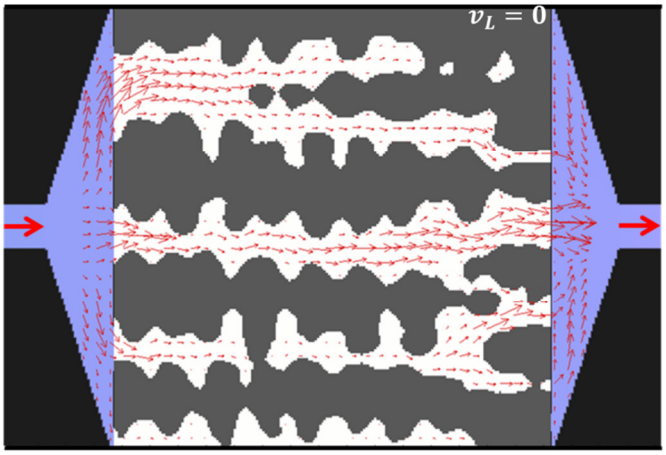


Figure 4.3 Simulation setup for CFD calculation.

The flow studies were performed in each of the three directions along the *x*, *y*, and *z* axes of the 3-D volume, both with and without β-intermetallics. As the primary dendrites were aligned with the *x*-axis, inlet-flow along the *x*-axis gives the permeability for liquid flow parallel to the primary arms, while permeability in the normal direction was taken as the average value calculated with inlet flows along the *y*- and *z*-axes. The boundary conditions for the flow simulations were as follows: a low Reynolds number velocity inlet (Re<0.1), free pressure outlet (0 Pa), no-slip conditions on the remaining four outer walls, and no-slip conditions on the interior walls

representing solid-liquid interfaces. The liquid viscosity was given a value of 0.001 Pa·s [187].

4.2 Microstructural evolution

Longitudinal slices taken from the 3-D tomographic datasets showing the semi-solid microstructure of Al-A319 are shown in Figure 4.4 for 582±1°C, 575±1°C, 568±1°C, and 555±1°C. It can be seen that the contrast between each phase is excellent. Primary Al-rich dendrites and Al-Si eutectic appear dark, the β-intermetallics appear very bright, and the solidifying liquid is grey. This high contrast allowed for good segmentation of the structure for the flow simulations. As solidification proceeds, the individual dendrites grow (Figure 4.4a), β-intermetallics form (Figure 4.4b) and finally the Al-Si eutectic phase forms in the interdendritic regions, which completes the solidification process (Figure 4.4d). Concurrently, the primary and secondary dendrite arms appear to be growing and coarsening (Figure 4.4b-c).

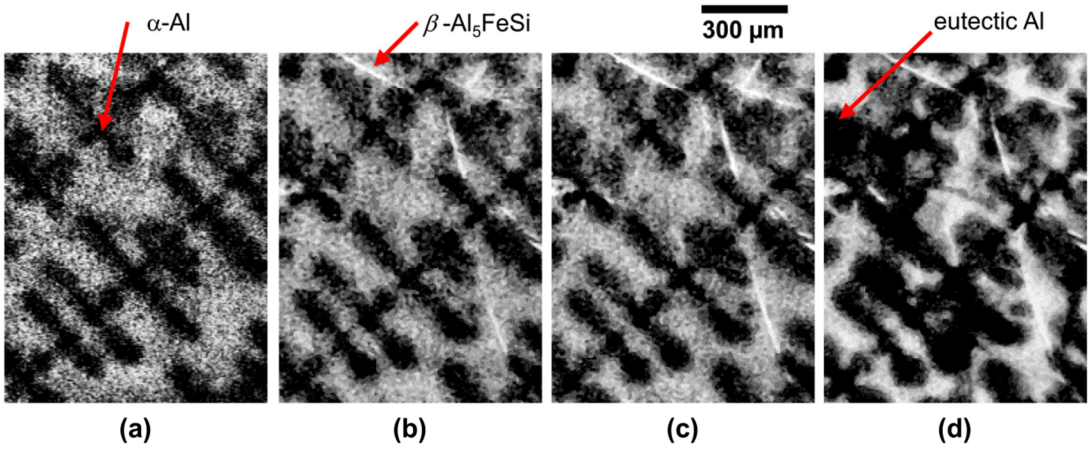


Figure 4.4 Longitudinal images acquired via x-ray tomographic microscopy showing the typical microstructure evolution of Al-7.5Si-3.5Cu-0.6Fe (wt.%) during solidification. The images (a-d) represent microstructure at temperatures of 582±1°C, 575±1°C, 568±1°C and 555±1°C, respectively. The corresponding solid fractions were calculated to be 0.23, 0.30, 0.39, and 0.78, respectively.

The experimentally-observed evolution of solid fraction of all phases (f_S) and β-intermetallic fraction alone (f_I) both as a function of temperature, along with the

corresponding lever-rule, and Scheil limits are shown in Figure 4.5. Each square (f_S) and circle (f_I) represents the value obtained from each of the thirteen tomographic datasets acquired during solidification. The solid fractions for the four slices given in Figure 4.4 are indicated by the dashed lines labelled I-IV in Figure 4.5, which provides clarity and direct comparison between the two figures. The values derived from the 3-D images match closely to the lever-rule approximation for this slowly solidifying case. There is also a good match in the sequence of phase formation, i.e., the tomographic images adequately capture the initiation of the β-intermetallic precipitation at 578±1°C (compared to 580°C from thermodynamic calculations) as well as the initiation of the eutectic transformation at 561±1°C (compared to 565°C from the prediction). The high degree of similarity in the solidification sequence between the 3-D images and theory provides good confidence in the segmentation methodology and thus the input geometries for the resulting flow simulations; they can be assumed to provide an excellent quantitative characterisation of the actual solidification microstructure.

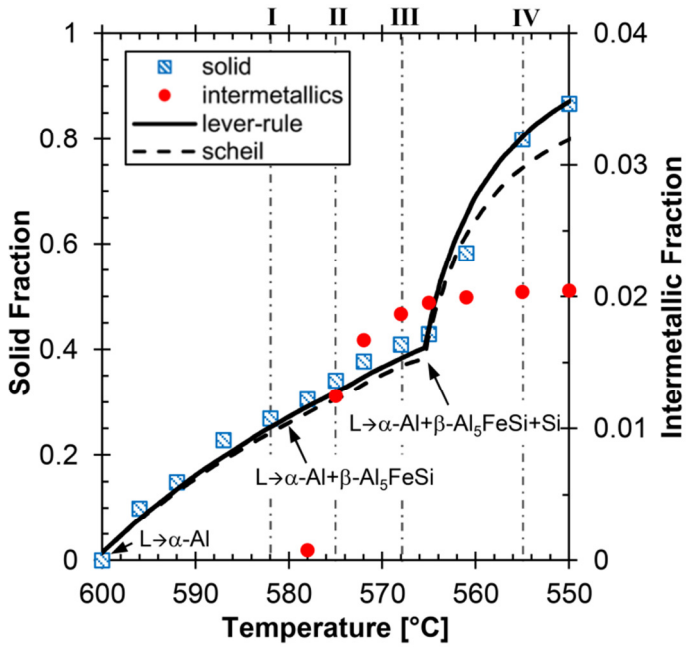


Figure 4.5 The evolution in f_S and f_I observed in the *in situ* 3-D imaging of solidification as compared to the lever-rule and Scheil behaviour. Each discrete point (square, circle) represents one 3-D tomographic dataset, while the lines I-IV represent the f_S corresponding to images (a-d) in Figure 4.4. The sequence of phase formation is also indicated.

4.3 Flow simulations

The pressure contours and flow velocities resulting from the flow simulations in the x-direction, parallel to the primary dendrites, are shown in Figures 4.6 and 4.7 for various temperatures in the semi-solid regime. These images show the liquid domain (i.e., the inverse of the segmented regions shown in Figure 4.2) for f_S ranging from 0.30 to 0.56 in the cases without (left column) and with (right column) β-intermetallics. It can be seen in Figure 4.6 that the pressure required for flow increases with increasing solid fraction, as expected (Figure 4.6a at f_S=0.30, Figure 4.6c at f_S=0.36, Figure 4.6e at f_S=0.41). The addition of β-intermetallics (Figure 4.6b at f_S=0.30, Figure 4.6d at f_S=0.36, Figure 4.6f at f_S=0.41) causes a significant change in the pressure contours. Comparing Figure 4.6c with Figure 4.6d, and also Figure 4.6e with Figure 4.6f, it is clear that there is a strong increase in the pressure required for fluid flow when β-intermetallics are present. Figure 4.6g-h provide a measure of the interaction between the liquid, primary dendrites, and β-intermetallics at f_S=0.33, and show the fluid velocity through the channels in 3-D. The β-intermetallics are large and plate-like, and it is immediately clear that they will block many of the channels, and accommodate these blockages by either: restricting flow to the few channels that remain unblocked by β-intermetallics, or force flow back and forth between channels in order to go around the blockages. This second case would be particularly relevant as β-intermetallic growth progresses and every channel contains β-intermetallics.

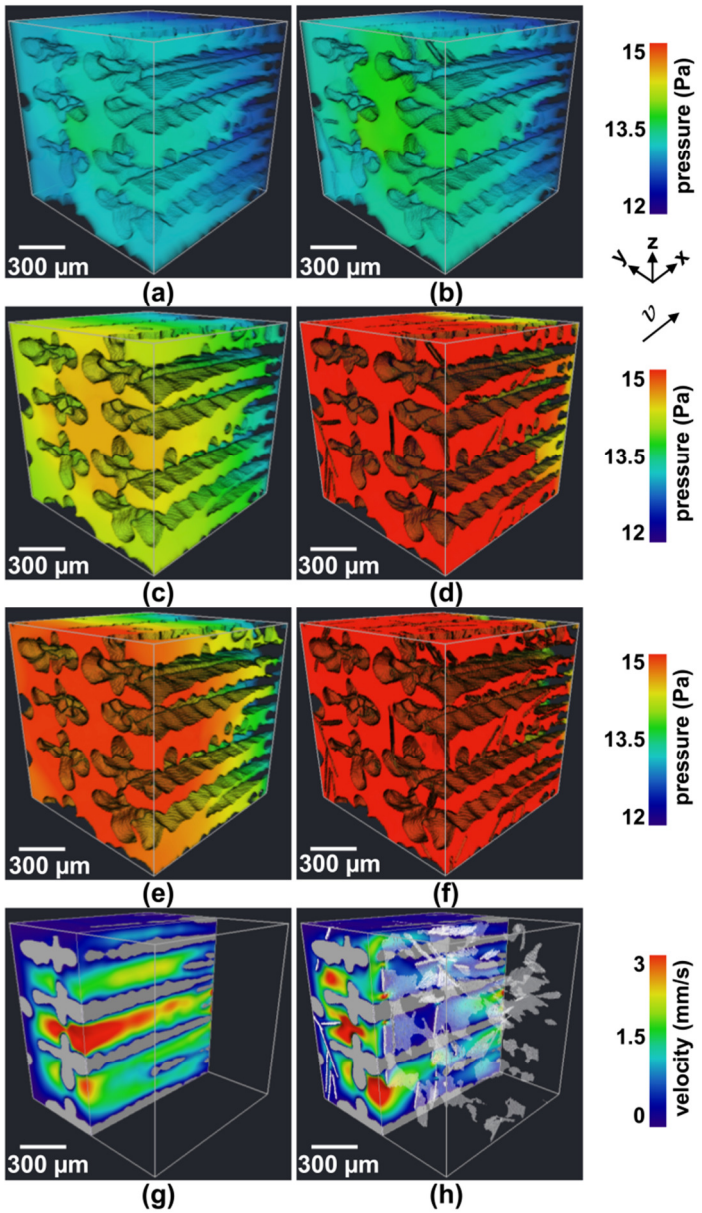


Figure 4.6 Simulated pressure contours in the interdendritic liquid region (i.e., the negative volume of Figure 4.2) both (a,c,e) without and (b,d,f) with β-intermetallics. The 3-D microstructures shown represent the pressure contours at solid fraction of (a,b) 0.30 (578°C), (c,d) 0.36 (572°C), and (e,f) 0.41 (565°C). The corresponding simulated liquid velocities both (g) without and (h) with β-intermetallics shown represent solid fraction of 0.33 (575°C).

Cross-sectional images showing the fluid velocity magnitudes in the solidifying microstructures are given in Figure 4.7. Fluid flow occurs from left-to-right, and the qualitative effect of the β-intermetallic is now plainly evident.

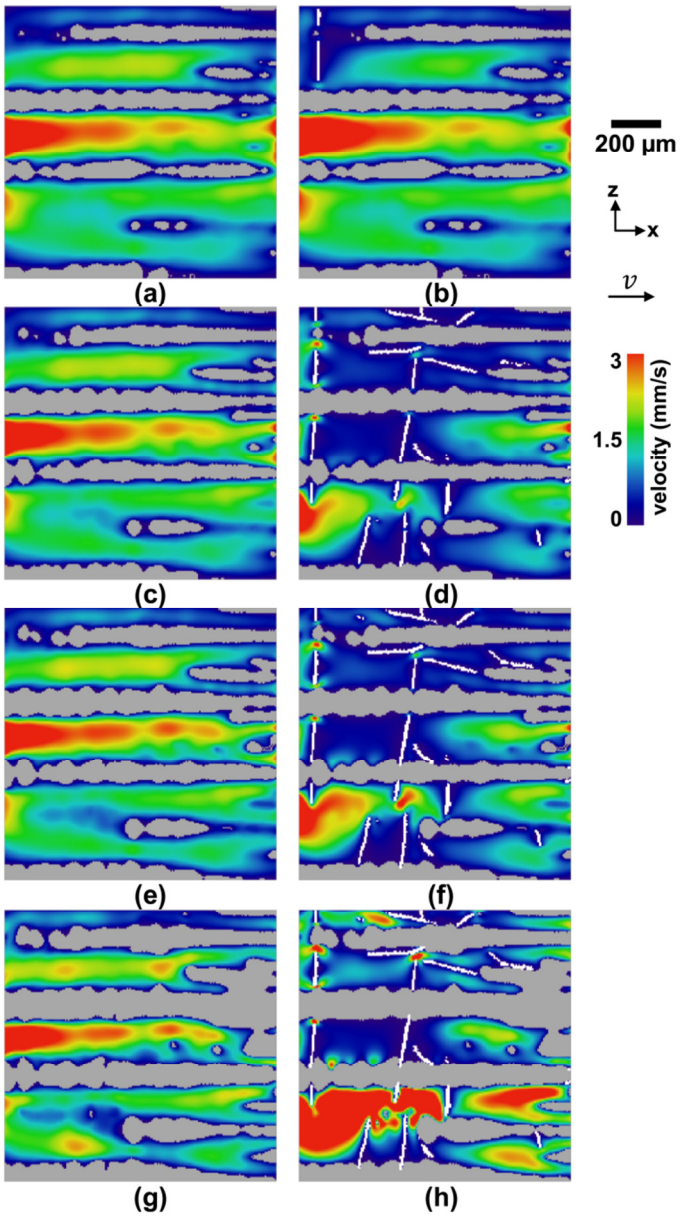


Figure 4.7 2-D cross-sectional views of the calculated 3-D velocity magnitudes showing the fluid flow within the interdendritic region during solidification both (a,c,e,g) without, and (b,d,f,h) with β-intermetallics at solid fraction of (a,b) 0.30 (578±1°C), (c,d) 0.36 (572±1°C), (e,f) 0.41 (565±1°C), and (g,h) 0.56 (561±1°C). The primary Al-rich dendrites and eutectic are coloured in grey while the β-intermetallics are white.

Beginning with Figure 4.7a-b at f_S=0.30, it can be seen that the addition of one β-intermetallic particle partially blocks the top channel (Figure 4.7b, upper left-side plate in white). With increasing solid fraction (i.e. Figure 4.7c-d at f_S=0.36, Figure 4.7e-f at f_S=0.41, and Figure 4.7g-h at f_S=0.56), the flow fields become more complex. For example, at f_S=0.41 (Figure 4.7e-f), the flow has transitioned from a relatively constant

velocity without β-intermetallics (Figure 4.7e) to a velocity field that is channel-dependent, with blockages, and sudden jumps in velocity with the presence of the β-Al_5FeSi intermetallics (Figure 4.7f). Note that while it may appear from these flow patterns that mass is not conserved, this is not the case as these images are 2-D cross-sections of 3-D simulations. Liquid that is blocked in plane will circulate out of plane.

From a qualitative perspective, the results shown in Figures 4.6 and 4.7 demonstrate that Fe-containing β-intermetallics strongly block the interdendritic channels at high solid fractions. Iron impurities are known to increase porosity content and hot tearing. These simulations verify that channel blockage, as previously theorised [82, 86, 120], is indeed one of the causes of increased pore and hot tearing defect formations. Note that these results do not disprove the other postulated mechanisms; rather, they clearly highlight and quantify the importance of flow effects.

4.4 Permeability assessment

The permeability values extracted from the flow simulations are shown in Figure 4.8, for flow (a) parallel and (b) normal to the primary columnar dendrites both without and with β-intermetallics as a function of temperature. The evolution in solid fraction as measured from the tomographic datasets is also provided, including the points for β-intermetallic and eutectic formation. Beginning with Figure 4.8a, it can be seen that the permeability decreases monotonically with temperature as expected because of the thickening of the primary dendrites as solidification progresses. The permeability is significantly lower for the case with β-intermetallics as compared to without, although the trends are the same.

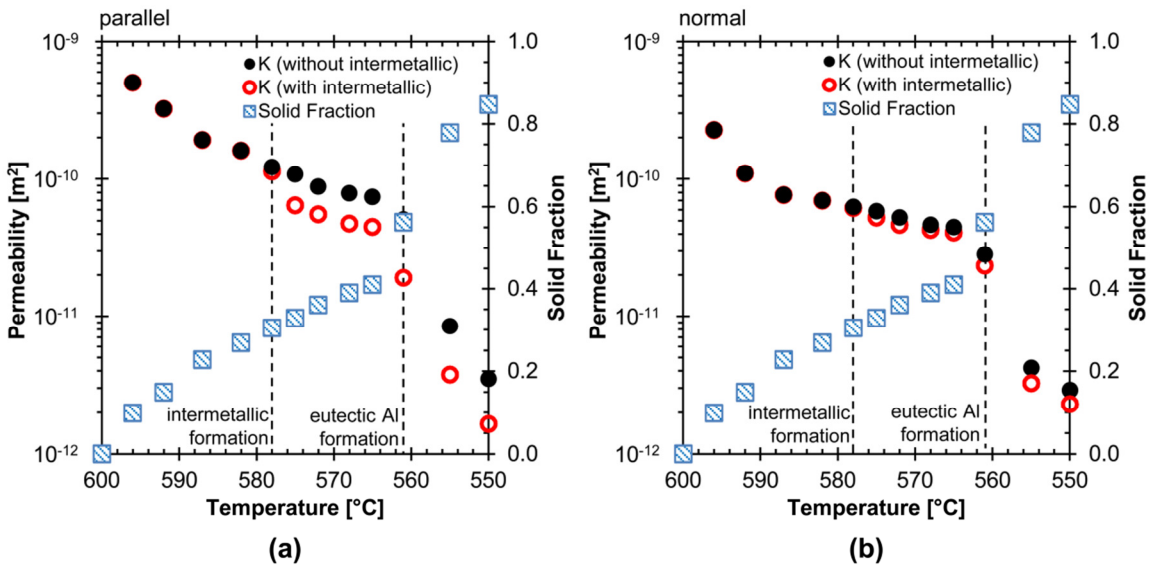


Figure 4.8 The evolution in permeability for liquid flow (a) parallel and (b) normal to the primary columnar dendrites both without and with β-intermetallics. Dashed-lines indicated the temperatures where the nucleation of β-intermetallic and eutectic Al phases were observed in the 3-D renderings.

In the solidification interval between β-intermetallic and eutectic formation, the loss of permeability that occurs due to the β-intermetallic particles can be directly attributed to the blocking effect discussed in the previous section. Once the eutectic starts to form, the channels become further blocked and small side-branches close completely, resulting in a further permeability decrease as compared to the standard value without β-intermetallics. The effect of β-intermetallics on the calculated permeability values normal to the primary dendrites, shown Figure 4.8b, show similar trends to those discussed for the parallel flow in Figure 4.8a. However, the additional loss in permeability related to the β-intermetallic particles is considerably lessened. As shown in Figure 4.2, the primary channels in the x-direction are large and continuous while the channels in the y- and z-directions are already discontinuous, impeding flow. Hence, the addition of β-intermetallic particles does not increase the channel tortuosity in the normal direction to any great extent.

The results shown in Figure 4.8 are unique in that they quantify, for the first time, the variation in permeability with solid fraction on the *same* specimen. These

results were made possible due to the *in situ* acquisition of the tomographic datasets. As reviewed in section 2.3.2, other researchers [106-110] have performed similar simulations on a series of specimens quenched at various intervals within the semi-solid regime to achieve a primary phase fraction matching a specific solid fraction. This previous work provided good insight into permeability development but each specimen had a different microstructure and hence provided considerable scatter in the numerical results. With the exception of [109], this previous work was performed on grain-refined alloys with equiaxed globular grains. Permeability in globular structures will be considerably different in comparison to dendritic structures since there is no well-defined primary channel to drive fluid flow, and further, blocking by β-intermetallics may be inter-granular and hence more irregular. These results, therefore, stand alone in characterising permeability with regards to columnar dendritic microstructures.

Figure 4.9 shows a simulation of interdendritic liquid flow around an actual β-intermetallic particle. In Figure 4.9a, the flow is vertical and down, and hence parallel to the platelet's orientation, while in Figure 4.9b the flow is horizontal and to the right, and hence normal to the platelet. It can be observed that the disturbance around the normal platelet is considerable and thus will significantly affect permeability while the corresponding disturbance around the parallel platelet is minimal. Based on this simple flow field visualisation, it is clear that any permeability assessment involving a channel blocking mechanism must include knowledge of the shape and orientation of the blocking particles. In our solidification sequence, the orientation of the β-intermetallics in relation to the primary dendrites fits a normal distribution representation with μ=90° and σ=35.5. As shown in Chapter 3, β-intermetallics have a preferential growth direction that is parallel to the secondary dendrite arms and hence perpendicular to the primary trunk, which, based on Figure 4.9, would increase their blocking efficiency.

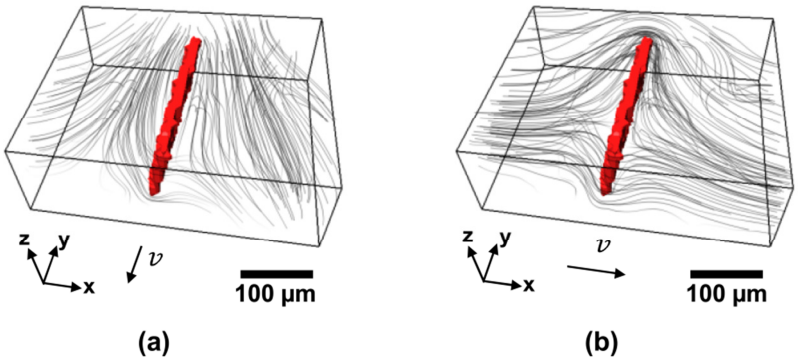


Figure 4.9 Simulated flow velocities in a sub-volume of interdendritic liquid extracted from the volume shown in Figure 4.7h for flow (a) parallel and (b) normal to the orientation of the β-intermetallic particles. Note the direction of v in each image showing the fluid flow.

4.5 Determination of an analytical permeability expression

The flow simulations presented above enable introduction of the influence of β-intermetallics on analytical expressions for semi-solid permeability. In this work, the calculated values of permeability have been fit to an empirical relationship based on the Blake-Kozeny equation following the procedure of Poirier [94] (see section 2.3.2). An additional term, $1-\beta f_I$, where β represents the impact factor of the β-intermetallics on flow blockage, has been added to account for the effect of f_I as shown below:

$$K_p = (1-\beta f_I)K_p^{orig} \tag{4.3}$$

$$K_n = (1-\beta f_I)K_n^{orig} \tag{4.4}$$

$$K_p^{orig} = C_1 \frac{f_L^3 \lambda_1^2}{1-f_L} \tag{4.5}$$

$$K_n^{orig} = C_2 \left(\frac{\lambda_1}{\lambda_2}\right)^p \frac{f_L^3 \lambda_1^2}{(1-f_L)^n} \tag{4.6}$$

where K_p and K_n are the permeabilities in the directions parallel and normal to the primary dendrites, K_p^{orig} and K_n^{orig} are the original expressions of Poirier [94], λ_1 and λ_2

are the primary and secondary dendrite arm spacings, f_L is the liquid fraction and C_1, C_2, p, n are fitting constants calculated from the regression analysis. For the case without β-intermetallics, f_I is 0, reducing Equations (4.3) and (4.4) to the general anisotropic Blake-Kozeny permeability expressions. The value of β, along with the fitting constants C_1, C_2, p, n, is summarised in Table 4.1. These values were obtained via a nonlinear least-squares regression analysis of the simulated permeability results taking into account only the values that did not contain eutectic Al-Si. The constants obtained by Poirier are also provided in Table 4.1 for comparison purposes. Note that while the values of f_I were obtained directly from the tomographic datasets, data from thermodynamic calculations could be utilised for implementation of Equations (4.3) and (4.4) into casting models for predicting defects.

Table 4.1 Parameters for Blake-Kozeny permeability expressions

Parameter	Model	
	This study	Poirier [94]
Parallel flow [eq. (4.3)]		
C_1	8.5×10^{-4}	$4.53 \times 10^{-4} + 4 \times 10^{-6}(f_L + 0.1)^{-5}$
β	15	N/A
Normal flow [eq. (4.4)]		
C_2	4×10^{-3}	1.73×10^{-3}
p	1	1.09
n	0.3	0.749
β	10	N/A

The comparison between the simulated permeability results and the analytical expressions based on Equations (4.3) and (4.4) is shown in Figure 4.10. It can be seen that the fits in both the (a) parallel and the (b) normal directions are excellent at f_L>0.4, i.e., in the regime of primary phase solidification. Thus, the permeability of columnar dendritic microstructure with intermetallics is shown to be predictable by adding an impact factor to the Blake-Kozeny expressions. The value of β is observed to be larger

in the case of flow in the parallel direction ($\beta = 15$) in comparison to the normal direction ($\beta = 10$). As shown earlier in Figure 4.9, greater impact on the flow fields can be found when plate-like β-intermetallic particles grow normal to flow direction. It would then be expected that blocking particles with less complexity (e.g., globular shape) would have smaller β factor.

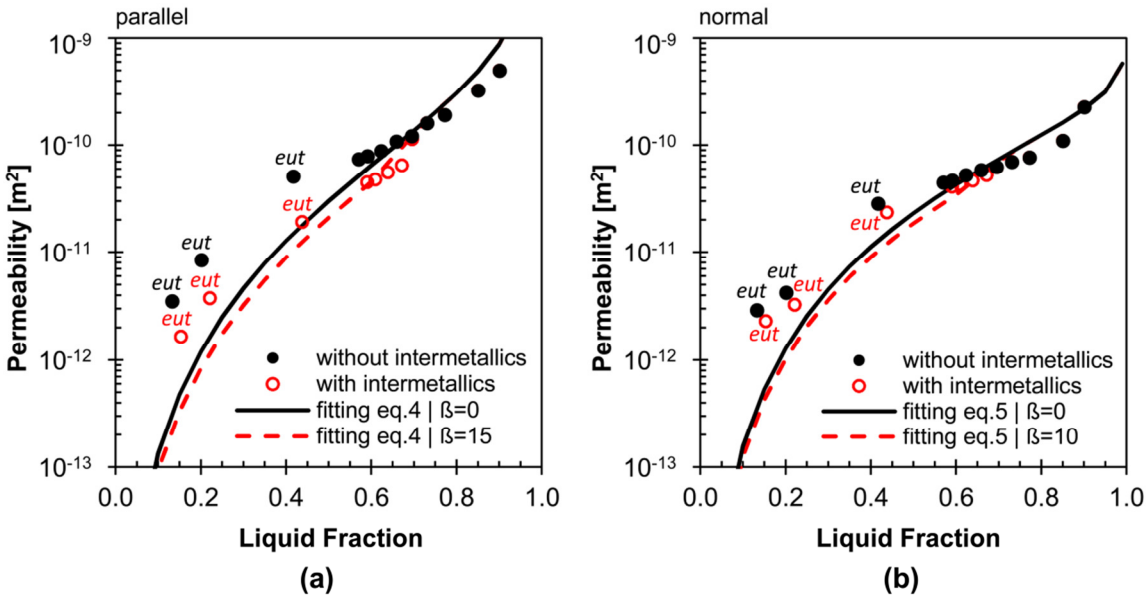


Figure 4.10 Comparison between the simulated permeability and the regression fitting, Equations (4.3) and (4.4), for liquid flow both (a) parallel and (b) normal to the primary columnar dendrites in solidifying microstructures both with and without β-intermetallics. Note that the annotated *eut* indicates a structure containing eutectic material.

For values of f_L<0.4, the new analytical expression for permeability deviates from the simulation results. At this point, the eutectic reaction has commenced, and this will strongly affect channel blockage as the eutectic Al-Si may form alongside primary Al-rich dendrites [188] and/or may cause complete closure of small side-branch channels (e.g. Figure 4.7e and Figure 4.7g) and/or may cause the formation of preferential flow paths. The deviation may also be due to the relative effects of intermetallic formation and eutectic formation on channel tortuosity, which could be significantly increased in these cases.

The analytical permeability expressions were originally derived based on dendritic microstructures and while the presence of eutectic will increase the solid fraction, it will not necessarily increase tortuosity (i.e. Equations (4.5) and (4.6) may not apply in the case of columnar dendritic structures with a large eutectic fraction). This corresponds to the finding of Khajeh and Maijer [108] that, for large values of θ[1], the total permeability is controlled only by the permeability of the dendritic network. In contrast, the channel blocking mechanism resulting from β-intermetallic formation will definitely increase tortuosity in both parallel and normal flows. Further study of the impact of eutectic formation on fluid flow is thus required in order to include this aspect of the problem into an analytical expression for permeability containing both β-intermetallics and a significant eutectic constituent.

4.6 Comparison with experimental data and analytical approximations

Murakami *et al.* [100, 101] using borneol-paraffin and Poirier [94] using Pb-Sn have measured the permeability for different values of λ_1, λ_2 and f_L for flow both parallel to and normal to the primary dendrite direction. These experimental results, together with the analytic Hagen-Poiseuille (Santos *et al.* [117]), and Blake-Kozeny (both this work and Poirier [94]) expressions are compared in Figure 4.11 against the permeability values extracted from the present flow simulations. In order to put all of the results on the same figure, a dimensionless form of permeability is adopted. This figure shows that the flow simulations match reasonably well with the experimental

[1] The dimensionless θ is defined in [108] as $\theta = \frac{f_{L,e}\, D_e}{7.75(1-f_{L,e})}\sqrt{\frac{f_{L,d}}{K_d}}$ where $f_{L,e}$ and $f_{L,d}$ are the fraction of eutectic solid and dendritic solid, K_d is the permeability assuming on a dendritic structure and D_e is the density of equiaxed grains. In columnar dendritic structures, $D_e \to 0$ and thus $\theta \to \infty$.

data for both parallel and normal flow regimes. Regarding the analytical expressions, while the expressions also match reasonably well to the flow simulations without β-intermetallic particles, the best fit is obtained with the anisotropic Blake-Kozeny model using the constants derived in this work because this expression illustrates good agreement for both parallel and normal flow regimes. Although the differences between the permeability values using Poirier's constants and the constants derived in this work are small, especially in the case of normal flow, a significantly better fit is found at higher liquid fractions. This is because Poirier had only experimental data at f_L<0.6 with which to perform the regression analysis whereas tomographic datasets with 0.6<f_L<0.9 were available in this work.

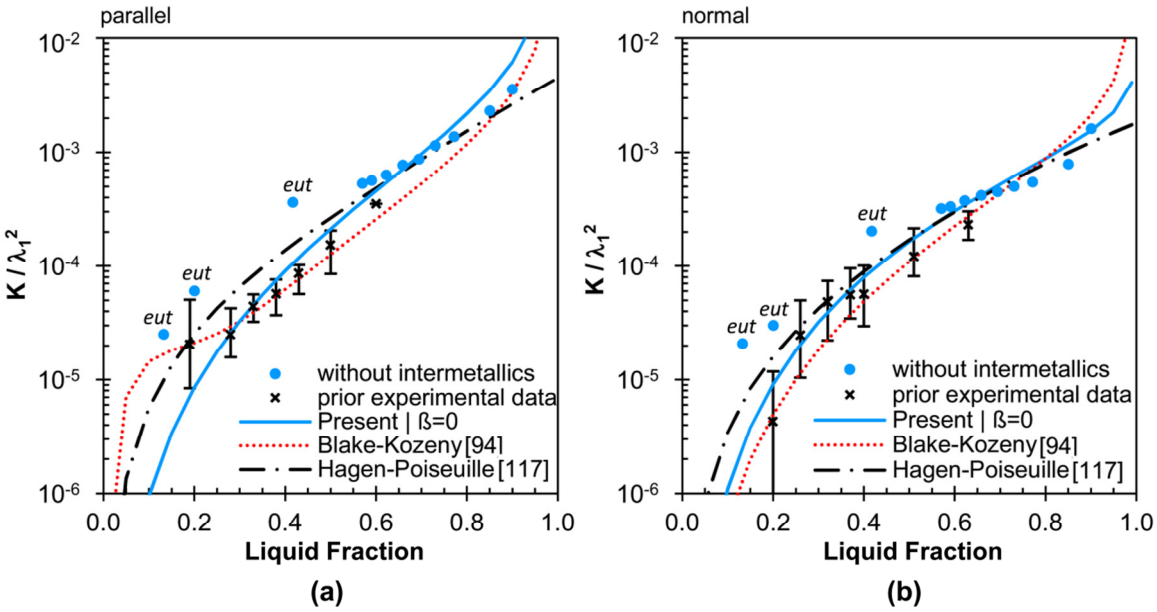


Figure 4.11 Comparison between the simulated permeability in solidifying microstructures both with and without β-intermetallics, analytical models (curves) [94, 117, and present work], and experimental data from Pb-Sn and borneol-paraffin alloys (crosses) [94, 100, 101] in units of dimensionless permeability for flow both (a) parallel and (b) normal to the primary columnar dendrites. Note that the annotated *eut* indicates a structure containing eutectic material.

4.7 Summary

A *novel* method for coupling *in situ* synchrotron x-ray tomography with numerical simulations was developed to quantify the permeability of solidifying microstructures. This new technique captured, *in situ* and in 3-D, multiple solid fractions ($0.1<f_s<0.85$) of an Al-Si-Cu alloy during solidification. With such information, the development of multiple phases (primary, β-intermetallics, and eutectic) and accurate measurements of the permeability and fluid flow of the evolving specimen were possible for the first time. The results qualitatively and quantitatively demonstrate the blocking effect of β-intermetallics on fluid flow and the ensuing loss in permeability, particularly in the direction parallel to the primary dendrites. The results also show that the β-Al_5FeSi intermetallic precipitates reduce the permeability of the semi-solid metal.

This first direct quantification of permeability was then encapsulated in an analytical expression based on the anisotropic Blake-Kozeny relation which can be easily incorporated macroscopic flow simulations of defect formations during solidification processes. This new expression includes an additional term, $1-\beta f_I$, to characterise the effect of the β-intermetallics. A good fit for parallel and normal flows to both the simulation results and experimental data from the literature is found when using this new expression. This factor takes into account the dependency of morphology and orientation of blocking particles.

The following chapter will demonstrate the contribution of β-intermetallics on flow blockage and permeability reduction that leads to the increased susceptibility of alloys for solidification defects such as hot tearing and microporosity.

Chapter 5

Influence of β-intermetallics on solidification defects*

The previous work in Chapter 4 has shown significant influence of β-Al_5FeSi intermetallics on flow blockage and permeability reduction. This impact on feeding behaviour reflects the negative effects of β-intermetallics on an alloy's castability. As reviewed in Chapter 2, prior experimental studies have found that the presence of β-intermetallics increases the propensity of solidification defect formation, such as an increase in porosity content [8, 47, 78, 131]. Many mechanisms by which β-intermetallics affect pore formation have been suggested (detailed in section 2.4.1), including blocking of interdendritic flow [8, 120], acting as nucleation sites [132], and aiding pore growth [11]. They may also influence pore growth indirectly, for example inducing larger Al-Si eutectic grains that reduce feeding and thus increase porosity [133]. However, there has been no consensus on the choice of dominant mechanism due to most studies being only a post-mortem analysis.

* Note, this chapter has been submitted in modified form to Acta Materialia as the paper entitled "Influence of Fe-rich intermetallics on solidification defects in aluminium-silicon-copper alloys" by Puncreobutr, C., Lee, P.D., Kareh, K.M., Connolley, T., Fife, J.L., Phillion, A.B.

In addition to as-cast porosity, A319 alloys containing β-intermetallics also exhibit a high susceptibility to hot tearing [7, 160], another solidification defect that limits production yield during the casting and processing of recycled aluminium. As detailed in section 2.4.2, while an extensive number of experimental and numerical investigations have been made on binary alloys to relate various alloying and processing parameters to hot tearing susceptibility [139, 140, 142, 145], little is known about hot tearing in commercial Al-Si-Cu alloys, and even less about the influence of β-intermetallics. Although a few studies have shown that the addition of Sr and/or TiB_2 can have a beneficial effect in reducing the hot tearing susceptibility of A319 alloys [7, 160], the role of β-intermetallics on hot tear formation has not been directly examined, and the correlation between alloying elements that modify microstructure and a reduction in the hot tearing is still unclear.

Direct observation of defect formation during solidification has recently been made possible both in 2-D, via x-ray radiography, and in 3-D, via x-ray tomography, yielding better insights into real-time pore formation [23, 189] and hot tear processes [92, 190] in binary Al-Cu alloys.

In this chapter, fast *in situ* synchrotron x-ray tomographic experiments were performed on commercial A319 alloys (Al-7.5Si-3.5Cu, wt.%) with differing Fe-levels (0.2-0.6wt%Fe). Real-time observations of porosity and hot tear formation were made during both *in situ* solidification and semi-solid uniaxial tension experiments to provide a greater understanding of the influence of β-intermetallics on defect formation in the semi-solid state.

The chapter will first present the details of the experimental procedure and quantitative image analysis techniques used in this study. It will then explore the effect of β-intermetallics on both porosity formation and hot tear susceptibility.

5.1 Methods

5.1.1 Materials

To perform solidification and semi-solid deformation experiments, A319 alloys (Al-7.5Si-3.5Cu, wt.%) with two different Fe-levels (0.2-0.6Fe, wt.%) were prepared from a commercial A319 ingot (as-received from Ford Motor Company) and a commercially pure Al-10Fe (wt.%) master alloy. These metals were melted and cast into a pre-heated well-feed permanent mould [161] to form a wedge-shaped specimen, using the same procedure given in section 3.1.1. The resulting microstructure was equiaxed dendritic. The chemical compositions obtained using x-ray fluorescence are given in Table 5.1.

Table 5.1 Chemical composition of A319 alloys (wt.%)

A319	Al	Si	Cu	Fe	Mn	Mg	Ti	Zn
0.2Fe	balance	7.49	3.40	0.15	<0.01	0.07	0.08	<0.01
0.6Fe	balance	7.52	3.53	0.59	<0.01	0.07	0.07	0.01

The solid fraction of intermetallics f_I for these two alloy compositions is plotted in Figure 5.1 using a Scheil approximation within the Thermo-Calc software (Thermo-Calc Software AB, Stockholm) and the database from [62]. The thermodynamic calculation predicts a three-fold increase in β-intermetallic phase fraction, from ~0.65% to nearly 2.1% as the Fe content is increased from 0.2wt.%Fe to 0.6wt.%Fe. Longitudinal sections of the as-cast microstructure from the high-resolution tomographic images (0.9μm), described in section 5.1.3, for both wedge castings are also shown in Figure 5.1. As can be seen, the plate-like β-intermetallics can only be resolved in the specimen with 0.6wt.%Fe. At 0.2wt.%Fe, and under the cooling rates given by the wedge casting setup, the β-intermetallic phase cannot be observed with the

given resolution. Thus, the 0.2wt.%Fe alloy corresponds to a primary-grade material while the 0.6wt.%Fe alloy corresponds to a recycled-grade product.

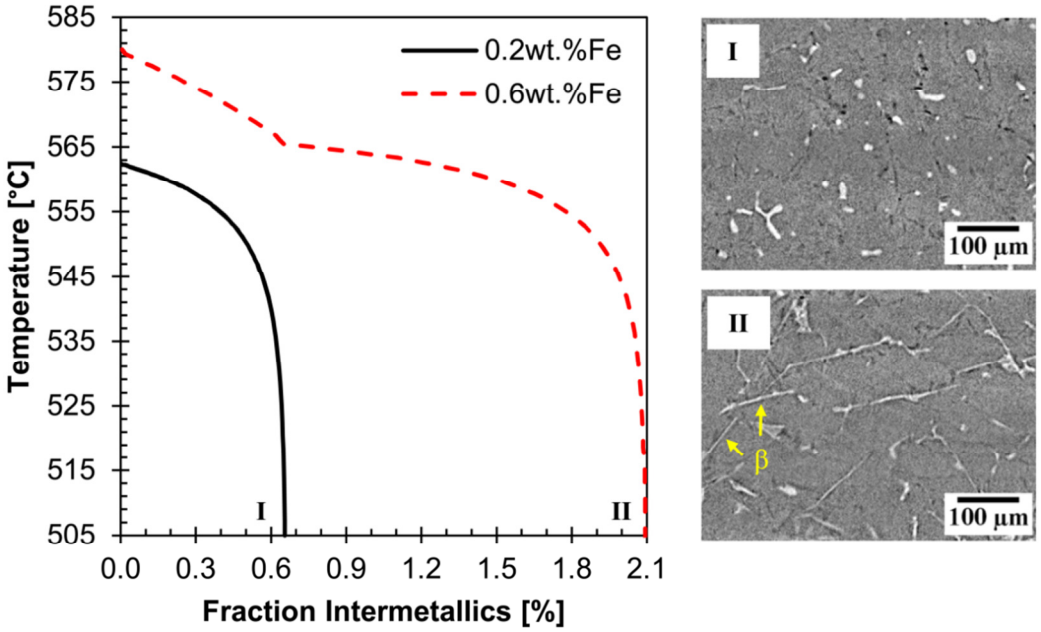


Figure 5.1 Calculated fraction of the *β*-intermetallics in Al-A319 alloys at two Fe-levels of (I) 0.2 wt.%Fe and (II) 0.6 wt.%Fe, assuming Scheil solidification model. (I) and (II) show high-resolution longitudinal sections of typical as-cast solidified microstructures.

Subsequent to the wedge-casting, a tensile specimen was extracted from the wedge with 0.2wt.%Fe for the *in situ* semi-solid deformation experiment, and both a cylindrical specimen and a tensile specimen were machined from the wedge with 0.6wt.%Fe for the *in situ* solidification and semi-solid deformation experiments. The dimensions of the tensile specimens were 60 mm in length and 3 mm in diameter, with a small central gauge notched section of 5.5 mm in length and 2.5 mm in diameter. The cylindrical specimen was 4 mm in length and 2.5 mm in diameter.

5.1.2 Solidification experiment

To investigate the interaction between *β*-intermetallics and porosity formation, the results obtained from the first *in situ* solidification experiment in Chapter 3 are further analysed in this chapter. As fully described in section 0, the experiment was carried out on the 0.6wt.%Fe specimen at TOMCAT beamline of the Swiss Light Source

(Paul Scherrer Institut, Switzerland), using a bespoke resistance furnace (shown in Figure 5.2a). The specimen was first heated up to 650°C, held for 5 minutes to ensure it was completely molten and isothermal, and then cooled at a rate of 0.05°C/s until completely solid. During solidification, the specimen was continuously rotated and parallel polychromatic x-ray radiation, filtered to 5% power (~30keV), was used to acquire a series of 2-D radiographs at different angles that were then processed to reconstruct 3-D tomographic volumes with a pixel size of 2.75 μm. Each complete 3-D volume consisted of 1001 radiographs and was captured in 2s, minimising the dynamic change in the solidifying microstructure during each scan. There was a delay of ~1 minute to download all radiographic images off the camera memory for the next 3-D scan, resulting in a total scan time of 72s between consecutive 3-D volumes.

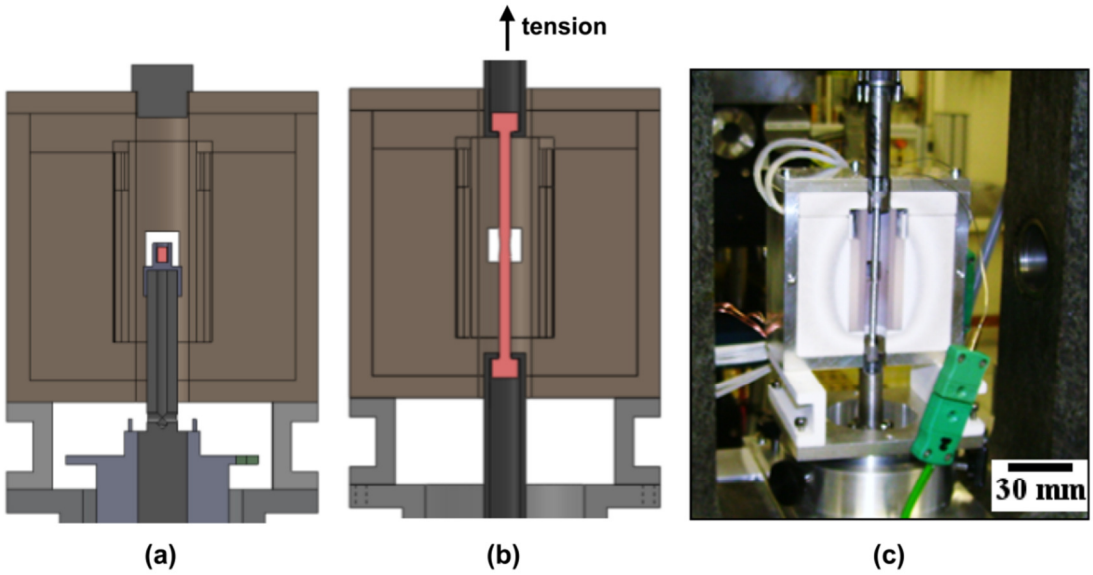


Figure 5.2 (a-b) Schematics of experimental setups for solidification and semi-solid uniaxial tension studies, respectively; and (c) photograph of thermal-mechanical testing rig.

5.1.3 Semi-solid deformation experiment

To study the behaviour of semi-solid A319 alloys during tensile deformation the resistance furnace used for the solidification experiment was integrated with a bespoke mechanical tester rig, called P2R, shown in Figure 5.2b-c. This apparatus was designed and constructed with the following technical specifications [173]: (1) load application of

±1-500 N, (2) specimen extension of ±0-150 mm with an encoded accuracy of 200 nm, and (3) stepped or continuous specimen rotation over ±0-360° within an accuracy of 0.001° at speeds up to 1Hz.

The two *in situ* tensile deformation experiments were performed on the 0.2wt.%Fe and 0.6wt.%Fe specimens at the I12 beamline of the Diamond Light Source (Harwell Science and Innovation Campus, UK). In these tests, each specimen was heated up to 515˚C and held for 5 minutes to enable thermal equilibrium. This temperature is approximately 10°C above the eutectic temperature of 505°C and corresponds to a solid fraction (f_S) of 0.92 in the notched region. Then, each specimen was deformed until failure under uniaxial tension at a constant cross-head displacement rate of 10 μm/s, corresponding to an average axial stain rate of ~$5x10^{-3}$ s^{-1}. During deformation, the specimen was continuously rotated and monochromatic x-ray radiation of 53 keV was used to acquire a series of 2-D radiographs at different angles that were then processed to reconstruct a series of 3-D tomographic volumes with a pixel size of 12.22 μm. Each 3-D volume was captured using 720 radiographs in 4s. In total, 24 volumes were acquired for each deformation test specimen from the undeformed to the final failure stages with a 4s downtime between consecutive 3-D volumes.

After the final failure, a high-resolution synchrotron x-ray tomography at a pixel size of 0.9 μm was performed on the upper half of each failed specimen (which was clamped in the moving jaw (Figure 5.2b)) to further investigate the fracture surface and internal voids in 3-D.

5.1.4 Quantitative characterisation

A fast reconstruction algorithm based on the Fourier transform method (gridrec) [165, 166] was used to obtain the 3-D solidification datasets, while an algorithm based

on the filtered back projection (FBP) method [191-193] was used to obtain the 3-D semi-solid deformation datasets. Full details of reconstruction procedure were given in section 3.1.3. Different algorithms were used as each beamline has its own process for reconstruction of the tomographic images. Although significant differences in computational performance can be found, the reconstructed 3-D results obtained from gridrec and FBP are almost equivalent [165]. In both cases, a flat-field correction, a dark-field correction and ring artifact removal algorithms [167, 191] were performed prior to reconstruction. For each experiment, the series of 3-D volumes were then spatially aligned using a 3-D affine registration method [168], and then a 3-D non-linear diffusion filter [171] was applied to reduce noise. Finally, two binarisation methods were used to separate each phase: region growing segmentation [172] was used to obtain pores and hot tears whereas manual segmentation was done to obtain β-intermetallic phase.

For the solidification experiment, the quantification of pore and intermetallic phases was made in a sub-volume of 400x400x400 voxel^3 (equivalent to ~1 mm^3) extracted from a region near the specimen surface to focus on the evolution of a single pore and its interaction with the surrounding β-intermetallics. For the semi-solid deformation experiments, the quantification was made in the gauge region of the specimens. The volume analysed in the gauge was kept constant and hence was elongated proportional to the strain undergone by the specimen from the undeformed state to failure. Two types of pores/voids were defined in the gauge: internal (if the pore/void had no connectivity to the specimen surface) or surface-connected.

Similar to techniques detailed in section 3.1.6, the volume and orientation of each pore/void and each intermetallic was calculated using a marching cube triangulation method and principle component analysis (PCA) respectively. These calculations were performed using MATLAB (MathWorks, MA). An advanced rendering

package (Avizo (VSG, France)) was used to produce the visualisations of all 3-D structures. Note that in this chapter the term "pores" is used for those formed due to solidification shrinkage/feeding, the term "voids" is used for those occurred during straining, and "damage" is used for the combined regions.

5.2 Effect of β-intermetallics on porosity formation

The evolution of a selected (typical) pore in the Al-Si-Cu alloy with 0.6wt.%Fe during the solidification experiment is examined in Figure 5.3. The 3-D rendering of the pore with decreasing temperature is shown in Figure 5.3a, and the corresponding evolution in pore volume and sphericity is quantified in Figure 5.3b.

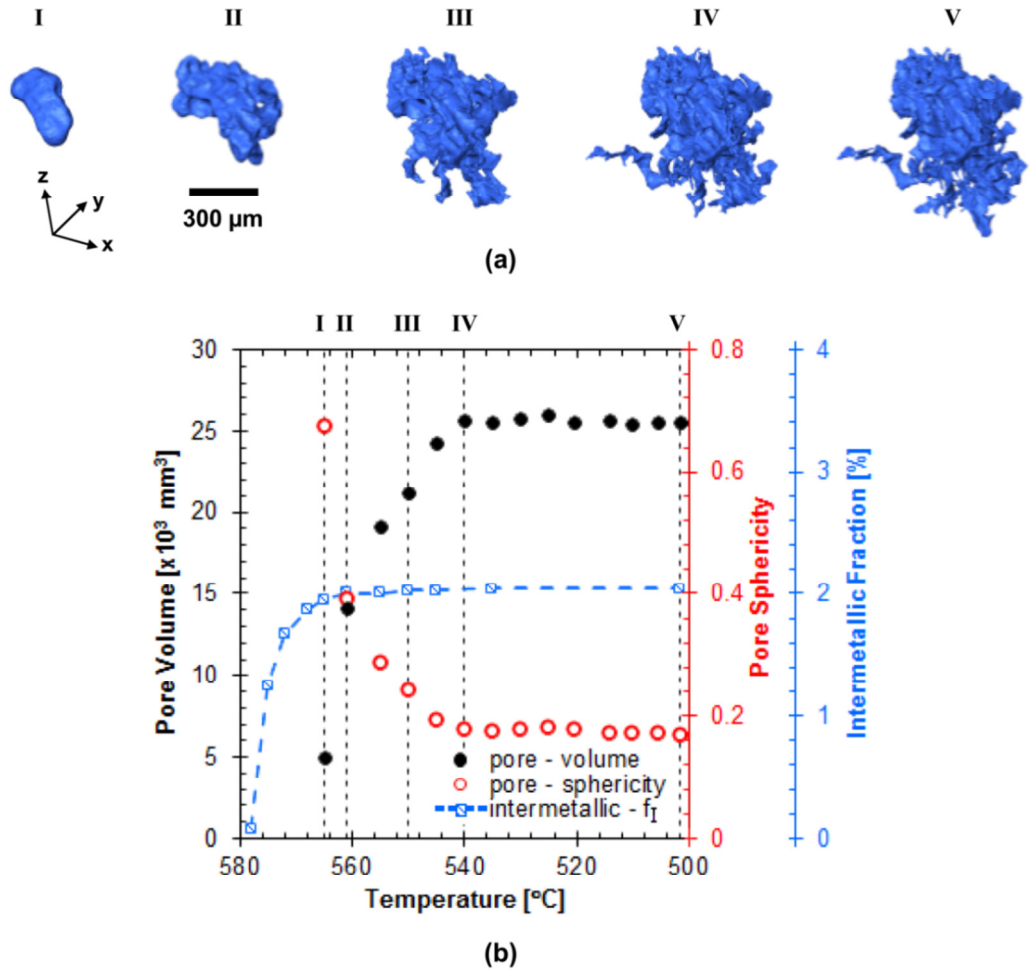


Figure 5.3 (a) Rendered evolution of a pore during solidification (I-V represent temperatures of 565°C, 561°C, 550°C, 540°C and 502°C, respectively); (b) quantified volume and sphericity of the pore shown in (a). Quantified fraction of intermetallics is also illustrated.

The pore first appears at 565±1°C, and is small and round (Figure 5.3a-I). As the temperature decreases to 561±1°C (Figure 5.3a-II), the pore grows very rapidly, tripling its volume from its initial $5x10^3$ mm^3 (plotted in black in Figure 5.3b). This trend continues with advancing solidification (Figure 5.3a-III,IV), where both pore size and tortuosity are observed to increase. Pore formation is almost complete at 540±1°C when the pore reaches a volume of ~$26x10^3$ mm^3 (Figure 5.3a-V). At lower temperatures, the pore volume remains constant, as shown by the plateau in Figure 5.3b. The quantified sphericity of the pore, which is a measure of its roundness (where the sphericity of a sphere equals 1), decreases dramatically from ~0.7 when it first forms to less than 0.2 after 540±1°C, and remains unchanged thereafter (red plot in Figure 5.3b).

The observed evolution in β-intermetallics is also plotted in Figure 5.3b (blue curve) for comparison purposes. β-intermetallics are observed to form between 578±1 and 565±1°C, i.e. their formation is mostly complete when the observed pore nucleates at 565±1°C. Plate-like β-intermetallics are thus already present at the moment of pore nucleation.

To clarify the role of β-intermetallics on pore nucleation and growth, the interaction between the selected pore and its surrounding intermetallics during solidification is rendered in 3-D in Figure 5.4. As can be seen, the pore (blue) first forms inside a liquid channel, which is surrounded by β-intermetallics (red). As previously seen in Chapter 4, these β-intermetallics can physically block interdendritic flow, reducing permeability. It has also been hypothesised they block hydrogen diffusion paths in the interdendritic liquid by acting as diffusion barriers, which imposes hydrogen supersaturation in local subdivided domains and induces pore nucleation [11]. This hypothesise and simulated results obtained in previous chapter agree well with Figure 5.4, where the liquid channel will be supersaturated with hydrogen with a lower permeability due to the number of β-intermetallics surrounding it.

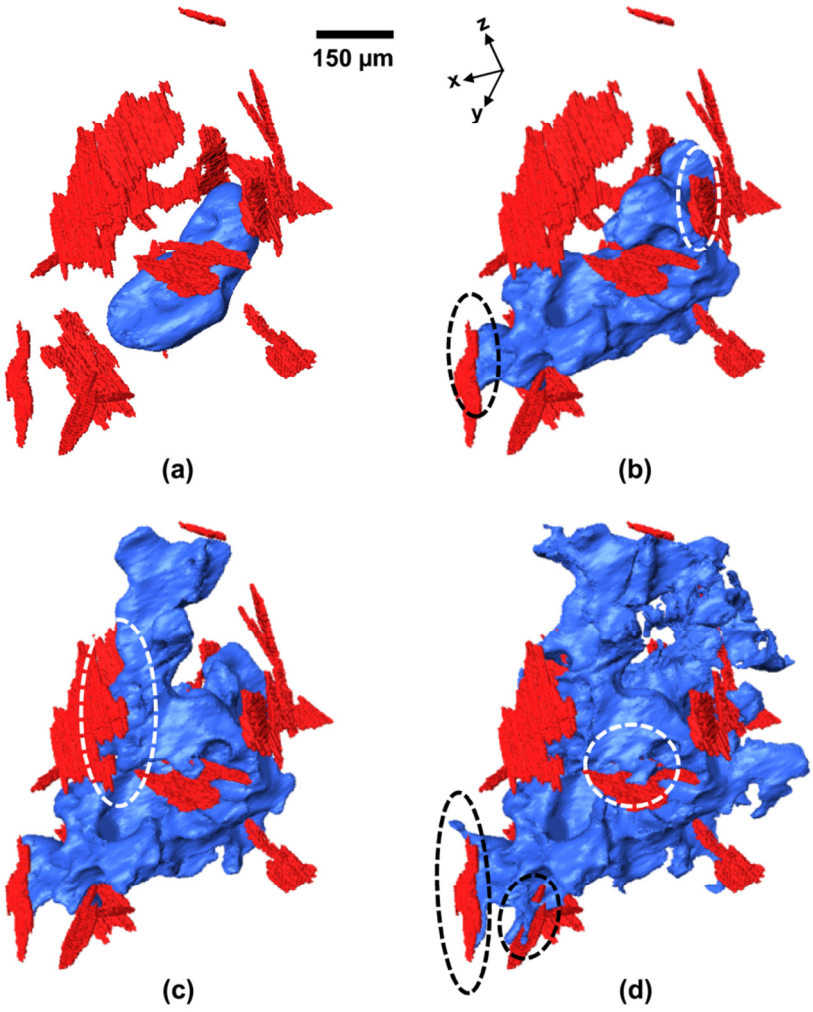


Figure 5.4 Rendering of pore evolution (blue) with the presence of intermetallics (red) (a-d represent temperatures of 565°C, 561°C, 555°C and 550°C, respectively). Examples of pore growth along solid surface of intermetallics are shown in dashed-circles.

After nucleation, the pore grows very rapidly into the interdendritic regions with an increasing tortuosity as shown in Figure 5.4b-d. The growth of the pore is physically constrained by both β-intermetallics and other solid phases, i.e. the primary dendrites and the Al-Si eutectic (which starts nucleating at 561±1°C). Similar behaviour of pore growth constrained by the solid phases was previously observed radiographically [23] and tomographically [194]. The pore also appears to grow preferentially along the solid surface of the β-intermetallic plates as illustrated in the dashed-circles in Figure 5.4b,c. As hypothesised in [11], Fe-rich intermetallics may thus reduce the gas-intermetallic interfacial energy and facilitate growth along intermetallic surfaces. The pore can also

grow into the small spaces between the β-intermetallics and the other solid phases as shown by the bottom left circle in Figure 5.4d.

Unlike prior work involving quenched microstructure observations (e.g. [132]), there was no evidence of pore nucleation on β-intermetallics in the tomographic images shown in Figure 5.4. The results of this *in situ* solidification experiment instead suggest that β-intermetallics induce pore nucleation by blocking the feeding of liquid, thus reducing permeability (as demonstrated in Chapter 4), and accelerating pore growth through the reduction of the pore-intermetallic interfacial energy. The quantitative characterisation is, however, limited to one example under specific cooling conditions, and further investigations are needed to confirm the predominance of this mechanism. The *in situ* observation of preferential pore growth along the planar surfaces of β-intermetallics shown in Figure 5.4 may also explain why prior authors have frequently found pores in contact with β-intermetallics in classical quenched microstructure (e.g. [47, 132, 136]); pores appear to nucleate in the interdendritic liquid and/or off the aluminium dendrites and then later grow towards and make contact with surrounding β-intermetallics.

5.3 Effect of β-intermetallics on hot tear formation

5.3.1 *In situ* observation

Longitudinal sections in Figure 5.5 show the evolution of damage with increasing strain for both 0.2wt%Fe and 0.6wt.%Fe Al-Si-Cu specimens in semi-solid uniaxial tension. The images a-d (e-h) show the evolving structure of the 0.2wt%Fe (0.6wt%Fe) specimen between a 0-19% (0-7%) strain. As can be seen, the attenuation contrast is sufficient to allow for the quantification of damage formation in the complex dendritic microstructure, where the damages appear as dark regions, equiaxed

aluminium grains appear grey, and the liquid and intermetallic phases (including β-Al_5FeSi and Al_2Cu) appear white. Although the spatial resolution of 12.22 μm used in this *in situ* study is sufficient to quantify damage formation in the entire specimen gauge length, the β-intermetallics are too fine for quantitative analysis.

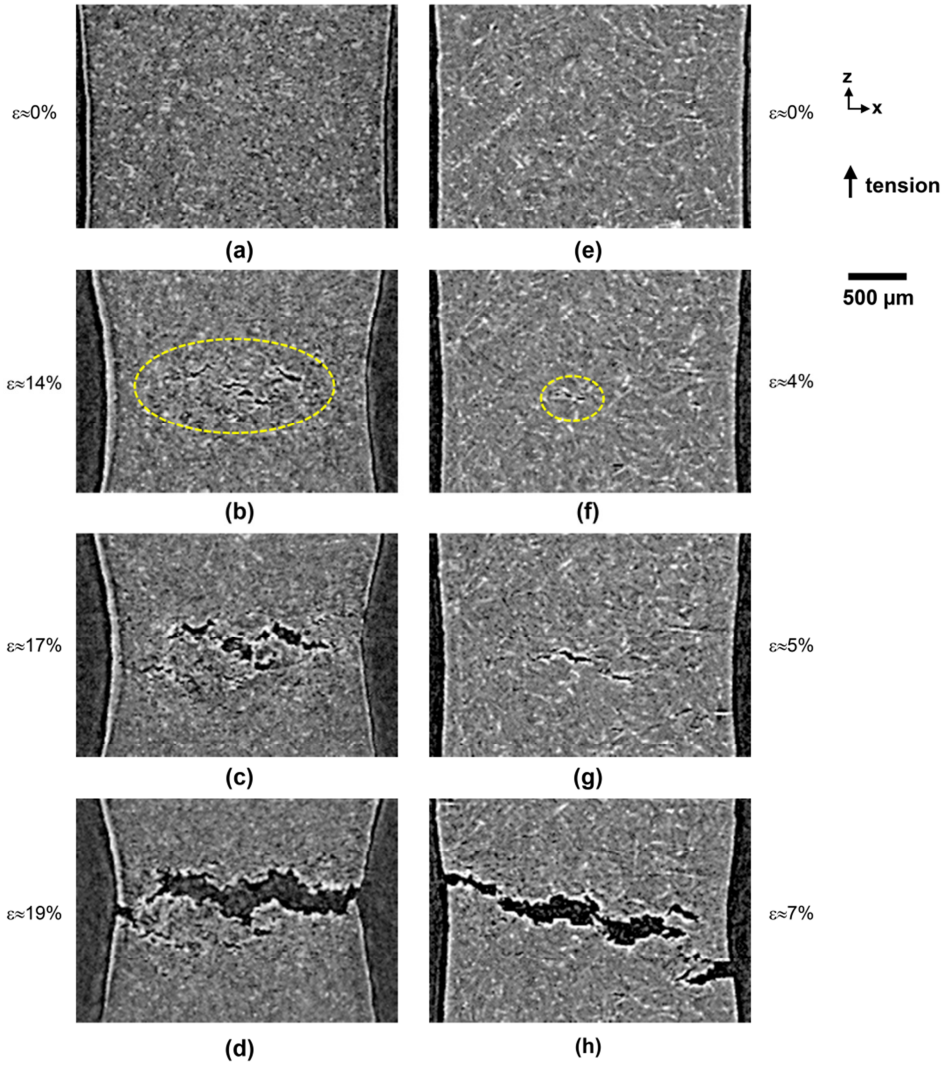


Figure 5.5 Typical evolution of damage during simulated hot tearing in Al-7.5Si-3.5Cu with 0.2 wt.%Fe (a-d) and 0.6 wt.%Fe (e-h). Note that a-d represent true strains (%) of 0, 14, 17, 19 and e-h represent true strains (%) of 0, 4, 5, 7, respectively. Dashed-circles indicate locations where critical damage initiated.

By segmenting the pores, voids and developing damage, the *in situ* damage evolution during hot tearing can be rendered as shown in Figure 5.6a,b. The true strains in all 3-D renderings are identical to those shown in the longitudinal sections in Figure 5.5, and the internal and surface-connected damage is shown in blue and red

respectively. The corresponding development of total volume of damage is quantified and plotted in Figure 5.6c.

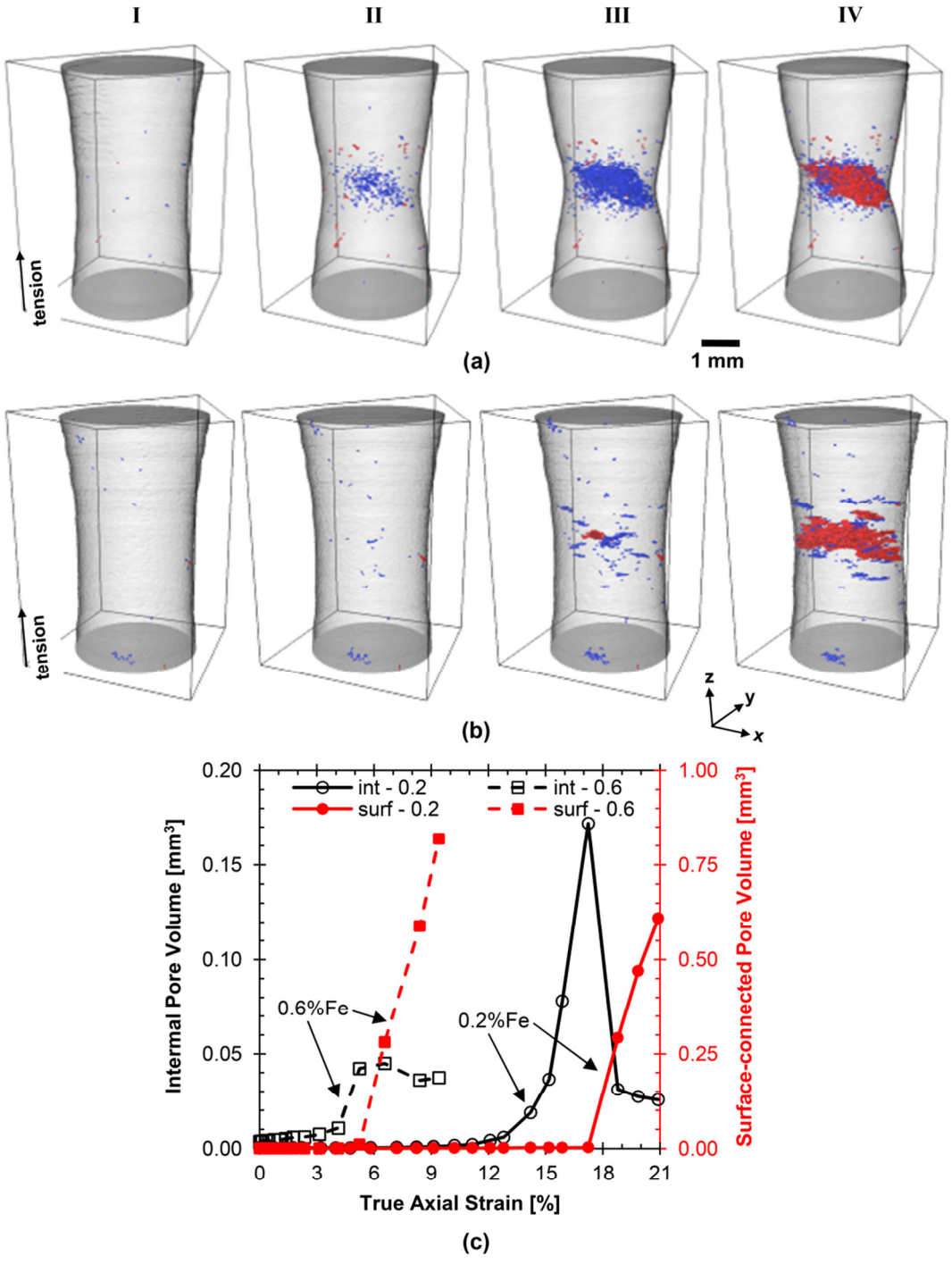


Figure 5.6 3-D rendering of hot tear formation in Al-7.5Si-3.5Cu with (a) 0.2 wt.%Fe and (b) 0.6 wt.%Fe as well as the quantified evolution in (c) the internal damage volume (int) and surface-connected damage volume (surf). I-IV represent true strains (%) of 0, 14, 17, 19 and 0, 4, 5, 7, for specimens with 0.2 wt.%Fe and 0.6 wt.%Fe, respectively. Note that internal damage is coloured in blue and surface-connected damage is labelled in red in (a-b).

Before deformation is applied, it is observed that only small as-cast pores are present in the semi-solid microstructure of both specimens (Figure 5.6a,b-I). Beginning with the specimen at 0.2wt.%Fe (which at a high resolution of 0.9 μm does not appear to contain β-intermetallics as shown in Figure 5.1), it can be seen that new voids nucleate in the middle of the specimen gauge only after a large amount of true strain (~14%) has been applied (Figure 5.6a-II), with a steady increase in the internal damage (Figure 5.6c). Note that the real-time nucleation of these new voids may occur earlier than their actual appearance in the tomographic datasets because of the spatial resolution limits (12.22μm). There is also considerable deformation and necking in the gauge region. Further straining to a true strain of 17% leads to additional void nucleation, existing damage growth and the commencement of damage coalescence (Figure 5.6a-III). This is characterised by a sharp increase in the internal damage of the specimen (Figure 5.6c). Final failure occurs when the majority of internal damage joins up and connects to the specimen surface (Figure 5.6a-IV) at a true strain of 19%. This is characterised by a sharp drop in the internal damage volume mirrored by an increase in the total volume of surface-connected damage shown in Figure 5.6c, which corresponds to the moment when the interconnected network of internal damage reaches the specimen surface.

In comparison, the specimen at 0.6wt.%Fe (with large plate-like β-intermetallics as shown in Figure 5.1) displays a much more brittle-like failure mechanism. In this specimen, voids also form initially near the middle of specimen gauge (Figure 5.6b-II) where triaxiality is the greatest [195], but at a much lower true strain of ~4%, as compared to the 0.2wt.%Fe specimen (Figure 5.6a-II) (ε~14%). Rapid void growth and coalescence are then observed between true strains of 4% and 5% (qualitatively in Figure 5.6b-III and quantitatively in Figure 5.6c) but there is only a limited amount of necking in the gauge region. Final failure occurs at a true strain of approximately 7%

when most of the damage coalesces across the gauge and reaches the specimen surface (Figure 5.6b-IV). This moment is quantified in Figure 5.6c, where a sharp increase in the total volume of surface-connected damage is observed.

It is known that semi-solid tensile deformation promotes the flow of liquid metal to strain-localised regions, leading to regional liquid accumulation to accommodate the applied strains [92, 151, 157]. If liquid feeding is insufficient, strain cannot be accommodated and hot tears may form. In the specimen at 0.2wt%Fe with small, unresolved intermetallics, liquid flow occurs with ease and can thus accommodate a large amount of strain (ε~14%). With increasing strain, the liquid supply becomes insufficient and voids first form internally over a large portion of the core where strain and triaxiality are the greatest [190, 195, 196]. They then grow outwards toward the surface (Figure 5.6a), which occurs through a combination of void nucleation, growth and coalescence. Similar phenomena were previously observed in binary Al-Cu [92, 190] and other commercial alloys [91]. In contrast, because large β-intermetallic particles can severely reduce the permeability of the mush by blocking the interdendritic flow paths [8, 120], liquid feeding of the strained regions in the specimen at 0.6wt.%Fe is much more difficult. Since β-intermetallics also act as stress concentrators, bigger intermetallics weaken the mush [159] and therefore largely contribute to hot tearing failure at very low true strains (Figure 5.6b).

5.3.2 Post-failure observation

Longitudinal sections of the post-failure high-resolution (0.9 μm) tomographic images are given in Figure 5.7, and show the fracture surfaces for both the 0.2wt.%Fe and the 0.6wt.%Fe tensile specimens as seen in Figures 5.7a and 5.7c respectively. The damage voids appear dark, the aluminium grains appear grey and the β-intermetallics appear white. The magnified microstructure in Figure 5.7b reveals a large amount of

internal voids near the fracture surface of the specimen with 0.2wt.%Fe. Most of these internal voids appear round or elongated perpendicular to the loading direction. In contrast, the post-failure microstructure of the 0.6wt.%Fe specimen (Figure 5.7d) exhibits significantly fewer internal voids near the fracture surface. The few number of voids that exist appear almost planar, and many of them are in contact with β-intermetallics.

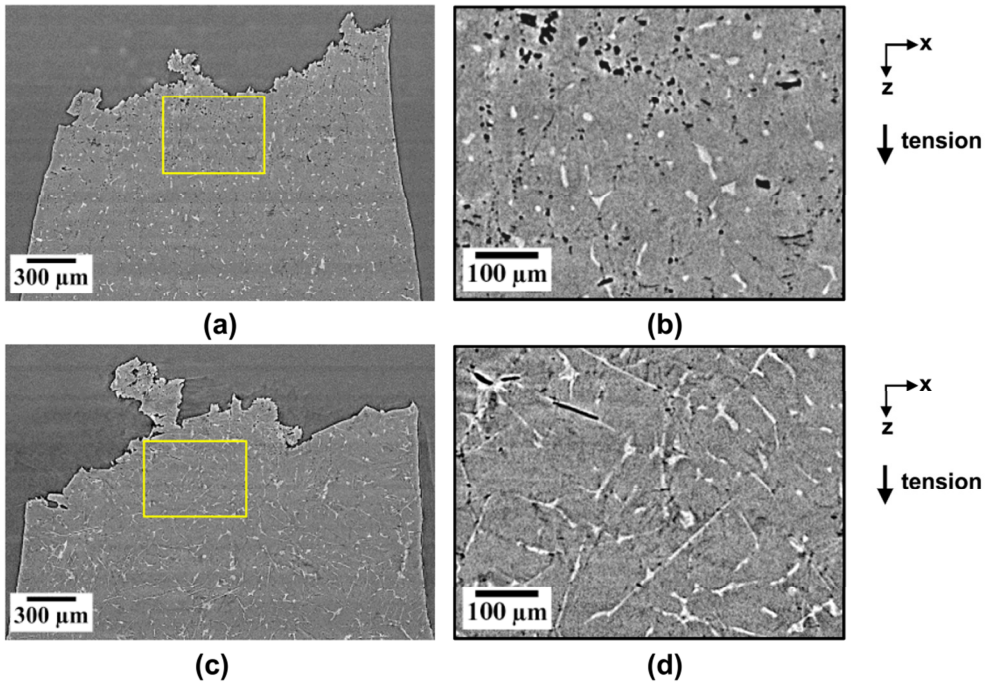


Figure 5.7 (a,c) Longitudinal sections of post-failure microstructures in Al-7.5Si-3.5Cu with 0.2 and 0.6 wt.%Fe, respectively; and (b,d) magnified microstructures from an ROI (yellow square) in (a,c), respectively.

3-D renderings of the internal voids in the post-failure microstructures are shown in Figure 5.8a-b. Qualitatively, the diameter of the neck at failure is smaller in the 0.2wt.%Fe specimen when compared to the 0.6wt.%Fe specimen, as shown in Figure 5.8a compared to 5.8b. This is indicative of the yielding and greater ductile deformation and failure of the 0.2wt.%Fe specimen in contrast to the 0.6wt.%Fe specimen, as described in the previous section. In addition many more internal voids appear in the 0.2wt.% specimen when compared to the 0.6wt.%Fe specimen. By quantifying the number density of the post-failure internal voids as a function of void

volume, Figure 5.8c shows that while there is no significant difference in volume distribution between the two specimens, the 0.2wt.%Fe specimen with unresolved *β*-intermetallics exhibits a much larger number density of voids during straining.

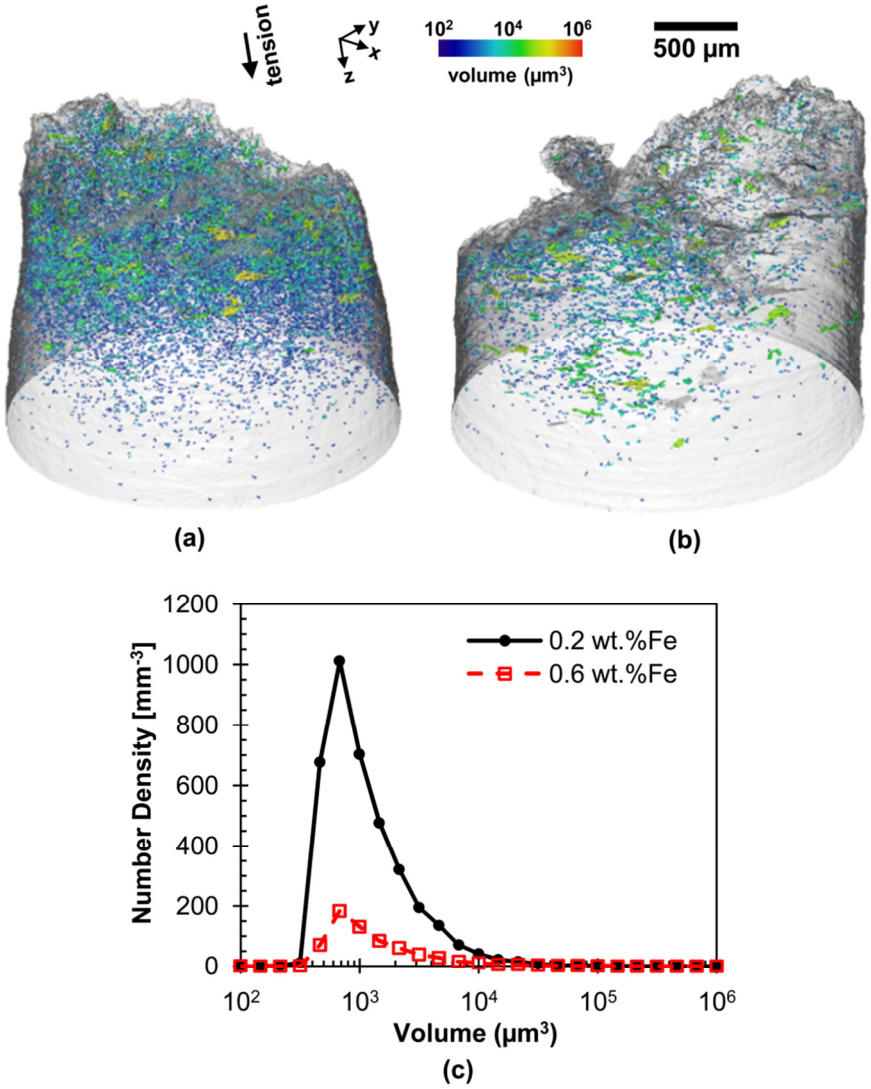


Figure 5.8 (a-b) Rendered internal voids (colour by volume) in Al-7.5Si-3.5Cu with 0.2 and 0.6 wt.%Fe, respectively, and (c) quantified number density and volume of internal voids shown in (a-b).

By using two voids chosen at random near the fracture surfaces, the difference in internal void morphology in the two specimens after hot tearing failure is illustrated in Figure 5.9. In the 0.2wt.%Fe specimen, the void is clearly tortuous, branching and twisting along the complex interdendritic spaces (Figure 5.9a). The void is coloured by local mean curvature to aid in the visualisation of its convexity and concavity. In

contrast, the presence of large β-intermetallics (rendered in grey) in the 0.6wt.%Fe specimen introduces an additional physical constraint and alters void morphology, where it is flatter with less branches, and is preferentially aligned along the planar surface of the β-intermetallic (Figure 5.9b).

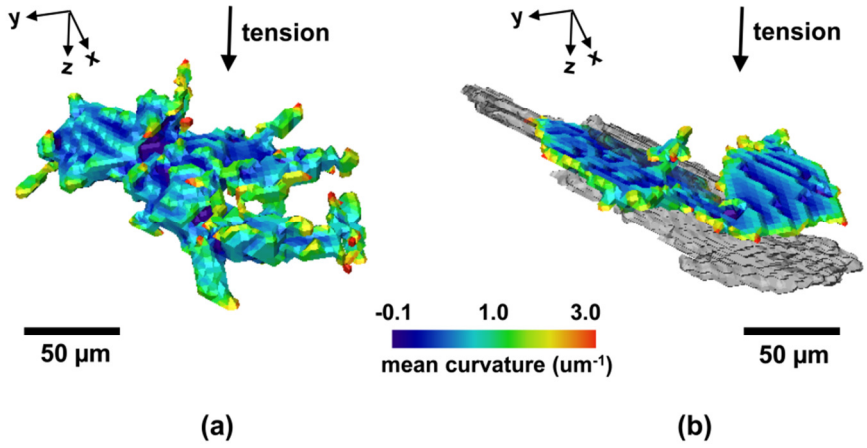


Figure 5.9 (a-b) 3-D rendering of internal void (coloured by local mean curvature) near fracture surface of Al-7.5Si-3.5Cu with 0.2 and 0.6 wt.%Fe, respectively. Intermetallics in (b) are shown in dark colour.

5.4 Discussion

The *in situ* observations of solidification and semi-solid deformation provide new insight into the role of β-intermetallics in assisting in the formation of casting defects. By comparing Figure 5.9b with Figure 5.4, it can be seen that the flat void morphology along the surface of β-intermetallics resulting from hot tearing is similar to the *in situ* observation of pore growth during solidification, where pores were seen to grow preferentially along β-intermetallics. Roy *et al.* [132] previously found that pores were always in contact with β-intermetallics in 2-D quenched Al-Si-Cu microstructures and implied that β-intermetallics are active nucleation sites for pores. These observations are not supported by the current work. First, there was no evidence of pore nucleation on β-intermetallics in the tomographic images of *in situ* solidification. Second, if β-intermetallics were a potent pore nucleation site, there would have been an observable

increase in pore density in the 0.6wt.%Fe specimen during semi-solid deformation as compared to the 0.2wt.%Fe specimen. Thus, both during solidification and isothermal semi-solid deformation, β-intermetallics do not appear as sites for pore nucleation, but instead act as growth sites, potentially due to lower gas-intermetallic interfacial energy [11] or strain localisation [197]. The resulting quasi-planar pore morphology may additionally impose strain localisers at the tip of the pores combined with the stress concentration promoted by the β-intermetallics themselves. Phillion *et al.* [91] previously found that as-cast pores and newly formed voids acted as precursors to hot tearing. The influence of β-intermetallics on facilitating pore/void growth as well as altering pore/void morphology may also promote the initiation of hot tears.

Correlating the orientation of internal voids to loading direction is also of great interest. The orientation of each internal void in the post-failure microstructures was determined using PCA and compared to the tensile direction in order to quantify final void direction under uniaxial tension. A pole figure was obtained for each void, as shown in Figure 5.10, schematic I-IV. In this figure, a pole at the center corresponds to void having a major axis (orientation) parallel to the tensile direction (Figure 5.10-I), whereas a pole on the circumference corresponds to a void with a major axis perpendicular to the tensile direction (Figure 5.10-IV). By integrating all pole figures, an orientation contour plot is obtained (Figures 5.10a and 5.10b), where higher concentrations are shown in red and each calculated pole figure is shown as white dot. In both specimens, the highest concentrations are found lying near the circumference of the image, indicating that internal voids in both specimens are preferentially orientated perpendicular to the loading direction. This is consistent with both Phillion *et al.* [91], who have shown through post-mortem tomographic imaging that crack propagation in semi-solids occurs in the direction perpendicular to the loading direction to utilise the maximum strain energy for new crack surface creation, and also

Sistaninia *et al.* [158, 198, 199] who performed combined discrete/finite element simulations to demonstrate that strain development at high fraction solid is concentrated only along few preferential liquid paths perpendicular to the loading direction.

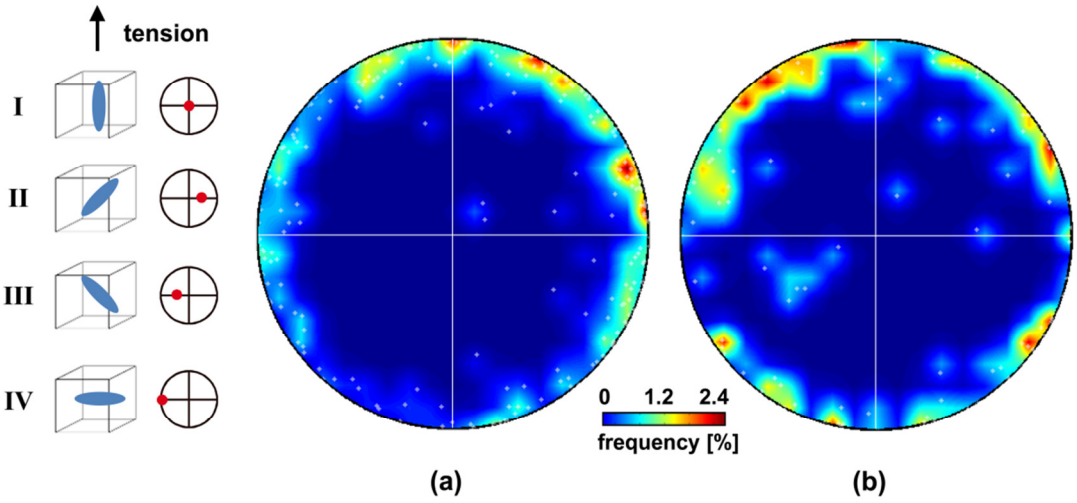


Figure 5.10 Orientation contour plot of all internal void in post-failure microstructures of Al-7.5Si-3.5Cu with (a) 0.2 wt.%Fe and (b) 0.6 wt.%Fe. Inset I-IV schematise orientation plot (each dot in circle) of an object with four different orientations.

Finally, these *in situ* observations may help explain the industrially-observed reduction in hot tearing that occurs through TiB_2 grain refinement and Sr modifications in Al-Si-Cu alloys [7, 160]. These additions have been found to result in finer and shorter β-intermetallics [47, 70], and thus it can be hypothesised that this will greatly reduce the impact of β-intermetallics on flow blockage and stress concentration, leading to a reduction in hot tearing tendency. It is worth noting that the smaller grain size resulting from the addition of TiB_2 also contributes to reducing hot tearing by postponing the coherency solid fraction [149] and converting porosity into smaller pores but with a higher number density [23].

5.5 Summary

The influence of Fe-rich β-intermetallics on solidification defect formation has been quantitatively investigated using 3-D synchrotron x-ray tomography. Two experiments were conducted in this chapter: an *in situ* solidification study of porosity formation and an *in situ* isothermal semi-solid deformation experiment simulating hot tearing. The experiments were performed on a commercial A319 alloy (Al-7.5Si-3.5Cu, wt.%) with two different Fe-levels of 0.2 and 0.6wt.%, providing complex commercial-like casting microstructures with β-intermetallic particles equivalent to primary and recycled aluminium alloy products.

From the *in situ* solidification experiment, the results indicate that the presence of a large fraction of β-intermetallics heavily blocks the interdendritic channels and induces porosity formation as a result of permeability reduction (as shown in Chapter 4) and hydrogen supersaturation in the local subdivided domain. No β-intermetallics were seen directly nucleating a pore during solidification, instead they appear to physically block and constrain pore growth and contribute to the increase in pore tortuosity. In addition, β-intermetallics were found to facilitate pore growth, which may be due to a low interfacial energy between the gas and the intermetallic plates.

From the *in situ* semi-solid deformation experiment, it was found that the β-intermetallics will increase hot tearing susceptibility. The 0.6wt.%Fe specimen only sustained a relatively small amount of deformation (~4%) prior to failure as compared to the 0.2wt.%Fe specimen, and the failure event was much more brittle-like. High-resolution imaging of the β-intermetallic-rich post-failure microstructure also show that the internal voids near the fracture surface of the 0.6wt.%Fe specimen were flatter, less branched, and preferentially aligned to existing β-intermetallics, which may concentrate strain and locally reduce the strength of the semi-solid.

Chapter 6

Conclusions and future work

6.1 Conclusions

In this thesis, a fast *in situ* synchrotron x-ray tomography approach was carried out to dynamically quantify microstructural evolution during the solidification and isothermal uniaxial tensile deformation of a commercial A319 alloy (Al–7.5Si–3.5Cu, wt.%) with two different Fe-levels (0.2-0.6wt.%Fe). The application of novel image analysis techniques as well as image-based computational fluid dynamics (CFD) on solidifying microstructures extracted directly from tomographic experiments allowed the characterisation of:

(1) mechanisms controlling β-intermetallic nucleation and growth,

(2) influence of β-intermetallics on flow blockage and permeability, and

(3) effect of β-intermetallics on porosity and hot tear formation.

These insights into β-intermetallic formation and their interaction with solidification defects are critical to the development of new alloys and provide improved understanding and quantifiable inputs to inform and validate more accurate predictive models of microstructural defect formation.

Nucleation and growth mechanisms of β-intermetallic

Real-time observations during *in situ* solidification reveal the complexity of β-intermetallic formation. Quantitative investigation on these *in situ* results highlights the following new insights:

- The nucleation of the β-intermetallics occurs over a range of temperatures and their nucleation density as a function of nucleation undercooling can be estimated by a Gaussian distribution. The maximum activated nucleation density (n_{max}) was approximately 32 mm^{-3}, while mean (ΔT_M) and deviation (ΔT_σ) of the Gaussian nucleation undercooling distribution was found to be 6°C and 0.9°C, respectively.

- β-intermetallic nucleation mechanisms can be classified into four categories: (1) at the oxidised specimen surface, (2) near the primary aluminium dendrites or in the bulk liquid, (3) on existing β-intermetallics, and (4) on as-cast pores. The most prevalent occurrence for nucleation is on or near aluminium dendrites.

- β-intermetallics preferentially nucleate and grow with an orientation parallel to the secondary dendrite arms of the α-Al dendrites.

- Formation of β-intermetallics is largely complete before the formation of the Al-Si eutectic, suggesting the superiority of the eutectic reaction L → α-Al + β-Al_5FeSi over phase formation.

- β-intermetallics demonstrate fast lateral growth (~30 μm/s) and slow thickening (~2μm/min), agreeing well with prior *in situ* studies. A β-intermetallic first forms with a thin plate-like morphology but subsequently grows rapidly into interdendritic spaces and impinges on dendrites. These physical restrictions cause the β-intermetallic to grow around and in between primary dendrites and/or other solid phases, resulting in very complex plate-like shapes with branches and holes.

- The growth kinetics of each β-intermetallic are strongly driven by undercooling and time after their nucleation event. A higher undercooling leads to a

higher initial growth velocity (Equation (3.2)), and mean lateral growth velocity decreases exponentially with time (Equation (3.3)).

- Both direct impingement and potential branching events of two (or more) β-intermetallics are observed throughout the specimen. This clarifies one of the main debating topics about impingement. Since both impingement and branching events exhibit a wide range of contact angles, it is likely that growth interactions might not be crystallographically related.

- It is proposed that β-intermetallic growth is governed by lateral growth mechanisms and is dominated by impingement events.

Influence of β-intermetallic on fluid flow

A method for coupling *in situ* imaging with numerical CFD modelling was developed to simulate the interdendritic flow without and with the presence of β-intermetallics at solid fractions between 0.10 and 0.85. The following conclusions were made:

- This coupled method enables, for the first time, permeability and fluid flow measurements of an individual microstructure morphology that is changing both in solid fraction and in intermetallic phase evolution. Simulated permeabilities match reasonably well with prior experimental data from the literature for both parallel and normal flow regimes.

- β-intermetallic plates in the solidifying microstructures strongly block interdendritic fluid flow and significantly reduce the permeability of the semi-solid metal.

- β-intermetallics that grow normal to the flow direction were found to have a greater impact on the flow field in comparison to β-intermetallics parallel to the flow direction.

- An analytical expression based on the anisotropic Blake-Kozeny model was developed with a particle blockage term $(1-\beta f_I)$ that takes into account the effects of intermetallic particles on permeability. Permeabilities for flow in parallel (K_p) and normal (K_n) directions are expressed as:

$$K_p = (1-\beta f_I)(8.5\times10^{-4})\frac{f_L^3\lambda_1^2}{1-f_L} \qquad \beta = 15$$

$$K_n = (1-\beta f_I)(4\times10^{-3})\left(\frac{\lambda_1}{\lambda_2}\right)\frac{f_L^3\lambda_1^2}{(1-f_L)^{0.3}} \qquad \beta = 10$$

- In the regime of primary-phase solidification (without Al-Si eutectic), a good fit between the analytical expression and the simulation results was found.

Effect of β-intermetallics on solidification defects

Real-time observations during *in situ* solidification and semi-solid deformation reveal that β-intermetallics contribute in multiple ways to porosity formation and hot tear susceptibility. The following points were concluded:

- While β-intermetallics were not observed to nucleate porosity, they block interdendritic channels, increasing pore tortuosity. The presence of β-intermetallics appears to induce porosity formation as a result of permeability reduction, as discussed above.

- Pores were found to grow preferentially along the surfaces of β-intermetallics, suggesting that β-intermetallics may facilitate pore growth via a reduced interfacial energy between the gas and the β-intermetallic plates.

- The presence of β-intermetallics was found to increase hot tear susceptibility. Since large β-intermetallics can physically block the interdendritic flow path and reduce permeability of the mush as well as act as stress concentrators, they detrimentally

weaken the mush and lead to a much more brittle-like hot tearing failure compared to the more ductile behaviour of the base alloy with small, unresolved β-intermetallics.

- High resolution tomographic imaging on the post-failure microstructure reveals that internal voids near the fracture surface are flatter and less branched in the 0.6wt.%Fe (with large plate-like β-intermetallics) specimen, compared to that in the 0.2wt.%Fe (with small, unresolved β-intermetallics) specimen. Moreover, internal voids are preferentially aligned to the β-intermetallics, similar to the *in situ* observations during solidification. The resulting quasi-planar void morphology may additionally impose strain localisers at the tips of quasi-planar voids and further weaken the mush.

6.2 Suggestions for further research

As seen in Chapter 3, although direct impingement events were observed and confirmed, it is still unclear whether branching events take place. It is possible that impingement may have actually occurred instead of branching. In order to clarify this incidence of very rapid growth interaction, a faster temporal resolution tomographic imaging is suggested for further studies.

The use of fast *in situ* synchrotron x-ray tomography and novel image analysis techniques in this study proves to be a good approach to characterise mechanisms controlling β-intermetallics formation. However, only limited solidification conditions were studied. Further *in situ* synchrotron x-ray tomographic experiments are recommended to enable systematic investigation of the impact of additional parameters on β-intermetallics, including alloying element, cooling rate and grain refiner.

To accurately predict the effect of β-intermetallic formation on real casting components, a multiscale modelling of β-intermetallic formation and microstructural defect formation needs to be developed. Quantifiable inputs obtained in this study, such as nucleation mechanisms and growth dynamics of β-intermetallics as well as mechanisms controlling the interactions between β-intermetallics and evolving defects should be integrated into this multiscale model. Coupled with through process models, these will assist in optimising predictions of processing-microstructure-property relationships in complex near-net-shape cast components.

Bibliography

[1] Lee, P. D., Lindley, T. C., Cheong, C. W. J., Davis, G. R. and Elliott, J. The effect of metallurgical variables and porosity on the high cycle fatigue behaviour of aluminium alloy A319. In: Proceedings of COM. Vancouver, B.C., 2003. p.457-472.

[2] Koch, M. and Hamisch, J. CO_2 emission related to the electricity consumption in the european primary aluminium production - a comparison of electricity supply approaches. Int J LCA 2002;7:283-289.

[3] Vlack, L. H. V. Elements of materials science and engineering. London: Prentice Hall, 1989.

[4] Belov, N. A., Aksenov, A. A. and Eskin, D. G. Iron in aluminium alloys: impurity and alloying element (advances in metallic alloys). London: CRC Press, 2002.

[5] Mondolfo, L. F. Aluminum alloys: structure and properties. London: Butterworths, 1976.

[6] Yi, J. Z., Gao, Y. X., Lee, P. D. and Lindley, T. C. Effect of Fe-content on fatigue crack initiation and propagation in a cast aluminum-silicon alloy (A356-T6). Mat Sci Eng A 2004;386:396-407.

[7] Paray, F., Kulunk, B. and Gruzleski, J. E. Hot tearing in 319 Alloy. Int J Cast Met Res 2000;13:147-159.

[8] Dinnis, C. M., Taylor, J. A. and Dahle, A. K. Iron-related porosity in Al-Si-(Cu) foundry alloys. Mat Sci Eng A 2006;425:286-296.

[9] Mbuya, T. O., Odera, B. O. and Ng'ang'a, S. P. Influence of iron on castability and properties of aluminium silicon alloys: literature review. Int J Cast Met Res 2003;16:451-465.

[10] Taylor, J. A. Metal related castability effects in aluminium foundry alloys. Cast Metals 1995;8:225-252.

[11] Wang, J., Li, M., Allison, J. and Lee, P. D. Multiscale modeling of the influence of Fe content in a Al-Si-Cu alloy on the size distribution of intermetallic phases and micropores. J Appl Phys 2010;107:061804.

[12] Fleming, M. Solidification processing. New York: McGraw-Hill, 1974.

[13] Gibbs, J. W. The collected works of J. Willard Gibbs. New York: Longmans, Green and Co., 1928.

[14] Dantzig, J. A. and Rappaz, M. Solidification. Lausanne: EPFL Press, 2009.

[15] Porter, D. A. and Easterling, K. E. Phase transformations in metal and alloys. London: Chapman & Hall, 1992.

[16] Turnbull, D. Kinetics of heterogeneous nucleation. J Chem Phys 1950;18:198-203.

[17] Kim, W. T. and Cantor, B. An absorption model of the heterogeneous nucleation of solidification. Acta Metall Mater 1994;42:3115-3127.

[18] Cantor, B. Heterogeneous nucleation and adsorption. Philos T Roy Soc A 2003;361:409-417.

[19] Greer, A. L., Cooper, P. S., Meredith, M. W., Schneider, W., Schumacher, P., Spittle, J. A. and Tronche, A. Grain refinement of aluminium alloys by inoculation. Adv Eng Mater 2003;5:81-91.

[20] Quested, T. E. and Greer, A. L. Athermal heterogeneous nucleation of solidification. Acta Mater 2005;53:2683-2692.

[21] Kurz, W. and Fisher, D. J. Fundamentals of solidification. Uetikon-Zuerich: Trans Tech Publications Ltd, 2005.

[22] Turnbull, D. and Fisher, J. C. Rate of nucleation in condensed systems. J Chem Phys 1949;17:71-73.

[23] Lee, P. D. and Hunt, J. D. Hydrogen porosity in directional solidified aluminium-copper alloys: *in situ* observation. Acta Mater 1997;45:4155-4169.

[24] Oldfield, W. A quantitative approach to casting solidification: freezing of cast iron. Trans Am Soc Met 1966;59:945-961.

[25] Gandin, C. A. and Rappaz, M. A coupled finite element - cellular automaton model for the prediction of dendritic grain structures in solidification processes. Acta Metall Mater 1994;42:2233-2246.

[26] Lee, P. D., Wang, J. and Li, M. Coupling *in situ* observations and microscale modeling to predict pore and Fe-rich intermetallic formation during the solidification of Al-Si-Cu-Fe alloys. In: S. L. Cockcroft and D. M. Maijer, editors. 12th Conference on modeling of casting, welding and advanced solidification processes (MCWASP). Vancouver to Alaska:TMS, 2009. p.87 - 99.

[27] Aziz, M. J. Model for solute redistribution during rapid solidification. J Appl Phys 1982;53:1158-1168.

[28] Scheil, E. Bemerkungen zur schichtkristallbildung. Z Metallkd 1942;34:70-72.

[29] Gulliver, G. H. The quantitative effect of rapid cooling upon the constitution of binary alloys. J Inst Met 1913;9:120-157.

[30] McCartney, D. and Hunt, J. A numerical finite difference model of steady state cellular and dendritic growth. Metall Mater Trans A 1984;15:983-994.

[31] Tiller, W. A., Jackson, K. A., Rutter, J. W. and Chalmers, B. The redistribution of solute atoms during the solidification of metals. Acta Metall 1953;1:428-437.

[32] Thomson, W. On the equilibrium of vapour at a curved surface of liquid. Philos Mag 1871;42:448-452.

[33] Van der Veen, J. F. and Reichert, H. Structural ordering at the solid–liquid interface. MRS Bulletin 2004;29:958-962.

[34] Jackson, K. A., Uhlmann, D. R. and Hunt, J. D. On the nature of crystal growth from the melt. J Cryst Growth 1967;1:1-36.

[35] Eidhed, W. Modification of β-Al_5FeSi compound in recycled Al-Si-Fe cast alloy by using Sr, Mg and Cr additions. J Mater Sci Technol 2008;24:45-47.

[36] Wang, J., Lee, P. D., Hamilton, R. W., Li, M. and Allison, J. The kinetics of Fe-rich intermetallic formation in aluminium alloys: *in situ* observation. Scripta Mater 2009;60:516-519.

[37] Zhang, L., Gao, J., Damoah, L. N. W. and Robertson, D. G. Removal of iron from aluminum: a review. Miner Process Extract Metall Rev 2011;33:99-157.

[38] Li, Z., Samuel, A. M., Samuel, F. H., Ravindran, C., Valtierra, S. and Doty, H. W. Parameters controlling the performance of AA319-type alloys: part I - tensile properties. Mat Sci Eng A 2004;367:96-110.

[39] Espinoza-Cuadra, J., García-García, G. and Mancha-Molinar, H. Influence of defects on strength of industrial aluminum alloy Al–Si 319. Mater Design 2007;28:1038-1044.

[40] Seri, O. and Furumata, K. Effect of Al-Fe-Si intermetallic compound phases on initiation and propagation of pitting attacks for aluminum 1100. Mater Corros 2002;53:111-120.

[41] Liang, D., Korgul, P. and Jones, H. Composition and solidification microstructure selection in the interdendritic matrix between primary Al_3Fe dendrites in hypereutectic Al-Fe alloys. Acta Mater 1996;44:2999-3004.

[42] Young, R. M. and Clyne, T. An Al-Fe intermetallic phase formed during controlled solidification. Scripta Metall 1981;15:1211-1216.

[43] Khalifa, W., Samuel, F. and Gruzleski, J. Iron intermetallic phases in the Al corner of the Al-Si-Fe system. Metall Mater Trans A 2003;34:807-825.

[44] Allen, C. M., O'Reilly, K. A. Q., Cantor, B. and Evans, P. V. Intermetallic phase selection in 1XXX Al alloys. Prog Mater Sci 1998;43:89-170.

[45] Crepeau, P. Effect of iron in Al-Si casting alloys: a critical review. AFS Trans 1995;103:361-366.

[46] Kral, M. V. A crystallographic identification of intermetallic phases in Al-Si alloys. Mater Lett 2005;59:2271-2276.

[47] Lu, L. and Dahle, A. Iron-rich intermetallic phases and their role in casting defect formation in hypoeutectic Al-Si alloys. Metall Mater Trans A 2005;36:819-835.

[48] Han, Y., Choi, J., Choi, C. and McCartney, D. Intermetallic phase formation in directionally solidified Al–Si–Fe alloy. Met Mater Int 2004;10:27-32.

[49] Dinnis, C. M., Taylor, J. A. and Dahle, A. K. As-cast morphology of iron-intermetallics in Al-Si foundry alloys. Scripta Mater 2005;53:955-958.

[50] Murali, S., Row, T. N. G., Sastry, D. H., Raman, K. S. and Murthy, K. S. S. Crystal structure of β-$FeSiAl_5$ and (Be-Fe)-$BeSiFe_2Al_8$ phases. Scripta Metall Mater 1994;31:267-271.

[51] Romming, C., Hansen, V. and Gjonnes, J. Crystal structure of β-$Al_{4.5}FeSi$. Acta Crystallogr B 1994:307-312.

[52] Zheng, J. G., Vincent, R. and Steeds, J. W. Crystal structure of an orthorhombic phase in *β*-(Al-Fe-Si) precipitates determined by convergent-beam electron diffraction. Philos Mag A 2000;80:493-500.

[53] Hansen, V., Hauback, B., Sundberg, M., Romming, C. and Gjonnes, J. *β*-$Al_{4.5}FeSi$: a combined synchrotron powder diffraction, electron diffraction, high-resolution electron microscopy and single-crystal x-ray diffraction study of a faulted structure. Acta Crystallogr B 1998;54:351-357.

[54] Salvo, L., Lhuissier, P., Scheel, M., Terzi, S., Di Michiel, M., Boller, E., Taylor, J. A., Dahle, A. K. and Suéry, M. 3D *in situ* imaging of aluminium alloys during solidification. T Indian I Metals 2012;65:623-626.

[55] Allen, C. M., O'Reilly, K. A. Q. and Cantor, B. Effect of semisolid microstructure on solidified phase content in 1xxx Al alloys. Acta Mater 2001;49:1549-1563.

[56] Sha, G., O'Reilly, K. A. Q., Cantor, B., Titchmarsh, J. M. and Hamerton, R. G. Quasi-peritectic solidification reactions in 6xxx series wrought Al alloys. Acta Mater 2003;51:1883-1897.

[57] Backerud, L., Krol, E. and Tamminen, J. Solidification characteristics of aluminum alloys, vol 1: wrought alloys. Oslo: Skanaluminium, 1986.

[58] Sperry, P. R. Correlation of microstructure in 6xxx extrusion alloys with process variable and properties. In: Proceedings of 3rd International aluminum extrusion technology seminar. Atlanta, GA, 1984. p.21-29.

[59] Mulazimoglu, M. H., Zaluska, A., Gruzleski, J. E. and Paray, F. Electron microscope study of Al-Fe-Si intermetallics in 6201 aluminum alloy. Metall Mater Trans A 1996;27:929-936.

[60] Sha, G., O'Reilly, K. and Cantor, B. Characterization of Fe-rich intermetallic phases in a 6xxx series Al alloy. Mater Sci Forum 2006;519-521:1721-1726.

[61] Ashtari, P., Tezuka, H. and Sato, T. Modification of Fe-containing intermetallic compounds by K addition to Fe-rich AA319 aluminum alloys. Scripta Mater 2005;53:937-942.

[62] Du, Y., Schuster, J. C., Liu, Z.-K., Hu, R., Nash, P., Sun, W., Zhang, W., Wang, J., Zhang, L., Tang, C., Zhu, Z., Liu, S., Ouyang, Y., Zhang, W. and Krendelsberger, N. A thermodynamic description of the Al-Fe-Si system over the whole composition and temperature ranges via a hybrid approach of CALPHAD and key experiments. Intermetallics 2008;16:554-570.

[63] Terzi, S., Taylor, J. A., Cho, Y. H., Salvo, L., Suéry, M., Boller, E. and Dahle, A. K. *In situ* study of nucleation and growth of the irregular α-Al/*β*-Al_5FeSi eutectic by 3-D synchrotron x-ray microtomography. Acta Mater 2010;58:5370-5380.

[64] Sigworth, G. and Campbell, J. The modification of Al-Si casting alloys: important practical and theoretical aspects. Int J Metalcast 2009;3:65-74.

[65] Shabestari, S. G., Mahmudi, M., Emamy, M. and Campbell, J. Effect of Mn and Sr on intermetallics in Fe-rich eutectic Al-Si alloy. Int J Cast Met Res 2002;15:17-24.

[66] Campbell, J. Castings. Oxford: Butterworth-Heinemann Ltd, 2003.

[67] Cao, X. and Campbell, J. The nucleation of Fe-Rich phases on oxide films in Al-11.5Si-0.4Mg cast alloys. Metall Mater Trans A 2003;34:1409-1420.

[68] Miller, D. N., Lu, L. and Dahle, A. K. The role of oxides in the formation of primary iron intermetallics in an Al-11.6Si-0.37Mg alloy. Metall Mater Trans B 2006;37:873-878.

[69] Narayanan, L., Samuel, F. and Gruzleski, J. Crystallization behavior of iron-containing intermetallic compounds in 319 aluminum alloy. Metall Mater Trans A 1994;25:1761-1773.

[70] Khalifa, W., Samuel, F., Gm Nserc, U., Gruzleski, J., Doty, H. and Valtierra, S. Nucleation of Fe-intermetallic phases in the Al-Si-Fe alloys. Metall Mater Trans A 2005;36:1017-1032.

[71] McKay, B. J., Cizek, P., Schumacher, P. and O'Reilly, K. A. Q. Heterogeneous nucleation in an Al–Ni–Si alloy studied using a metallic glass technique. Mat Sci Eng A 2001;304–306:240-244.

[72] Allen, C. M., O'Reilly, K. A. Q., Evans, P. V. and Cantor, B. The effect of vanadium and grain refiner additions on the nucleation of secondary phases in 1xxx Al alloys. Acta Mater 1999;47:4387-4403.

[73] Kim, B., Lee, S., Lee, S. and Yasuda, H. Real-time radiographic observation of solidification behavior of Al-Si-Cu casting alloys with the variation of iron content. Mater Trans 2012;53:374-379.

[74] Sha, G., O'Reilly, K., Cantor, B., Worth, J. and Hamerton, R. Growth related metastable phase selection in a 6xxx series wrought Al alloy. Mat Sci Eng A 2001;304-306:612-616.

[75] Laird, C. and Aaronson, H. I. The growth of γ plates in an Al-15%Ag alloy. Acta Metall 1969;17:505-519.

[76] Couture, A. Iron in aluminum casting alloys - a literature survey. AFS Int Cast Metals J 1981;6:9-17.

[77] Liu, L., Mohamed, A. M. A., Samuel, A. M., Samuel, F. H., Doty, H. W. and Valtierra, S. Precipitation of β-Al_5FeSi phase platelets in Al-Si based casting alloys. Metall Mater Trans A 2009;40:2457-2469.

[78] Samuel, A. M., Pennors, A., Villeneuve, C., Samuel, F. H., Doty, H. W. and Valtierra, S. Effect of cooling rate and Sr-modification on porosity and Fe-intermetallics formation in Al-6.5%Si-3.5%Cu-Fe alloys. Int J Cast Met Res 2000;13:231-253.

[79] Shabestari, S. G. The effect of iron and manganese on the formation of intermetallic compounds in aluminum-silicon alloys. Mat Sci Eng A 2004;383:289-298.

[80] Gustafsson, G., Thorvaldsson, T. and Dunlop, G. The influence of Fe and Cr on the microstructure of cast Al-Si-Mg alloys. Metall Mater Trans A 1986;17:45-52.

[81] Mahta, M., Emamy, M., Daman, A., Keyvani, A. and Campbell, J. Precipitation of Fe rich intermetallics in Cr- and Co-modified A413 alloy. Int J Cast Met Res 2005;18:73-79.

[82] Samuel, A. M., Samuel, F. H., Villeneuve, C., Doty, H. W. and Valtierra, S. Effect of trace elements on ß-Al_5FeSi characteristics, porosity and tensile properties of Al-Si-Cu (319) cast alloys. Int J Cast Met Res 2001;14:97-120.

[83] Samuel, A. M. and Samuel, F. H. Effect of alloying elements and dendrite arm spacing on the microstructure and hardness of an Al-Si-Cu-Mg-Fe-Mn (380) aluminium die-casting alloy. J Mater Sci 1995;30:1698-1708.

[84] Samuel, F., Samuel, A., Ouellet, P. and Doty, H. Effect of Mg and Sr additions on the formation of intermetallics in Al-6 wt pct Si-3.5 wt pct Cu-(0.45) to (0.8) wt pct Fe 319-type alloys. Metall Mater Trans A 1998;29:2871-2884.

[85] Samuel, A. M., Samuel, F. H. and Doty, H. W. Observations on the formation of β-Al_5FeSi phase in 319 type Al-Si alloys. J Mater Sci 1996;31:5529-5539.

[86] Narayanan, L. A. and Samuel, F. H. Thermal analysis studies on the effect of cooling rate on the microstructure of the 319 aluminium alloy. AFS Trans 1992;100:383-391.

[87] Srivastava, A. K., Srivastava, V. C., Gloter, A. and Ojha, S. N. Microstructural features induced by spray processing and hot extrusion of an Al–18% Si–5% Fe–1.5% Cu alloy. Acta Mater 2006;54:1741-1748.

[88] Li, J., Zarif, M. and Schumacher, P. TEM investigation of a novel Fe containing phase in high purity Al-Si-Fe alloys. BHM Berg- Huttenmann Monatsh 2010;155:499-505.

[89] Lee, P. D., Chirazi, A. and See, D. Modeling microporosity in aluminum-silicon alloys: a review. J Light Met 2001;1:15-30.

[90] Beckermann, C. Macrosegregation. In: K. H. J. Buschow, R. W. Cahn, M. C. Flemings, B. Ilschner, E. J. Kramer, S. Mahajan and P. Veyssière, editors. Encyclopedia of materials: science and technology. NY:Elsevier Science, 2001. p.4733-4739.

[91] Phillion, A. B., Lee, P. D., Maire, E. and Cockcroft, S. L. Quantitative assessment of deformation-induced damage in a semisolid aluminum alloy via x-ray microtomography Metall Mater Trans A 2008;39:2459-2469.

[92] Phillion, A. B., Hamilton, R. W., Fuloria, D., Leung, A. C. L., Rockett, P., Connolley, T. and Lee, P. D. *In situ* x-ray observation of semi-solid deformation and failure in Al-Cu alloys. Acta Mater 2011;59:1436-1444.

[93] Flemings, M. C. Solidication processing. NY: McGraw-Hill, 1974.

[94] Poirier, D. R. Permeability for flow of interdendritic liquid in columnar-dendritic alloys. Metall Trans B 1987;18:245-255.

[95] Lee, P. D., Chirazi, A., Atwood, R. C. and Wang, W. Multiscale modelling of solidification microstructures, including microsegregation and microporosity, in an Al-Si-Cu alloy. Mat Sci Eng A 2004;365:57-65.

[96] Gladman, T. On the theory of the effect of precipitate particles on grain growth in metals. P Roy Soc Lond A Mat 1966;294:298-309.

[97] Piwonka, T. S. and Flemings, M. C. Pore formation in solidification. T Metall Soc AIME 1966;236:1157-1165.

[98] Apelian, D., Flemings, M. C. and Mehrabian, R. Specific permeability of partially solidified dendritic networks of Al-Si alloys. Metall Trans 1974;5:2533-2537.

[99] Nasser-Rafi, R., Deshmukh, R. and Poirier, D. R. Flow of interdendritic liquid and permeability in Pb-20 wt pct Sn alloys. Metall Trans A 1985;16:2263-2271.

[100] Murakami, K., Shiraishi, A. and Okamoto, T. Interdendritic fluid flow normal to primary dendrite-arms in cubic alloys. Acta Metall 1983;31:1417-1424.

[101] Murakami, K., Shiraishi, A. and Okamoto, T. Fluid flow in interdendritic space in cubic alloys. Acta Metall 1984;32:1423-1428.

[102] Duncan, A. J., Han, Q. and Viswanathan, S. Measurement of liquid permeability in the mushy zones of aluminum-copper alloys. Metall Mater Trans B 1999;30:745-750.

[103] Han, Q., Viswanathan, S. and Duncan, A. J. Permeability measurements of the flow of interdendritic liquid in equiaxed aluminum-silicon alloys. Metall Mater Trans B 2003;34:25-28.

[104] Nielsen, Ø., Arnberg, S., Mo, A. and Thevik, H. Experimental determination of mushy zone permeability in aluminum-copper alloys with equiaxed microstructures. Metall Mater Trans A 1999;30:2455-2462.

[105] Nielsen, Ø. and Arnberg, L. Experimental difficulties associated with permeability measurements in aluminum alloys. Metall Mater Trans A 2000;31:3149-3153.

[106] Bernard, D., Nielsen, Ø., Salvo, L. and Cloetens, P. Permeability assessment by 3D interdendritic flow simulations on microtomography mappings of Al–Cu alloys. Mat Sci Eng A 2005;392:112-120.

[107] Khajeh, E. and Maijer, D. M. Numerical determination of permeability of Al-Cu alloys using 3D geometry from x-ray microtomography. Mater Sci Technol 2010;26:1469-1476.

[108] Khajeh, E. and Maijer, D. M. Permeability of dual structured hypoeutectic aluminum alloys. Acta Mater 2011;59:4511-4524.

[109] Fuloria, D., Lee, P. D. and Bernard, D. Microtomographic characterization of columnar Al-Cu dendrites for fluid flow and flow stress determination. Mat Sci Eng A 2008;494:3-9.

[110] Khajeh, E. and Maijer, D. M. Permeability evolution during equiaxed dendritic solidification of Al–4.5 wt%Cu. Model Simul Mater Sc 2012;20:035004.

[111] Darcy, H. Les Fontaines Publiques de la Ville de Dijon. Paris: Victor Delmont, 1856.

[112] Carman, P. Flow of gases through porous media. London: Butterworths Scientic Publications, 1956.

[113] Khajeh, E. and Maijer, D. M. Physical and numerical characterization of the near-eutectic permeability of aluminum–copper alloys. Acta Mater 2010;58:6334-6344.

[114] Sun, Z., Logé, R. E. and Bernacki, M. 3D finite element model of semi-solid permeability in an equiaxed granular structure. Comp Mater Sci 2010;49:158-170.

[115] Schneider, M. C., Gu, J. P., Beckermann, C., Boettinger, W. J. and Kattner, U. R. Modeling of micro- and macrosegregation and freckle formation in single-crystal nickel-base superalloy directional solidification. Metall Mater Trans A 1997;28:1517-1531.

[116] Heinrich, J. C. and Poirier, D. R. Convection modeling in directional solidification. Comptes Rendus Mécanique 2004;332:429-445.

[117] Santos, R. G. and Melo, M. L. N. M. Permeability of interdendritic channels. Mat Sci Eng A 2005;391:151-158.

[118] Al-Jarba, K. A. and Fuchs, G. E. Carbon-containing single-crystal nickel-based superalloys: segregation behavior and carbide formation. JOM 2004;56:50-55.

[119] Ness, D., Thuniet, L., Bernard, D. and Lee, P. D. Simulation of the influence of carbides on the permeability of Ni-base superalloys. In: Proceedings of TMS annual meeting & exhibition Orlando, FL, 2007.

[120] Dash, M. and Makhlouf, M. Effect of key alloying elements on the feeding characteristics of aluminum-silicon casting alloys. J Light Met 2001;1:251-265.

[121] Couper, M. J., Neeson, A. E. and Griffiths, J. R. Casting defects and the fatigue behavior of an aluminium casting alloy. Fatigue Fract Eng M 1990;13:213-227.

[122] Major, J. F. Porosity control and fatigue behavior in A356-T61 aluminium alloy. AFS Trans 1990;105:901-906.

[123] Wang, Q. G., Apelian, D. and Lados, D. A. Fatigue behavior of A356-T6 aluminum cast alloys: part I - effect of casting defects. J Light Met 2001;1:73-84.

[124] Ransley, C. E. and Neufeld, H. The solubility of hydrogen in liquid and solid aluminium. J Inst Met 1948;74:599-620.

[125] Fredriksson, H. and Svensson, I. On the mechanism of pore formation in metals. Metall Mater Trans B 1976;7:599-606.

[126] Whittenberger, E. J. and Rhines, F. N. Origin of porosity in castings of magnesium-aluminium and other alloys. J Met 1952:409–420.

[127] Jones, S. F., Evans, G. M. and Galvin, K. P. Bubble nucleation from gas cavities - a review. Adv Colloid Interfac 1999;80:27-50.

[128] Fox, S. and Campbell, J. Visualisation of oxide film defects during solidification of aluminium alloys. Scripta Mater 2000;43:881-886.

[129] Lee, P. D. and Hunt, J. D. Measuring the nucleation of hydrogen porosity during the solidification of aluminium-copper alloys. Scripta Mater 1997;36:399-404.

[130] Atwood, R. C., Sridhar, S. and Lee, P. D. Equations for nucleation of hydrogen gas pores during solidification of aluminium seven weight percent silicon alloy. Scripta Mater 1999;41:1255-1259.

[131] Taylor, J., Schaffer, G. and StJohn, D. The role of iron in the formation of porosity in Al-Si-Cu-based casting alloys: part I - initial experimental observations. Metall Mater Trans A 1999;30:1643-1650.

[132] Roy, N., Samuel, A. and Samuel, F. Porosity formation in AI-9 wt pct Si-3 wt pct Cu alloy systems: metallographic observations. Metall Mater Trans A 1996;27:415-429.

[133] Dinnis, C., Taylor, J. and Dahle, A. Interactions between iron, manganese, and the Al-Si eutectic in hypoeutectic Al-Si alloys. Metall Mater Trans A 2006;37:3283-3291.

[134] Rooy, E. L. Aluminium scrap recycling and its impact on the metals casting industry. AFS Trans 1985;93:935-938.

[135] Iwahori, H., Takamiya, H., Yonekura, K., Yamamoto, Y. and Nakamura, M. Influence of iron and manganese on feedability of AC2B aluminum alloy. Journal of the Japan foundrymen's society 1988;60:590-595.

[136] Otte, M., McDonald, S., Taylor, J., StJohn, D. and Schneider, W. Controlling porosity-related casting rejects: understanding the role of iron in Al-Si alloys. AFS Trans 1999;107:471-478.

[137] Taylor, J., Schaffer, G. and StJohn, D. The role of iron in the formation of porosity in Al-Si-Cu-based casting alloys: part II - a phase-diagram approach. Metall Mater Trans A 1999;30:1651-1655.

[138] Wang, J. S. and Lee, P. D. Simulating tortuous 3D morphology of microporosity formed during solidification of Al-Si-Cu alloys. Int J Cast Met Res 2007;20:151-158.

[139] Guven, Y. F. and Hunt, J. D. Hot tearing in aluminium copper alloys. Cast Metals 1988;1:104-111.

[140] Farup, I., Drezet, J. M. and Rappaz, M. *In situ* observation of hot tearing formation in succinonitrile-acetone. Acta Mater 2001;49:1261-1269.

[141] Suyitno, Kool, W. H. and Katgerman, L. Integrated approach for prediction of hot tearing. Metall Mater Trans A 2009;40:2388-2400.

[142] Eskin, D. G., Suyitno and Katgerman, L. Mechanical properties in the semi-solid state and hot tearing of aluminium alloys. Prog Mater Sci 2004;49:629-711.

[143] Vero, J. Hot tearing of aluminum alloys. Metal Industry 1936;48:431-491.

[144] Pellini, W. S. Strain thoery of hot tearing. Foundry 1952;80:125-199.

[145] Rappaz, M., Drezet, J. M. and Gremaud, M. A new hot-tearing criterion. Metall Mater Trans A 1999;30A:449-455.

[146] Sistaninia, M., Phillion, A. B., Drezet, J. M. and Rappaz, M. A 3-D coupled hydromechanical granular model for simulating the constitutive behavior of metallic alloys during solidification. Acta Mater 2012;60:6793-6803.

[147] Rosenburg, R. A., Flemings, M. C. and Taylor, H. F. Nonferrous binary alloys hot tearing. AFS Trans 1960;69:518-528.

[148] Dahle, A. K. and StJohn, D. H. Rheological behaviour of the mushy zone and its effect on the formation of casting defects during solidification. Acta Mater 1998;47:31-41.

[149] Veldman, N. M., Dahle, A., StJohn, D. and Arnberg, L. Dendrite coherency of Al-Si-Cu alloys. Metall Mater Trans A 2001;32:147-155.

[150] Gourlay, C. M. and Dahle, A. K. Dilatant shear bands in solidifying metals. Nature 2007;445:70-73.

[151] Suéry, M., Terzi, S., Mireux, B., Salvo, L., Adrien, J. and Maire, E. Fast *in situ* x-ray microtomography observations of solidification and semisolid deformation of Al-Cu alloys. JOM 2012;64:83-88.

[152] Kareh, K. M., Lee, P. D. and Gourlay, C. M. Globule-globule interactions during deformation in semi-solid Al-Cu using time-resolved x-ray tomography. Solid State Phenom 2013;192-193:179-184.

[153] Fonseca, J., O'Sullivan, C., Nagira, T., Yasuda, H. and Gourlay, C. M. *In situ* study of granular micromechanics in semi-solid carbon steels. Acta Mater 2013;61:4169-4179.

[154] Gourlay, C. M., Dahle, A. K., Nagira, T., Nakatsuka, N., Nogita, K., Uesugi, K. and Yasuda, H. Granular deformation mechanisms in semi-solid alloys. Acta Mater 2011;59:4933-4943.

[155] Davidson, C., Viano, D., Lu, L. and StJohn, D. Observation of crack initiation during hot tearing. Int J Cast Met Res 2006;19:59-65.

[156] Mitchell, J. B., Cockcroft, S. L., Viano, D., Davidson, C. and StJohn, D. Determination of strain during hot tearing by image correlation. Metall Mater Trans A 2007;38:2503-2512.

[157] Terzi, S., Salvo, L., Suéry, M., Limodin, N., Adrien, J., Maire, E., Pannier, Y., Bornert, M., Bernard, D., Felberbaum, M., Rappaz, M. and Boller, E. *In situ* x-ray tomography observation of inhomogeneous deformation in semi-solid aluminium alloys. Scripta Mater 2009;61:449-452.

[158] Sistaninia, M., Terzi, S., Phillion, A. B., Drezet, J. M. and Rappaz, M. 3-D granular modeling and *in situ* x-ray tomographic imaging: a comparative study of hot tearing formation and semi-solid deformation in Al–Cu alloys. Acta Mater 2013;61:3831-3841.

[159] Sweet, L., Easton, M., Taylor, J., Grandfield, J., Davidson, C., Lu, L., Couper, M. and StJohn, D. Hot tear susceptibility of Al-Mg-Si-Fe alloys with varying iron contents. Metall Mater Trans A 2012:1-12.

[160] D'Elia, F. and Ravindran, C. Influence of grain refinement on hot tearing in B206 and A319 aluminum alloys. T Indian I Metals 2009;62:315-319.

[161] Yi, J., Gao, Y., Lee, P., Flower, H. and Lindley, T. Scatter in fatigue life due to effects of porosity in cast A356-T6 aluminum-silicon alloys. Metall Mater Trans A 2003;34:1879-1890.

[162] Fife, J. L., Rappaz, M., Pistone, M., Celcer, T., Mikuljan, G. and Stampanoni, M. Development of a laser-based heating system for *in situ* synchrotron-based x-ray tomographic microscopy. J Synchrot Radiat 2012;19:352-358.

[163] Mokso, R., Marone, F. and Stampanoni, M. Real time tomography at the Swiss Light Source. AIP Conf Proc 2010;1234:87-90.

[164] Kak, A. C. and Slaney, M. Principles of computerized tomographic imaging. PA: Society of Industrial and Applied Mathematics, 2001.

[165] Marone, F., Munch, B. and Stampanoni, M. Fast reconstruction algorithm dealing with tomography artifacts. In: Proceedings of Developments in x-ray tomography VII. 2010. p.780410.

[166] Marone, F. and Stampanoni, M. Regridding reconstruction algorithm for real-time tomographic imaging. J Synchrot Radiat 2012;19:1029-1037.

[167] Münch, B., Trtik, P., Marone, F. and Stampanoni, M. Stripe and ring artifact removal with combined wavelet-Fourier filtering. Opt Express 2009;17:8567-8591.

[168] Studholme, C. An overlap invariant entropy measure of 3D medical image alignment. Pattern Recogn 1999;32:71-86.

[169] Pluim, J. P. W., Maintz, J. B. A. and Viergever, M. A. Mutual-information-based registration of medical images: a survey. IEEE Trans Med Imag 2003;22:986-1004.

[170] Gonzalez, R. C., Woods, R. E. and Eddins, S. L. Digital image processing using Matlab. USA: Gatesmark Publishing, 2009.

[171] Weickert, J., Haar, B. and Viergever, R. Efficient and reliable schemes for nonlinear diffusion filtering. IEEE T Image Process 1998;7:398-410.

[172] Adams, R. and Bischof, L. Seeded region growing. IEEE T Pattern Anal 1994;16:641-647.

[173] Puncreobutr, C., Lee, P., Hamilton, R. and Phillion, A. Quantitative 3D characterization of solidification structure and defect evolution in Al alloys. JOM 2012;64:89-95.

[174] Crocker, J. C. and Grier, D. G. Methods of digital video microscopy for colloidal studies. J Colloid Interface Sci 1996;179:298-310.

[175] Yue, S., Lee, P. D., Poologasundarampillai, G. and Jones, J. R. Evaluation of 3-D bioactive glass scaffolds dissolution in a perfusion flow system with x-ray microtomography. Acta Biomater 2011;7:2637-2643

[176] Lorensen, W. E. and Cline, H. E. Marching cubes: A high resolution 3D surface construction algorithm. In: Proceedings of Computer graphics and interactive techniques. New York, NY, 1987. p.163-169.

[177] Nystroem, I., Udupa, J. K., Grevera, G. J. and Hirsch, B. E. Area of and volume enclosed by digital and triangulated surfaces. In: Proceedings of Medical imaging: visualization, image-guided procedures, and display. San Diego, CA, 2002. p.669-680.

[178] Sato, M., Bitter, I., Bender, M. A., Kaufman, A. E. and Nakajima, M. TEASAR: tree-structure extraction algorithm for accurate and robust skeletons. In: Proceedings of 8th Pacific conference on computer graphics and applications. 2000. p.281-449.

[179] Deza, M. M. and Deza, E. Encyclopedia of distances. NY: Springer, 2013.

[180] Fife, J. L. and Voorhees, P. W. The morphological evolution of equiaxed dendritic microstructures during coarsening. Acta Mater 2009;57:2418-2428.

[181] Backerud, L., Chai, G. and Tamminen, J. Solidification characteristics of aluminum alloys, vol 2: foundry alloys. Sweden: AFS and Skanaluminium, 1990.

[182] Lee, P. D. and Hunt, J. D. Hydrogen porosity in directionally solidified aluminium-copper alloys: a mathematical model. Acta Mater 2001;49:1383-1398.

[183] Narayanan, L. A., Samuel, F. H. and Gruzleski, J. E. Dissolution of iron intermetallics in Al-Si alloys through nonequilibrium heat treatment. Metall Mater Trans A 1995;26:2161-2174.

[184] Cho, Y. H., Lee, H. C., Oh, K. H. and Dahle, A. K. Effect of strontium and phosphorus on eutectic Al-Si nucleation and formation of β-Al_5FeSi in hypoeutectic Al-Si foundry alloys. Metall Mater Trans A 2008;39:2435-2448.

[185] Liu, Z.-K. and Chang, Y. Thermodynamic assessment of the Al-Fe-Si system. Metall Mater Trans A 1999;30:1081-1095.

[186] Zhang, S., Klimentidis, R. E. and Barthelemy, P. Micron to millimeter upscaling of shale rock properties based on 3D imaging and modeling. In: Proceedings of Society of core analysts (SCA) symposium. Aberdeen, UK, 2012.

[187] Mirbagheri, S. M. H. and Chirazi, A. Simulation of interdendritic liquid permeability for low and high solid fractions during the solidification of mushy alloys. Mat Sci Eng A 2006;427:51-59.

[188] Mathiesen, R., Arnberg, L., Li, Y., Meier, V., Schaffer, P., Snigireva, I., Snigirev, A. and Dahle, A. X-ray videomicroscopy studies of eutectic Al-Si solidification in Al-Si-Cu. Metall Mater Trans A 2011;42:170-180.

[189] Lee, P. D., Wang, J. and Atwood, R. C. Microporosity formation during the solidification of aluminum-copper alloys. JOM-e 2006;Online only.

[190] Puncreobutr, C., Lee, P., Hamilton, R., Cai, B. and Connolley, T. Synchrotron tomographic characterization of damage evolution during aluminum alloy solidification. Metall Mater Trans A 2013;44:5389-5395.

[191] Titarenko, S., Titarenko, V., Kyrieleis, A., Withers, P. J. and De Carlo, F. Suppression of ring artefacts when tomographing anisotropically attenuating samples. J Synchrot Radiat 2011;18:427-435.

[192] Titarenko, V., Bradley, R., Martin, C., Withers, P. J. and Titarenko, S. Regularization methods for inverse problems in x-ray tomography. In: Proceedings of Developments in x-ray tomography VII. 2010. p.78040Z.

[193] Kyrieleis, A., Titarenko, V., Ibison, M., Connolley, T. and Withers, P. J. Region-of-interest tomography using filtered backprojection: assessing the practical limits. J Microsc 2011;241:69-82.

[194] Felberbaum, M. and Rappaz, M. Curvature of micropores in Al–Cu alloys: an x-ray tomography study. Acta Mater 2011;59:6849-6860.

[195] Kaye, M., Puncreobutr, C., Lee, P. D., Balint, D. S., Connolley, T., Farrugia, D. and Lin, J. A new parameter for modelling 3D damage evolution validated using synchrotron tomography. Acta Mater 2013;61:7616-7623.

[196] Puncreobutr, C., Lee, P. D., Kaye, M., Balint, D., Farrugia, D., Connolley, T. and Lin, J. Quantifying damage accumulation during the hot deformation of free-cutting steels using ultra-fast synchrotron tomography. IOP Conf Ser: Mater Sci Eng 2012;33:012038.

[197] Gao, Y. X., Yi, J. Z., Lee, P. D. and Lindley, T. C. A micro-cell model of the effect of microstructure and defects on fatigue resistance in cast aluminum alloys. Acta Mater 2004;52:5435-5449.

[198] Sistaninia, M., Phillion, A. B., Drezet, J. M. and Rappaz, M. Simulation of semi-solid material mechanical behavior using a combined discrete/finite element method. Metall Mater Trans A 2011;42:239-248.

[199] Sistaninia, M., Phillion, A. B., Drezet, J. M. and Rappaz, M. Three-dimensional granular model of semi-solid metallic alloys undergoing solidification: fluid flow and localization of feeding. Acta Mater 2012;60:3902-3911.